The Transient Foil Bearing Problem in Magnetic Recording

by

Sinan Müftü

Submitted in Partial Fulfillment
of the
Requirements for the Degree

Doctor of Philosophy

Supervised by Professor Richard C. Benson

Department of Mechanical Engineering
College of Engineering and Applied Science

University of Rochester

Rochester, New York

1994

©copyright 1994

"Her ne kadar sürç-ü lîsan ettikse affola."

Curriculum Vitae

The author was born on January 15th, 1964, in St. Louis, Missouri in the United States of America. He completed his elementary school, junior high school, and high school education in Ayşeabla İlkokulu, Tevfik Fikret Lisesi, and Ankara Fen Lisesi, in Ankara, Turkey, respectively. After graduating from high school he spent one year in Glendora, California as an exchange student with AFS student exchange program.

He received a BS degree from the Department of Mechanical Engineering of the Middle East Technical University, in Ankara. After graduating in 1987, he worked as a teaching assistant in the Department of Architecture of the same university while he studied toward a MS, M.E. degree under the supervision of Professor A. Erman Tekkaya in the field of large deformation solid mechanics and finite element method. He was awarded a MS degree in 1989. He started his Ph.D. studies in the Department of Mechanical Engineering of the University of Rochester, in the fall of 1989. There he served as a teaching, and research assistant and recieved a MS degree. He spent the summer of 1992 in 3M, St. Paul, Minnesota where he started the initial stages of his dissertation studies in Dr. David P. Smith's Laboratory. His research topic involved numericaly modeling the magnetic tape behavior in the head-tape interface. His thesis supervisor was Professor Richard C. Benson.

He is a student member of the American Society of Mechanical Engineers and the Society for Industrial and Applied Mathematics.

Acknowledgments

I thank Professor Richard Benson, my thesis advisor, for his help and guidance throughout this study. I thank Professors Al Clark, Larry Taber, Roger Gans, Sheryl Gracewski, Colin McKinstrie, and Riccardo Betti for fruitful discussions. This work was supported by Dean Bruce Arden's office and by the Department of Mechanical Engineering. Their contributions are greatfully acknowledged. The computer time provided by the Laboratory for Laser Energetics of the University of Rochester, and the Cornell National Supercomputer Facility is also greatfully acknowledged. I also acknowledge the support of Dr. David Smith and Mr. David Madsen of the 3M Company by providing me a summer job in their laboratory.

Past and present members of the Mechanics of the Flexible Structures Project and the occupants of Room 410 also contributed to this work in one way or another. I acknowledge their helps. I extend my particular thanks to Mr. Ken Stack and Mr. Ted Diehl for their helpful suggestions. I thank Ms. Lynne Brum for reading parts and Mr. John LaFleche for reading all of the text and making corrections. Thanks to Dr. Pierre Basséras for being such a neat office mate, and for his friendship.

I acknowledge the invaluable contributions of all of my teachers in various stages of my education.

I thank Mr. Bülent "Mucit" Murtezaoğlu for many suggestions on everything and for his friendship. I thank Ms. Lynne Brum for her friendship, support, and patience.

Finally, I thank my mother and my brother for their love, support and help, and remember the loving memory of my father.

The Transient Foil Bearing Problem in Magnetic Recording

by

Sinan Müftü

Abstract

The transient foil bearing problem applied to the magnetic recording applications is modeled and analyzed through numerical simulation. Air lubrication is modeled using the Reynolds equation including the first order slip correction terms and air compressibility. A segmented model for the out-of-plane tape displacements where the tape is modeled as a cylindrical shell in the wrap zone and as a plate in the straight segments between the guide pins and the tangency points is introduced. The tape inertia and transport effects are included by using the material time derivative of the displacements.

A semidiscrete form of the equation of motion of the tape is obtained by using finite difference approximations to partial derivative operators. The time integration of this equation is performed by using the Hilber-Hughes-Taylor method. The Reynolds equation is solved using the alternating direction implicit method.

The effects of axial tension variations, tape width, transient tension and tape speed changes, as well as initial stages of drum rotation in split-drum recording are studied. It is shown that the axial variations on the parameters mentioned can lead to unintended tape-guide separations. For slow drum speeds and small drum radii the inertial effects of the tape are damped out by the air bearing.

Wave propagation due to a point load in circumferentially transported cylindrical shells, in the absence of air lubrication is analyzed. The existence of a critical load speed is demonstrated, and the effect of shell's transport speed, thickness, and tension on this critical load speed are identified.

A frequency analysis for the tape equation is performed. It is shown that this medium is anisotropically dispersive. It is shown that the long wavelength behavior in the tape is due to the shell stiffness and the short wavelength behavior is due to the bending effects. The wave velocity deterioration due to spatial finite difference discretization in the numerical solution is shown quantitatively.

Contents

Curriculum Vitae iv

Acknowledgements v

Abstract vi

Contents vii

List of Figures xi

List of Tables xvi

1 Introduction 1

1.1 A Brief Survey of the Foil Bearing Literature 3

1.1.1 One Dimensional Steady State Analysis 4

1.1.2 Two Dimensional Steady State Analysis 6

1.1.3 Transient Analysis 7

1.1.4 Inverse Analysis 9

2 Governing Equations 11

2.1 Introduction 11

2.2 Equation of Motion of the Tape 12

2.2.1 Boundary Conditions and Initial Conditions of the Shell Equation 19

2.3 Tape Geometry 20

2.4 The Modified Reynolds Equation for Gas Lubrication 23
2.4.1 Derivation of the Modified Reynolds Equation 25
2.4.2 Boundary Conditions 28
2.5 Tape-Guide Spacing, h 28
2.6 Contact Pressure 29

3 Solution Methods **31**
3.1 Introduction 31
3.2 Spatial Discretization of the Equation of Motion of the Tape 32
3.2.1 The Finite Difference Mesh 32
3.2.2 The Finite Difference Equations 33
3.2.3 Constants of the Tape Equation 38
3.3 Semidiscrete Form of the Equation of Motion of the Tape 39
3.4 Numerical Solution of the Semidiscrete Equation of Motion 41
3.4.1 Concepts Related to Discrete Time Integration 41
3.4.2 The α-*method* for Time Integration 42
3.4.3 Implicit Integration Algorithm 43
3.4.4 Explicit Integration Algorithm 44
3.5 Numerical Solution of the Reynolds Equation 46
3.6 Coupled Solution of the Governing Equations 49

4 Frequency Analysis of the Semidiscrete System **52**
4.1 Introduction 52
4.1.1 Background on Dispersion 53
4.1.2 Analyzing the Effects Numerical Solutions 55
4.2 The Dispersion Relation 56
4.3 Dispersion Relation for the Discretized Equation 58
4.4 Comparison of Wave Action on the Continuous and Discretized Tape . . 60
4.5 Summary and Conclusions 61

5 Numerical Solution of the Transient Displacement of a Circumferentially Moving Cylindrical Shell **76**

5.1 Introduction 76

5.2 The Effects of Numerical Damping 77

5.3 Simulation of the Effects of a Stationary Load on a Moving Tape 78

5.3.1 Results and Discussion 83

5.4 Wave Action Due to a Concentrated Load Moving on a Circumferentially Transported Tape 90

5.4.1 Results and Discussion 91

5.5 Conclusions 92

6 Foil Bearing Problem for a Large Angle of Wrap and Infinitely Wide Tape **99**

6.1 Introduction 99

6.2 Governing Equations 100

6.3 Boundary Conditions and Initial Conditions 101

6.4 Solution Method 102

6.4.1 Discretization of the Tape Equation 103

6.4.2 Discretization of the Reynolds Equation 104

6.4.3 The Solution Algorithm 107

6.5 Convergence Studies 107

6.6 Results and Conclusions 109

7 The 2D Foil Bearing Problem **115**

7.1 Introduction 115

7.2 Problem Formulation 117

7.2.1 The Pressure Boundary Layers 119

7.2.2 Interpolation 120

7.3 The Steady State in Linear Recording 123

7.3.1 Tape Width Effects in Linear Recording 125
7.3.2 The Effect of Axial Tension Variation 126
7.3.3 The Effect of Guide Surface Shape 127
7.4 Transient Effects 128
7.4.1 Transient Effects in Linear Recording 129
7.4.2 Transient Effects in a Helical-Scan Application 133
7.5 Summary and Conclusions 134

8 Summary and Conclusions **161**

BIBLIOGRAPHY **165**

List of Figures

1-1 Tape under tension T_x passing over a cylindrical guide, with radius R, with speed V_x. Figure is taken from Barlow [4]. 5

1-2 Tape-guide spacing and air bearing pressure in a foil bearing,$\epsilon = 6\mu V_x/T_x$, $\chi = x\epsilon^{1/3}/h_O$. Figure is taken from Gross [27]. 6

2-1 The head tape configuration. 13

2-2 Cylindrical shell element 15

2-3 Tape geometry for the large angle of wrap analysis. 22

2-4 The coordinate system for the lubrication of a tape. 24

3-1 Discretized tape. 34

4-1 Analytical dispersion curve for $V_x = 25m/s$, at different orientations, $\theta = 0, \pi/4, \pi/2$. 63

4-2 Phase and Group Velocities for $V_x = 25, \theta = \pi/4$. 64

4-3 Phase and group velocities for different tape transport speeds, $V_x = 0, 25, 50, 75m/s$, at $\theta = \pi/4$. 65

4-4 Phase and group velocities for different orientations, $\theta = 0, \pi/4, \pi/2$ at tape speed $V_x = 25m/s$. 66

4-5 The effect of finer Δ on the phase velocity, V_p, predicted by the discretized solution for $V_x = 25m/s, \theta = \pi/4$. 67

4-6 The effect of finer Δ on the group velocity, V_{g_x}, predicted by the discretized solution, for $V_x = 25m/s, \theta = \pi/4$. 68

4-7 The effect of finer Δ on the group velocity, V_{g_y}, predicted by the discretized solution, for $V_x = 25m/s, \theta = \pi = 4$. 69

4-8 The phase velocity error due to discretization, ε_p, variation with Δ, as a function of wavelength , for $V_x = 25m/s, \theta = \pi/4$. 70

4-9 The group velocity error in x-direction due to discretization, ε_{g_x}, variation with Δ, as a function of wavelength, for $V_x = 25m/s, \theta = \pi/4$. 71

4-10 The group velocity error in y-direction due to discretization, ε_{g_y}, variation with Δ, as a function of wavelength, for $V_x = 25m/s, \theta = \pi/4$. 72

4-11 The effect of tape transport speed, V_x on the phase velocity error due to discretization, ε_p. 73

4-12 The effect of tape transport speed, V_x on the group velocity error due to discretization in x-direction, ε_{g_y}, as a function of wavelength. 74

4-13 The velocity error as a function of λ/Δ, for phase and group velocities. . 75

5-1 The case run without numerical damping. 79

5-2 The case that is run with numerical damping in the Newmark family. . . 80

5-3 The case that is run with α-method damping. 81

5-4 Transient displacement of the load point ($x_o = L_x/2, y_o = L_y/2$) for a concentrated step load as a function of tape velocities, $(0, 50, 70, 80, 85m/s)$. 84

5-5 Displacement Wave Propagation of the Tape in Response to a Concentrated Step Load, $V_x = 0m/s$. 88

5-6 Displacement Wave Propagation of the Tape in Response to a Concentrated Step Load, $V_x = 50m/s$. Tape motion is in the + x direction. . . . 89

5-7 Tape configuration in helical-scan recording 90

5-8 Tape deflections at subcritical head velocity, $V_L = 50m/s$. Problem parameters are $c = 10\mu m, T_x = 90N/m, V_x = 2.5m/s$ and $\alpha = -0.05, \beta = 0.275625, \gamma = 0.55$. Tape motion is in the + x direction. 93

5-9 Tape deflections near critical head velocity, $V_L = 80m/s$. Problem parameters are $c = 10\mu m, T_x = 90N/m, V_x = 2.5m/s$ and $\alpha = -0.05, \beta = 0.275625, \gamma = 0.55$. Tape motion is in the $+ x$ direction. 94

5-10 Tape deflections at super-critical head velocity, $V_L = 100m/s$. Problem parameters are $c = 10\mu m, T_x = 90N/m, V_x = 2.5m/s$ and $\alpha = -0.05, \beta = 0.275625, \gamma = 0.55$. Tape motion is in the $+ x$ direction. 95

5-11 The effect of increasing the tape thickness on the critical head velocity, $c = 20\mu m$. Problem parameters are $V_L = 80m/s, T_x = 90N/m, V_x = 2.5m/s$ and $\alpha = -0.05, \beta = 0.275625, \gamma = 0.55$. Tape motion is in the $+ x$ direction. 96

5-12 The effect of tension increase on the critical head velocity, $T_x = 135N/m$. Problem parameters are $c = 10\mu m, V_L = 80m/s, V_x = 2.5m/s$ and $\alpha = -0.05, \beta = 0.275625, \gamma = 0.55$. Tape motion is in the $+ x$ direction. . . . 97

5-13 The effect tape transport speed increase on the critical head velocity, $V_x = 25m/s$. Problem parameters are $c = 10\mu m, V_L = 80m/s, T_x = 90N/m$ and $\alpha = -0.05, \beta = 0.275625, \gamma = 0.55$. Tape motion is in the $+ x$ direction. . 98

6-1 The time stepping algorithm for the foil bearing problem as given by Stahl et al. 106

6-2 Convergence study for $20\mu m$ thick tape, as a function of Δt and Δx. . . 108

6-3 Comparing the flying heights for the experimental case from Vogel and Groom with the two approaches to the foil bearing problem. 109

6-4 Comparison of the air pressure at steady state for the Vogel and Groom's geometry. 110

6-5 Comparison of the steady state foil bearing heights for different tape thicknesses as a function of number of nodes, N_t, used to solve the problem. . 113

6-6 Comparison of the steady state foil bearing heights for different tape thicknesses as a function of spatial step size, Δx. 114

7-1 The guide shape in the y (axial) direction. 119

7-2 Isoparametric, bilinear interpolation element used in interpolating the variables between the pressure and tape domains. 122
7-3 The tape and pressure solution domains, and the tape and pressure interpolation elements. 122
7-4 A schematic view of the tape-guide separation, h. 131
7-5 The initial stages of the transient analysis. 140
7-5 ctd. 141
7-5 ctd. 142
7-6 The tape-guide spacing, h, air pressure, p, and the contact pressure, p_c at steady state. 143
7-7 Steady state tape-guide spacing, h, for different tape widths, L_y. 144
7-8 Cross section of the steady state tape-guide spacing, h, for different tape widths at $x = L_x/2$. 145
7-9 Cross section of the steady state air pressure, p, for different tape widths at $x = L_x/2$. 145
7-10 Cross section of the steady state tape-guide spacing, h, for different tape widths at $x = L_x/2$. 146
7-11 Cross section of the steady state air pressure, p, for different tape widths at $x = L_x/2$. 146
7-12 The effect of axial tension variation on steady state tape-guide spacing, h. 147
7.13 The effect of axial guide shape on the steady state tape guide separation. 148
7-14 Steady state flying heights at cross-sections $(L_x/2, y)$, at 30% above and below the nominal tension, $T_x = 276.7N/m$. 149
7-15 Transient effects while tension is reduced 30%, from $276.7N/m$, in $1ms$. . 150
7-16 Transient effects at $(x, L_y/2)$ and $(x, L_y/2)$, while tension is reduced 30%, from $276.7N/m$, in $1ms$. 151
7-17 Transient effects while tension is increased 30%, from $276.7N/m$, in $1ms$. 152

7-18 Transient effects at $(x, L_y/2)$ and $(x, L_y/2)$, while tension is increased 30%, from $276.7N/m$, in $1ms$. 153

7-19 Transient effects while tape speed is decreased 30%, from $0.5m/s$, in $1ms$. 154

7-20 Transient effects at $(x, L_y/2)$ and $(x, L_y/2)$, while tape speed is decreased 30%, from $0.5m/s$, in $1ms$. 155

7-21 Transient effects while an asperity moves under the tape. The asperity is defined by Equation (7.29) where asperity height, $A = 2\mu m$, and $a = 0.1$. The asperity moves with the same same speed as the tape. See Table 7.4 for the tape parameters. 156

7-21 ctd. 157

7-22 Tape displacement and pressure profiles at the cross section $(x, L_y/2)$ for the moving asperity case. 158

7.23 Transient displacement variation in a helical-scan like simulation. 159

7.24 Transient pressure variation in a helical-scan like simulation 160

List of Tables

2.1 Variables of the equation of motion of the cylindrical shell. 19

2.2 Variables of the Reynolds equation 28

4.1 Typical parameters for a helical-scan application. 62

5.1 Parameters for Figures 5.1-5.3 78

5.2 Variables and typical values for a magnetic recording application 84

6.1 Specifications for example problem for the Stahl et al.case. 111

6.2 Specifications of the test case for Vogel and Groom. 112

7.1 Steady state tape-guide separation values at $(L_x/2, L_y/2)$ when there is a sinusoidal dent or protrusion on the guide surface 128

7.2 Node spacing for the pressure domain for helical-scan simulation 134

7.3 Specifications for test case from Stahl et al. 137

7.4 Specifications for test case from Vogel and Groom. 138

7.5 Specifications for the helical scan case. 139

Chapter 1

Introduction

Successful recording on magnetic media was first achieved by Valdemar Poulsen in 1898 in Denmark. To record his voice on a steel wire, stretched across his laboratory, Poulsen moved an electromagnet, a battery and a telephone transmitter assembly along the wire while he talked into the transmitter. To listen to what he had recorded he replaced the transmitter and the battery with the receiver of a telephone and walked along the same path [14].

In this experiment, by using the telephone transmitter Poulsen was creating a magnetic field whose strength is proportional to the changes in his voice. By walking along the wire he magnetized the wire according to the strength of this magnetic field. Thus he effectively put a magnetic duplicate of his speech along the wire. Almost a hundred years later we can listen to our recordings on magnetic tapes with much less trouble than Poulsen initially had to go through, thanks to the developments made on the magnetic recording technology. However, the principle that Poulsen used remains the same.

Today, magnetic recording is not only used to record analog audio and video signals, but digital data as well. The digital format has a wide spread use in the computer data storage and its use in audio and video storage is increasing. The magnetic recording media has experienced drastic changes as did the recording instruments. Today in addition to tapes, two other widely used recording media are the hard and floppy disks used

in computer data storage. These two technologies provide a faster data access time compared to the tapes in which information is stored in a sequential manner[1].

In the early days of magnetic recording steel wires were used as the recording medium. Later steel tapes and paper tapes coated with magnetic particles were introduced. Plastic based substrates were introduced with success in 1935. Today the magnetic recording tapes consist of polyethylene terephthalate substrates coated with magnetic particles such as gamma-ferrite, γ-Fe_2O_3, chromium-dioxide, CrO_2, held together with an organic binder. Non-magnetic particles such as Al_2O_3 are added to the coating to improve the abrasion resistance [43, Chapter 3].

There are two main types of widely used tape recording technologies. In *linear* recording the magnetic tracks are laid in the direction of motion of the tape by a stationary magnetic head. In *helical-scan* format a slowly moving tape is wrapped around a rotating cylindrical drum in a helical fashion. In contrast to linear recording, the magnetic heads protruding from the drum surface scan the tape with a high relative speed as the drum rotates and write diagonally oriented tracks.

The interface between the magnetic head (the *guide* hereafter) and the flexible tape experiences a self lubrication phenomenon in which air acts as the lubricant[2]. Due to this phenomenon a gap occurs between the tape and the guide. This gap is desirable under certain circumstances because it reduces head and tape wear, but in general it is undesirable as the strength of the magnetic signal degrades with increased tape gap [44, Chapter 4]. This degradation is seen in the head output voltage, e, given by the Wallace equation,

$$\frac{e_h}{e_c} = exp(-\frac{2\pi h}{\lambda}) \tag{1.1}$$

the subscript c denotes a full contact situation and h denotes a tape-guide separation of h. The loss becomes more severe for small wave lengths, λ, of the recorded signal [43, Chapter 1]. Therefore, a thorough understanding of this interface is important for the

[1]The faster access time is due partly to the fast motion of the recording head and partly to the fact that the head has to travel smaller distances on a circular tape.

[2]See Chapter 7 for a more detailed description of this phenomenon.

quality of the magnetic recording. This self lubricated tape-guide interface constitutes the *foil bearing problem* that we study in this thesis.

In the rest of this chapter we present a brief survey of the foil bearing problem literature. In Chapter 2, the equations that we used to model the problem are presented. These equations are the equation of motion of a cylindrical shell modified to accommodate the flat parts of the tape, and the modified Reynolds equation for the air lubrication model. The methods that we used to solve these equations, as well as the method to solve these equations together are presented in Chapter 3. Because we are including the inertial effects of the tape we wanted to quantify the error introduced by the spatial discerization of the tape equation. This study is given in Chapter 4, where we also derive the dispersion relation for the partial differential equation governing the tape displacements. In Chapter 5 we study the wave propagation due to a moving point load in a circumferentially moving tape. As did some of the other investigators [29] [39], we also found that the results of the one dimensional problem constitute a good initial guess for the two dimensional case. Our approach to the solution of the 1D problem is given in Chapter 6. The two dimensional foil bearing problem is studied in Chapter 7. The tape width, axial tape tension variation and guide-shape effects are shown in steady state. Tape response to asperity motion, time dependent tape tension and tape speed variations are studied in the transient domain. In Chapter 8 the summary of the work and the conclusions are given, and suggestions for future work are made.

1.1 A Brief Survey of the Foil Bearing Literature

Several publications address the historical development of foil bearings. A review of the analytical work prior to 1969 is given by Wildmann [71]. Chapter 6 of the book edited by Gross [27] expands this review to 1980, and includes transient 1D problems. A qualitative classification of the iteration techniques used to solve the steady state problem, is given by Ono [53].

1.1.1 One Dimensional Steady State Analysis

The first published work on the foil bearings was by Blok and von Rossum, in 1953. This study involved experimental investigations as well as mathematical modeling. In the early models of the foil bearing problem the foil was assumed to be perfectly flexible, its inertial effects were neglected and the air was assumed to be incompressible. The foil was also assumed to be infinitely wide [71]. This assumption is the basis for the name *one dimensional (1D)* foil bearing problem. These studies identified three distinctive regions in a foil bearing: the *entrance, constant gap* and *exit* regions which are shown in Figures 1-1 - 1-2. In the entrance region the tape-guide spacing, h, decreases exponentially to its value in the constant gap region, h_o. In the exit region we see a sinusoidal variation in h before it increases exponentially. The behavior in the exit region is observed for relatively large wrap angles (see for example [5],) and it can be explained by considering a simplified form of the lubrication equation relating the air pressure to the bearing height[3],

$$\frac{dp}{dx} = 6\mu V_x \frac{h - h_o}{h^3} \tag{1.2}$$

where, μ and V_x are the air viscosity and tape velocity, respectively [27]. Using this equation together with Figure 1-2 the pressure gradient in the tape's running direction, x, is found to be as follows:

$$\frac{dp}{dx} \begin{cases} > 0, & \text{in the entrance region where } h > h_o \\ = 0, & \text{in the constant gap region where } h = h_o \\ > 0, & \text{in the exit region where } h > h_o \end{cases} \tag{1.3}$$

In the entrance of the tape guide interface, $\frac{dp}{dx}$ is positive. Therefore, the air pressure increases from ambient to its value in the constant gap region. In the constant gap region the pressure gradient is zero, consequently the pressure remains constant. In the exit region the pressure drops to the ambient pressure. However, close inspection of Equation (1.3) shows that the pressure gradient is positive in this region. This causes a

[3]The Reynolds equation is introduced in Chapter 2. In Equation (1.2) infinitely wide bearing assumption was used along with incompressibility.

Figure 1-1: Tape under tension T_x passing over a cylindrical guide, with radius R, with speed V_x. Figure is taken from Barlow [4].

confusing situation which is resolved in the system by a sudden increase in the pressure followed by a sudden decrease to the subambient pressure. Once the air bearing pressure becomes subambient the sign of the pressure gradient changes for pressure to increase to ambient. The shape of the pressure distribution on the foil bearing can be seen in Chapters 6 and 7.

These theoretical results were obtained by asymptotic analysis and linearization of the foil bearing equations around a constant foil bearing height, h_o . The three regions of the foil bearing were experimentally observed by Ma, and Licht in 1965 and 1968, respectively [42, 41].

The effects of finite width, fluid inertia, compressibility, foil bending stiffness were addressed, in analytical studies, by Eshel and Elrod, and Licht [18, 41].

Various investigators used numerical techniques to solve the 1D, steady state foil bearing problem in the last two decades; Hori et al. [32], White and Prabhu [69], Brewen et al. [11], Tanaka [62], Adams [1, 2], Lacey and Talke, [38]. In these studies the steady state solution of the problem is obtained by starting the iterative numerical solutions with a good guess. Different relaxation and iteration methods have been employed by these investigators.

Figure 1-2: Tape-guide spacing and air bearing pressure in a foil bearing,$\epsilon = 6\mu V_x/T_x$, $\chi = x\epsilon^{1/3}/h_O$. Figure is taken from Gross [27].

1.1.2 Two Dimensional Steady State Analysis

In the *two dimensional (2D)* foil bearing problem the effects due to the finite tape width are considered. The first 2D formulation of the problem was published by Barlow, in 1967 [4]. Barlow did not publish a solution for his 2D formulation at that time.

To the best of our knowledge, the 2D, steady state foil bearing problem was addressed for the first time by Greenberg in 1979, [25]. In his model Greenberg considered both the in-plane and out-of-plane tape displacements. He presented an analytical method for the tape deformation in terms of infinite series. The coupling of the tape equation with the Reynolds equation, which was solved with a finite difference approach, was achieved in steady state.

Ono, and Mizukawa employed a Green's function to solve the 2D, steady state tape equation in 1981 [54]. In order to decrease computational and storage requirements of this method they used the Green's function corresponding to the origin (which was located at the center of the tape) for the rest of the tape. Through numerical experiments, they found a strong correlation between the bending stiffness of the tape and the minimum spacing in the head tape interface.

In 1985, Mizukawa et al. [48], published their experimental results that they checked

against Ono and Mizukawa [54]. They experimented on a spherical head geometry, and used white light interferometry (WLI) technique for spacing measurements. A good description of the experimental technique is described in the paper. Their experimental results about the effects of bearing penetration on the spacing distribution and the minimum spacing agreed well with numerical predictions of [54] for low bearing penetrations.

In 1988, Yoneda and Sawada used the Kirchhoff plate theory[4] to properly account for the additional stiffening in the radial direction due to in-plane forces [73]. Their equations did not involve the usual stress function formulation of the theory, but in-plane displacements u and v were calculated instead. They applied Galerkin's method to simultaneously solve the Reynolds and the plate equations.

Ono et al. used the inverse analysis concept (which is explained below) to reach the steady state solution of the 2D foil bearing problem in 1991, [53]. In this paper a qualitative evaluation of the steady state iteration techniques used to couple the to media is given.

Mizoh et al. in 1992 [47] and Kotera et al. in 1993 [36] used a similar set of plate equations as Yoneda and Sawada [73] with the addition of bending orthotropy of the tape.

In 1993 Fujimoto et al. used a cylindrical shell formulation embedded into a Kirchhoff plate theory formulation [21]. This way they were able to account for the effects of the in-plane force distribution on the out-of-plane displacements. They used a numerical method in which the finite difference approximations were employed.

1.1.3 Transient Analysis

Transient behavior of the foil bearing problem was addressed for the first time in a paper by Eshel and Wildmann in 1968 [19]. They analyzed a 1D problem and neglected the foil inertia and foil bending, but they considered the squeeze term[5] of the Reynolds equa-

[4] See [64, Chapter 13] for the Kirchhoff plate theory.
[5] See Chapter 2 for the definition of this term.

tion. In this paper they reported that "... disturbances (to the foil bearing) propagate at a speed equal to one half the tape velocity." Eshel in 1969 [17], and Barnum and Elrod in 1971 [6] used similar assumptions and reached analytically the same disturbance propagation velocity.

The first paper which considered the inertial loads of the tape was published by Stahl, White and Deckert (SWD) in 1974 [58]. The tape was modeled by using a moving beam equation with a flat reference configuration. Thus the analysis of non-circular head shapes was made possible with certain restrictions. This study is explained in more detail in Chapter 6. In this study they made use of the transient tape behavior to reach the steady state deflection as suggested by Eshel in 1969 [17].

Vogel and Groom [67] performed experiments in the same year to verify the results that SWD had obtained through their analytical work. Among the conclusions that came out of this paper was the significance of the *side flow* of air on the lateral edges of the tape based on observing lower experimental foil heights compared to SWD's numerical results [58]. The same conclusion was reached by Hori et al. in 1975, [32], and by Tanaka in 1985, [62] who compared experimental foil bearing heights with 1D analysis.

In 1984, Granzow and Lebeck employed the Crank-Nicholson technique in order to improve the solution speed of the SWD approach [24]. They were able to use a time step that was three orders of magnitude bigger than the one used by Stahl et al.

In 1986, Heinrich and Wadhwa analyzed the SWD equations using Finite Element discretization of the tape equation, [30]. They used Newmark's method for the temporal discretization. Their approach eliminated the convergence problems that SWD and Granzow and Lebeck's algorithms had for non-circular head geometries.

In 1990, Rongen published his work on the 2D problem in which he modeled the tape with the large deflection Kirchhoff plate theory given with the stress-function formulation [57]. In this study the inertial effects of the tape are neglected, but the time derivatives[6] are retained in the Reynolds equation. Rongen presented the results of an

[6]This is the squeeze term of the Reynolds equation. See Chapter 2 for its definition.

analysis of the helical-scan problem. The plate equations used by Rongen were similar to the one used by Wolf et al. [72] in 1983. However, Rongen's study included also the bending stiffness of the tape.

Heinrich and Connolly solved the 2D problem using the finite element method in 1991 [29]. They modeled the tape as a plate, and retained the time derivatives in both equations, but they neglected the term that represents the gyroscopic effects[7] of the tape transport. They used the Newmark's method in temporal domain, to reach steady state solutions. They solved the SWD problem in 2D and verified the predictions of Vogel and Groom, on the effects of finite width to foil height.

Fujimoto et al.'s study considered the inertial effects in all three directions, namely x, y and z. However, they calculated an equivalent mass for the effects of the air bearing. Thus, their transient simulations did not involve the coupled solution of the Reynolds equation with the tape equation [21].

1.1.4 Inverse Analysis

Methods aiming to obtain a gap height distribution for a fixed head geometry, face the difficult task of obtaining the simultaneous solution of the two equations that represent the tape and lubrication. By assuming that the gap height is a given design parameter, the inverse method no longer has to find a simultaneously converged solution for the two equations. Therefore, the mathematical problem becomes simplified.

In 1985, White and Prabhu [69], and Brewen et al. [11] published studies on the inverse design concept independently. This involves coupling of the tape and Reynolds equations by; 1) assuming a gap height, 2) obtaining the pressure distribution according to this assumed value, and 3) determining the tape deformation by using the pressure distribution calculated in the previous step. Finally, in the last step the head shape is determined from the tape deformation and the assumed gap height.

A drawback of this method is the limitations on the manufacturability of the head

[7] See Chapters 2 and 5 for the definition of the gyroscopic term.

shape that the method predicts for the given gap height. However, one may impose an iteration scheme, on the inverse analysis method, which would force the head shape to converge to a predetermined value. In 1991, Ono et al. [53] showed that this method of iteration converges faster compared to other iteration methods (relaxation of gap height or air pressure) previously employed (see for example [25].)

Chapter 2

Governing Equations

2.1 Introduction

In this chapter we present the equation of motion of an elastic cylindrical shell, and the Reynolds lubrication equation, along with the necessary boundary and initial conditions for the foil bearing problem. The approaches by Flügge [20], and Timoshenko [63, 64] are the two main resources for the cylindrical shell equations. Derivation of the Reynolds equation follows Gross [27]. The derivation of the cylindrical shell equation is given in Section 2.2, and the Reynolds equation is is given in Section 2.4.

In our tape model for the foil bearing problem, we take the surface of the cylinder, around which the tape is wrapped, as the reference configuration. Barlow derived similar equations to ours [4]. This choice allows us to study large angle of wraps, unlike some of the previous work [58, 2, 1, 11, 24, 29, 30]. Using this reference configuration complicates the geometry, and leads to a segmented tape equation which is described in Section 2.3. The tape-guide spacing is defined in a short section, at the end of the chapter.

2.2 Equation of Motion of the Tape

Derivation of a plate or shell theory involves making several order-of-magnitude, and extensibility assumptions, such as the ones made by Love listed below. Leissa [40] has an extensive review of the literature on the different forms of the cylindrical shell equations based on different assumptions. In our derivation below we consider the terms of the equation of motion that are common to all of the investigators mentioned by Leissa. This form of the equation is also coincident with the forms given by Flügge and Timoshenko.

The tape-guide configuration is shown in Figure 2-1. The tape is wrapped with the wrap angle θ, around a cylindrical guide that has a radius R. Depending on the application, the tape extends out of the wrap zone in a straight line and it is supported by a guide pin at each end. Tape dynamics is viewed in a Eulerian frame. A fixed Cartesian coordinate system is placed *on* the left hand side pin. In this system the circumferential direction is x, the axial direction is y and the radial direction is z. The total length of the tape is L_x and the width of the tape is L_y. The limits of the straight parts of the tape are located at $x = L_{x_1}$, and $x = L_{x_2}$.

The equation of motion of a cylindrical shell derived in this section applies also to the flat parts of the tape as the tape's radius of curvature ($R \to \infty$) is the only parameter that is different in the flat parts. The equation of equilibrium of a cylindrical shell is obtained by considering the balance of forces acting on the middle surface of the shell element as shown in Figure 2-2. The equilibrium equations are simplified by using the following assumptions which were first given by Love, [20, 40]:

1. *The thickness of the shell is small compared with the other dimensions of the shell.*

2. *Normals to undeflected middle surface remain straight and normal to the deflected middle surface, and they do not experience any extension.*

3. *The transverse normal stress, σ_z may be neglected compared to other stresses.*

4. *All displacements are small so that they are negligible compared with the radii of*

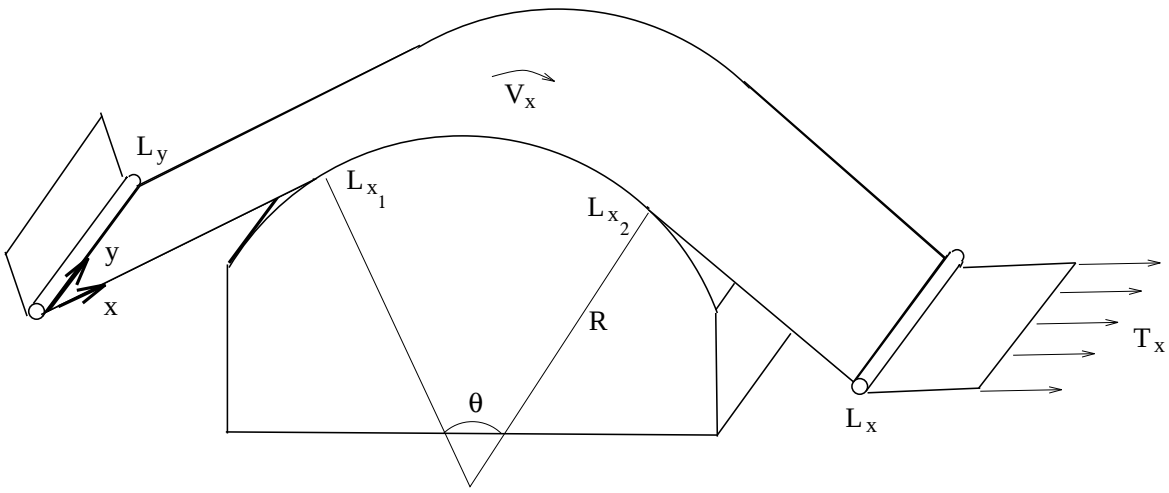

Figure 2-1: The head tape configuration. The warp angle is θ and the guide radius is R. The tape is modeled by a cylindrical shell in the wrap zone, and by plates outside the wrap zone. The transition occurs at locations $x = L_{x_1}$, and $y = L_{x_2}$.

curvature of the middle surface and their first derivatives are negligible compared to unity.

The forces and moments acting on the middle surface are obtained by using the *stress resultants* which are determined by integrating the stresses acting on the side faces of the shell element shown in Figure 2-2.

$$N_x = \int_{-c/2}^{c/2} \sigma_x dz \tag{2.1}$$

$$N_y = \int_{-c/2}^{c/2} \sigma_y (1 + \frac{z}{R}) dz \tag{2.2}$$

$$N_{xy} = \int_{-c/2}^{c/2} \tau_{xy} dz \tag{2.3}$$

$$N_{yx} = \int_{-c/2}^{c/2} \tau_{yx} (1 + \frac{z}{R}) dz \tag{2.4}$$

$$Q_x = -\int_{-c/2}^{c/2} \tau_{xz} dz \tag{2.5}$$

$$Q_y = -\int_{-c/2}^{c/2} \tau_{yz} (1 + \frac{z}{R}) dz \tag{2.6}$$

$$M_x = -\int_{-c/2}^{c/2} \sigma_x z dz \tag{2.7}$$

$$M_y = -\int_{-c/2}^{c/2} \sigma_y (1 + \frac{z}{R}) z dz \tag{2.8}$$

$$M_{xy} = -\int_{-c/2}^{c/2} \tau_{xy} z dz \tag{2.9}$$

$$M_{yx} = -\int_{-c/2}^{c/2} \tau_{yx} (1 + \frac{z}{R}) z dz \tag{2.10}$$

where, σ_x and σ_y are the normal stresses acting in the x and y directions, respectively. The shear stresses τ_{xy} and τ_{yx} act on the side faces of the shell element with unit normals in the x and y directions, respectively. Also, note that the terms involving $(1 + \frac{z}{R})$ represent the fact that length of the the curved sides of the cylindrical shell element changes with z. See Figure 2-2.

The equilibrium equations are obtained by taking the summation of the force and the moment vectors in the x, y and z directions. Upon examining Figure 2-2 one would notice that due to the curvature of the shell we need to consider the z component of N_x in writing the z-direction force equilibrium. Following Timoshenko, this component is given as $N_x(\frac{1}{R} + \frac{\partial^2 w}{\partial x^2} + \frac{1}{R}\frac{\partial u}{\partial x})$, [64, page450][1]. A similar consideration needs to be made for Q_x in the x-direction force equilibrium. Other stress resultant components also affect all three of the force equilibrium equations. However, all of these resultants are multiplied by the derivatives of the displacements, therefore any effects on the equilibrium equations due to the product of the other stress resultants and the derivatives of the displacements are neglected. The only product that is kept in the equilibrium equations is the term mentioned above in the z-direction equilibrium, as the magnitude of N_x prevents us from neglecting its product with $(\frac{1}{R} + \frac{\partial^2 w}{\partial x^2} + \frac{1}{R}\frac{\partial u}{\partial x})$.

in the x-direction,

$$\frac{\partial N_x}{\partial x} + \frac{\partial N_{yx}}{\partial y} - \frac{Q_x}{R} = 0 \tag{2.11}$$

in the y-direction,

$$\frac{\partial N_y}{\partial y} + \frac{\partial N_{xy}}{\partial x} = 0 \tag{2.12}$$

[1]The displacements that the shell experiences are decomposed as u, v, and w, in x, y, and z-directions, respectively.

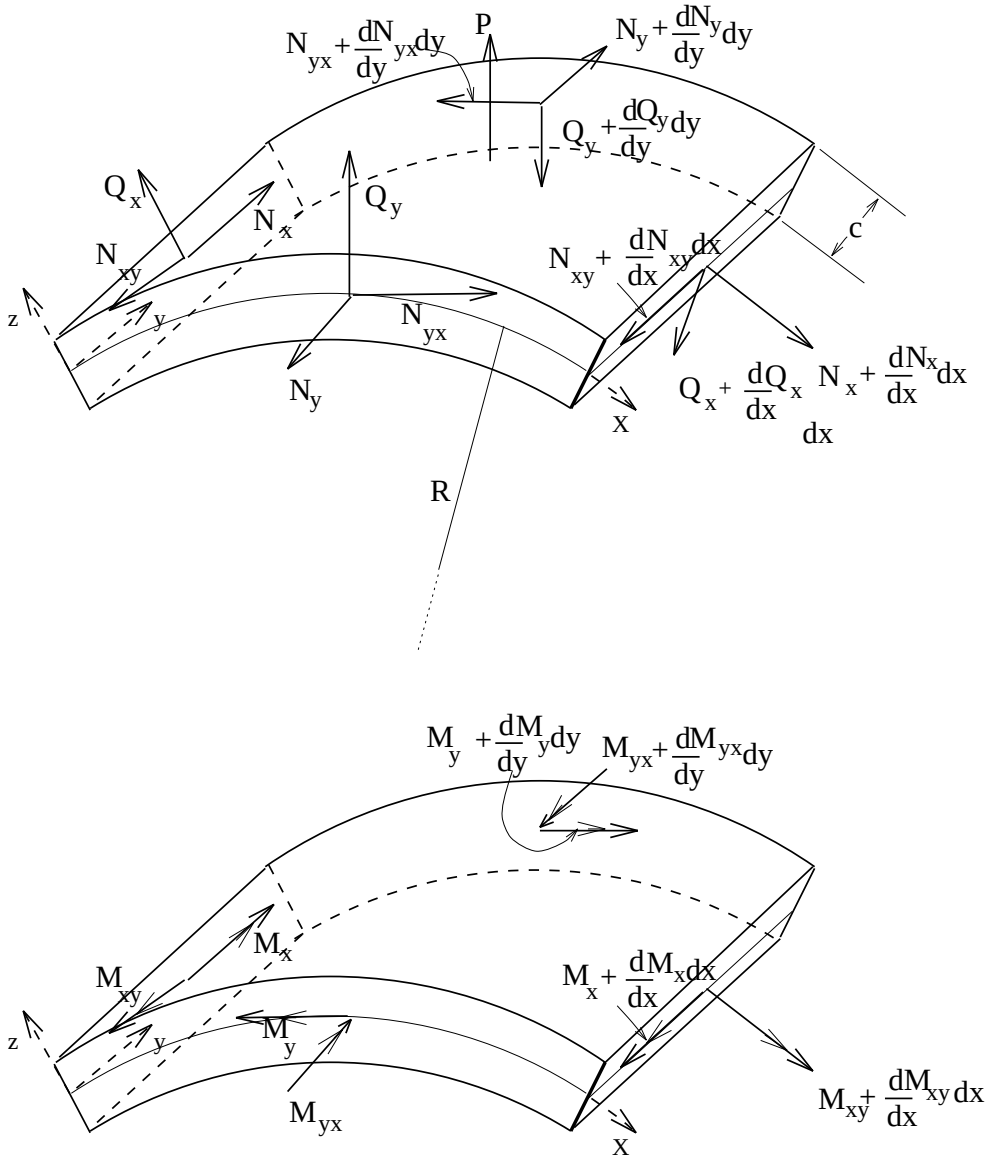

Figure 2-2: Cylindrical shell element

in the z-direction,

$$\frac{\partial Q_x}{\partial x} + \frac{\partial Q_y}{\partial y} + N_x(\frac{1}{R} + \frac{\partial^2 w}{\partial x^2} + \frac{1}{R}\frac{\partial u}{\partial x}) = p \tag{2.13}$$

where $p(x, y)$ is the radially applied external pressure. The static equilibrium of the moments are as follows:

about the x-axis,

$$\frac{\partial M_y}{\partial x} + \frac{\partial M_{xy}}{\partial x} - Q_y = 0 \tag{2.14}$$

about the y-axis,

$$\frac{\partial M_x}{\partial x} + \frac{\partial M_{yx}}{\partial y} - Q_x = 0 \tag{2.15}$$

about the z-axis,

$$RN_{yx} - RN_{xy} + M_{xy} = 0 \tag{2.16}$$

Transverse shear force resultants Q_x and Q_y can be eliminated from (2.11) and (2.13) by using (2.14) and (2.15). Thus, these two equations take the following forms,

$$\frac{\partial N_x}{\partial x} + \frac{\partial N_{yx}}{\partial y} - \frac{1}{R}\frac{\partial M_x}{\partial x} - \frac{1}{R}\frac{\partial M_{yx}}{\partial y} = 0 \tag{2.17}$$

$$\frac{\partial^2 M_x}{\partial x^2} + \frac{\partial^2 M_{xy}}{\partial x \partial y} + \frac{\partial^2 M_{yx}}{\partial y \partial x} + \frac{\partial^2 M_y}{\partial y^2} + N_x(\frac{1}{R} + \frac{\partial^2 w}{\partial x^2} + \frac{1}{R}\frac{\partial u}{\partial x}) = p(x, y) \tag{2.18}$$

Hooke's law establishes the isotropic elastic relations between the stresses and the strains.

$$\sigma_x = \frac{E}{1 - \nu^2}(\epsilon_x + \nu\epsilon_y) \tag{2.19}$$

$$\sigma_y = \frac{E}{1 - \nu^2}(\epsilon_y + \nu\epsilon_x) \tag{2.20}$$

$$\tau_{xy} = \frac{E}{2(1 + \nu)}\gamma_{xy} \tag{2.21}$$

where, ϵ_x and ϵ_y are the normal strains in x and y-directions, γ_{xy} is the shear strain, E is Young's modulus and ν is the Poisson's ratio. These strains are related to the displacements in the shell through geometric constraints, [20],

$$\epsilon_x = \frac{\partial u}{\partial x} - \frac{z}{R}\frac{1}{R + z}\frac{\partial^2 w}{\partial \theta^2} + \frac{w}{R + z} \tag{2.22}$$

$$\epsilon_y = \frac{\partial v}{\partial y} - z\frac{\partial^2 w}{\partial y^2} \tag{2.23}$$

$$\gamma_{xy} = \frac{1}{R+z}\frac{\partial v}{\partial \theta} + \frac{R+z}{R}\frac{\partial u}{\partial x} - \frac{\partial^2 w}{\partial \theta \partial y}(\frac{z}{R} + \frac{z}{R+z}) \tag{2.24}$$

where, the circumferential coordinate is, $x = R\theta$. For a thin shell, variations through the thickness, z, can be neglected with respect to the radius, R, (i.e. $z \ll R$). This assumption applies to the stress resultants, (2.2- 2.10), and to strain displacement relations, (2.22-2.24). If we further assume that the effect of bending moments on the in-plane stress resultants is negligible, we can express the stress resultants in terms of the displacements as follows:

$$N_x = \frac{Ec}{1-\nu^2}(\frac{\partial u}{\partial x} + \frac{w}{R} + \nu\frac{\partial v}{\partial y}) \tag{2.25}$$

$$N_y = \frac{Ec}{1-\nu^2}(\frac{\partial v}{\partial y} + \nu\frac{\partial u}{\partial x} + \nu\frac{w}{R}) \tag{2.26}$$

$$N_{xy} = N_{yx} = \frac{Ec}{2(1+\nu)}(\frac{\partial v}{\partial x} + \frac{\partial u}{\partial y}) \tag{2.27}$$

$$M_x = D(\frac{\partial^2 w}{\partial x^2} + \nu\frac{\partial^2 w}{\partial y^2}) \tag{2.28}$$

$$M_y = D(\frac{\partial^2 w}{\partial y^2} + \nu\frac{\partial^2 w}{\partial x^2}) \tag{2.29}$$

$$M_{xy} = M_{yx} = D(1-\nu)\frac{\partial^2 w}{\partial x \partial y} \tag{2.30}$$

See Table 2.1 for the definition of *bending stiffness*, D. Another result of neglecting the trapezoidal shape of the curved side (i.e. $z \ll R$) is that the force resultants N_{xy} and N_{yx}, and the moment resultants M_{xy} and M_{yx} become equal to each other, respectively. However, this condition causes the violation of equation (2.16), and it is a weakness of the theory [20].

In this thesis we are interested in the radial equilibrium of the cylindrical shell. Therefore, we neglect the effect of the in-plane displacements u and v on the strain displacement relations and the radial equilibrium. Based on this assumption Equations (2.25-2.30) are simplified, and carry only the terms involving the radial displacement, w, and its derivatives.

As the tape has an initial tension, T_x, in the undeformed state, the in-plane stress resultant, N_x, can be written as a superposition of the initial tension, and the tension due to shell displacement (Equation (2.25)), as follows:

$$N_x = T_x + \frac{Ec}{1-\nu^2}\frac{w}{R} \tag{2.31}$$

Thus when $w = 0$ the in-plane stress resultant in the x-direction becomes, $N_x = T_x$.

Using Equation (2.31), and the stress-resultants, (2.25-2.30), in the static equilibrium equation in the z-direction, (2.18), and assuming that the product of displacement, w with its derivatives is negligible, the following equation is reached,

$$D\nabla^4 w + Kw - T_x\frac{\partial^2 w}{\partial x^2} = p - \frac{T_x}{R} \tag{2.32}$$

This is the equation of equilibrium of a cylindrical shell that is subject to radial pressure, p, and circumferential tension, T_x. See Table 2.1 below for the definition of *shell stiffness,* K. Note that for a plate the shell stiffness term becomes zero, but the rest of the terms are the same as in Equation (2.32). See Section 2.3 for more on this issue.

The inertial forces are added to this equation by the virtue of D'Alembert's principle. As the tape is in motion, the inertial forces are given by $\rho_a \frac{D^2 w}{Dt^2}$, where the material time derivative, $\frac{D}{Dt}$, is essential in properly accounting for transport effects of the tape velocity in the Eulerian frame, [70]. For the case of zero tape velocity this reduces to differential, $\frac{\partial}{\partial t}$. The material time derivative of the displacement w is given as follows:

$$\frac{Dw}{Dt} = \frac{\partial w}{\partial t} + V_x\frac{\partial w}{\partial x} + V_y\frac{\partial w}{\partial y} + V_z\frac{\partial w}{\partial z} \tag{2.33}$$

where, V_x, V_y and V_z are the tape's velocity components in the x, y and z directions, respectively. By observing that V_y and V_z are zero for the tape transport problem the equation of motion for the tape becomes,

$$D\nabla^4 w + Kw - T_x\frac{\partial^2 w}{\partial x^2} + \rho_a(V_x^2\frac{\partial^2 w}{\partial x^2} + 2V_x\frac{\partial^2 w}{\partial x \partial t} + \frac{\partial^2 w}{\partial t^2}) = p - \frac{T_x}{R} \tag{2.34}$$

Variables of this equation are given in Table 2.1.

D	$\frac{Ec^3}{12(1-\nu^2)}$	Bending stiffness
K	$\frac{Ec}{R^2(1-\nu^2)}$	Shell stiffness
E		Young's modulus of the shell
ν		Poisson's ratio of the shell
c		Thickness of the shell
ρ_a		Areal density of the shell
$\frac{T_x}{R}$		Belt wrap pressure
R		Shell radius
T_x		Circumferential tension
V_x		Shell velocity in the circumferential direction
t		time
x		Circumferential coordinate
y		Axial coordinate
∇^4		Biharmonic operator

Table 2.1: Variables of the equation of motion of the cylindrical shell.

2.2.1 Boundary Conditions and Initial Conditions of the Shell Equation

The boundary conditions of the tape are such that the bending moment M_y and the equivalent shear force V_y vanish on the free edges along the lateral sides of the tape. The equivalent shear force is a combination of the shear force, Q_y, and the gradient of the twisting moments, $\frac{\partial M_{xy}}{\partial x}$. In terms of the radial displacements this is given as,

$$Q_y^{eq} = D[\frac{\partial^3 w}{\partial y^3} + (2-\nu)\frac{\partial^3 w}{\partial x^2 \partial y}] \tag{2.35}$$

[64]. The tape is supported by two guide pins on the two side boundaries. This support is modeled as a simple support in which the bending moment M_x and the displacement w are zero. See Figure 2-1 for the locations of the free and simply supported boundaries.

Simply Supported Sides:

Zero Moment for $x = 0, L_x$, and $0 \leq y \leq L_y$

$$M_x = D[\frac{\partial^2 w}{\partial x^2} + \nu \frac{\partial^2 w}{\partial y^2}] = 0 \tag{2.36}$$

Zero Displacement for $x = 0, L_x$, and $0 \leq y \leq L_y$

$$w = 0 \tag{2.37}$$

Free Edges :

Zero Moment for $y = 0, L_y$, and $0 \leq x \leq L_x$

$$M_y = D[\frac{\partial^2 w}{\partial y^2} + \nu \frac{\partial^2 w}{\partial x^2}] = 0 \tag{2.38}$$

Zero Equivalent Shear Force for $y = 0, L_y$, and $0 \leq x \leq L_x$

$$V_y = D[\frac{\partial^3 w}{\partial y^3} + (2 - \nu) \frac{\partial^3 w}{\partial x^2 \partial y}] = 0 \tag{2.39}$$

Solution of Equation (2.34) also requires two initial conditions for integration in the time domain.

Initial Conditions :

Initial Displacement for $t = 0$

$$w(x, y, 0) = w^o(x, y) \tag{2.40}$$

Initial Displacement Velocity for $t = 0$

$$\frac{\partial w(x, y, 0)}{\partial t} = v^o(x, y) \tag{2.41}$$

Here, w^o, v^o are two spatial functions to be defined.

2.3 Tape Geometry

Figure 2-3 shows the side view of the tape configuration. The tape is wrapped around the cylindrical guide for a wrap angle of $\theta = \theta_L + \theta_R$. It extends tangentially away from

the guide, outside this wrapping region, over the "entry" and an "exit" regions. It is supported by guide pins which are placed at $(\bar{X}, \bar{Y}) = (0, 0)$ and $(\bar{X}, \bar{Y}) = (L, 0)$ as shown in Figure 2-3.

The flat and curved parts of the tape have two different radii. In the first, and the third regions the tape is flat with an infinite radius. In the second region the tape follows the curvature of the guide and its radius is identical to that of the guide,

$$R = \begin{cases} \infty, & 0 \leq x \leq L_{x1}, \quad \text{(region 1)} \\ R, & L_{x1} \leq x \leq L_{x2}, \quad \text{(region 2)} \\ \infty, & L_{x2} \leq x \leq L_x, \quad \text{(region 3)} \end{cases} \tag{2.42}$$

In the first and third regions we model the tape as a plate, and in the second region we model it as a cylindrical shell. This requires the shell stiffness, K, to be modified as follows:

$$K = \begin{cases} 0 & 0 \leq x \leq L_{x1} \\ \frac{Ec}{R^2(1-\nu^2)} & L_{x1} \leq x \leq L_{x2} \\ 0 & L_{x2} \leq x \leq L_x \end{cases} \tag{2.43}$$

The belt wrap pressure $\frac{T_x}{R}$ is zero on the flat parts of the tape. We define a new variable, P_{BW}, as follows:

$$P_{BW} = \begin{cases} 0 & 0 \leq x \leq L_{x1} \\ \frac{T_x}{R} & L_{x1} \leq x \leq L_{x2} \\ 0 & L_{x2} \leq x \leq L_x \end{cases} \tag{2.44}$$

In our approach the reference configuration of the tape is the cylinder's surface in the second region, and the lines connecting the tangency points to the far-end simple supports in the first and third regions. See Figure 2-3. The reference configuration for the Reynolds equation, on the other hand, is on the guide surface. In order to distinguish these two reference configurations two different notations are used for each system. The "x-coordinate" is on the undeflected tape as described above, and it is related to the tape. The "s-coordinate" is placed on the surface of the rigid guide, and it is related to the Reynolds equation.

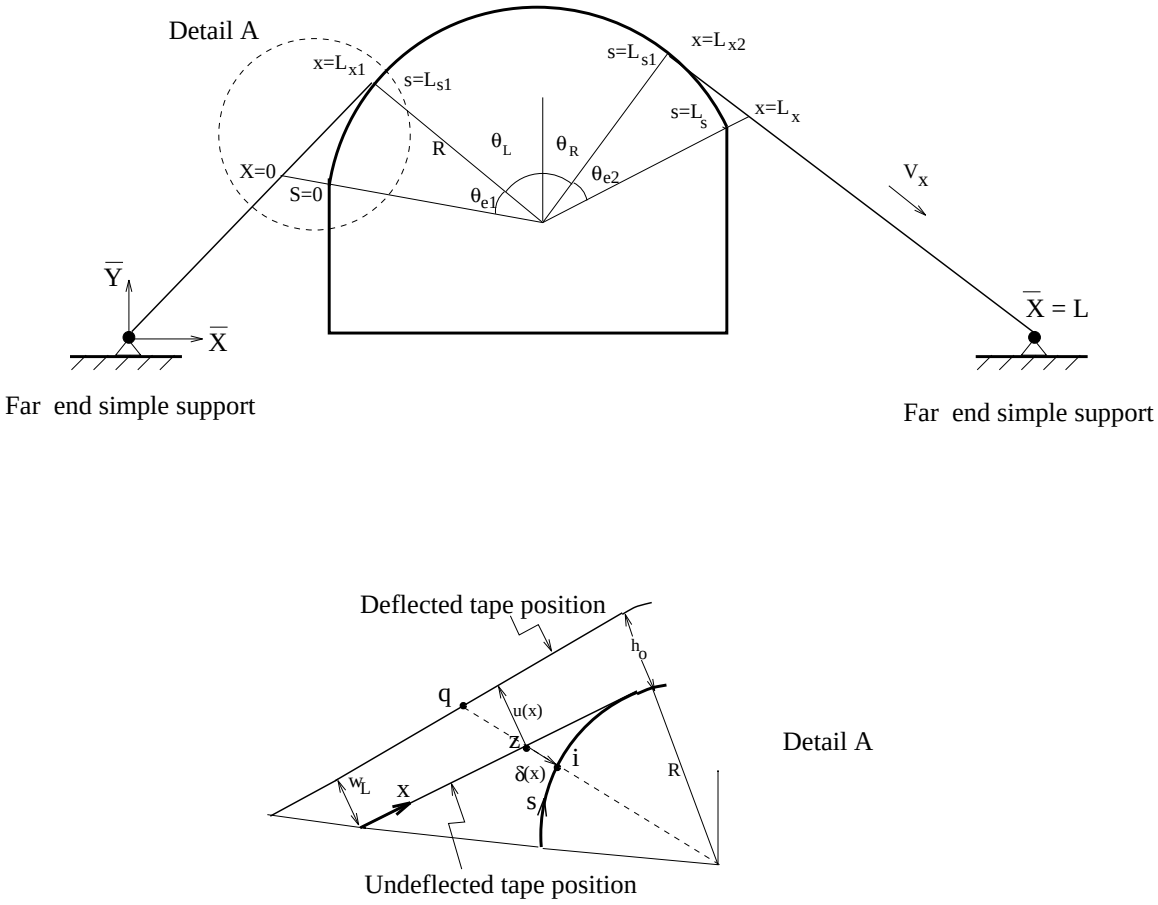

Figure 2-3: Tape geometry for the large angle of wrap analysis. Shown are the undeflected (reference) and deflected shapes.

On the x-coordinate system, the total tape length between two supports is L_x. The tangency points between the tape and the guide are located at $x = L_{x1}$ and $x = L_{x2}$. On the s-coordinate system the counterparts of L_x, L_{x1}, and L_{x2} are L_s, L_{s1}, and L_{s2}, respectively.

The distance between the undeflected tape and the guide is denoted by $\delta(x)$, and it is given as follows:

$$\delta(x) = \begin{cases} \sqrt{(\bar{X}_i - \bar{X}_z)^2 + (\bar{Y}_i - \bar{Y}_z)^2}, & 0 \leq x \leq L_{x1} \\ 0 & L_{x1} \leq x \leq L_{x2} \\ \sqrt{(\bar{X}_i - \bar{X}_z)^2 + (\bar{Y}_i - \bar{Y}_z)^2}, & L_{x2} \leq x \leq L_x \end{cases} \tag{2.45}$$

See Figure 2-3 for the locations of points i and z.

2.4 The Modified Reynolds Equation for Gas Lubrication

In this section the derivation of the modified Reynolds equation for air lubrication is presented. Lubrication takes place in very narrow gaps in which we can assume that there is only boundary layer flow. This kind of flow is subject to very large velocity gradients across the depth of the lubricant, and therefore it is dominated by the viscous forces. The ratio of the inertial fluid forces (the first group of terms in Equation (2.46)) to viscous fluid forces (the second group of terms), is given by the *modified Reynolds number* [27],

$$Re^* = \frac{\rho U}{B} \frac{h^2}{\mu U} \tag{2.46}$$

In this relation ρ is the fluid density, U is the bearing velocity, B is a characteristic bearing length, h is a characteristics bearing clearance and μ is the lubricant viscosity. The modified Reynolds number should be, $Re^* \ll 1$, for a flow to be dominated by viscous forces.

In the lubrication zone the fluid adheres to the lubricated surfaces. This situation creates a *no-slip* boundary condition. If the lubricant is modeled by a Newtonian fluid,

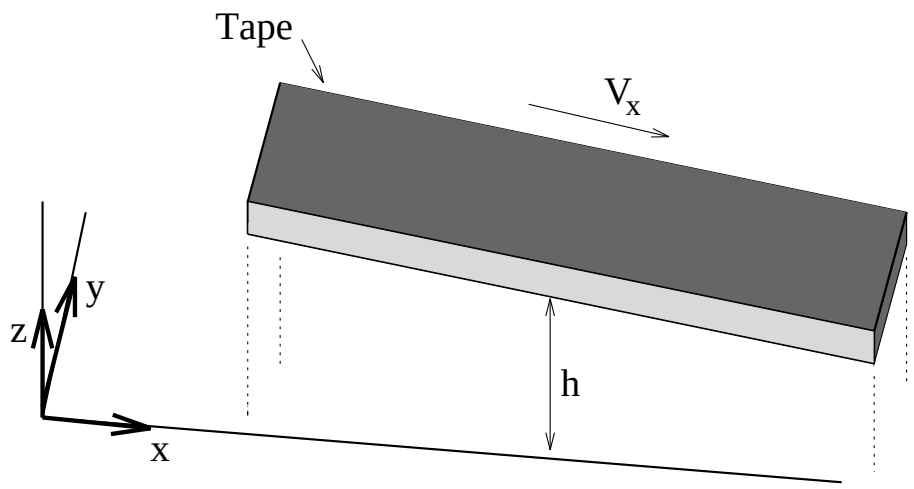

Figure 2-4: The coordinate system for the lubrication of a tape.

(in which the velocity gradient is linearly related to shearing stress in the fluid), then the momentum equations corresponding to such a fluid can be integrated through the gap thickness and combined with the mass continuity equation to give a single equation that governs the pressure distribution in a lubrication process. The equation derived this way is called the *Reynolds equation.*

However, when the lubrication takes place in clearances that are comparable to molecular mean free path of the lubricant, the fluid velocity on the boundaries no longer satisfies the no-slip conditions, and should be modified with the slip velocity[2]. This was suggested by Burgdorfer (1959) [13], and later modified by Hsia (1983), [33], and Mitsuya (1992), [45]. The equation obtained by using boundary conditions corrected for slip is called the *modified Reynolds equation.* The measure of the molecular rarefaction is the Knudsen number, Kn,

$$Kn = \frac{\lambda}{h} \tag{2.47}$$

where λ is the length of the mean free path of the lubricant molecules. The unmodified Reynolds equation is valid for $Kn < 0.01$ where as the modified Reynolds equation can

[2]The slip velocity is defined in the next section.

be used for higher Knudsen numbers[3].

The assumptions used in the derivation of the modified Reynolds equation, given in the next section, are summarized as follows [27]:

1. *The fluid is Newtonian.*
2. *Vertical velocity components in the fluid are negligible compared to horizontal components.*
3. *Inertial terms in the momentum equation are negligible compared to viscous terms.*
4. *The flow is isothermal.*
5. *The gas behaves as an ideal gas, i.e. $\rho \propto p$, where p is the pressure.*

2.4.1 Derivation of the Modified Reynolds Equation

The *Navier-Stokes* equations govern the momentum balance in a given control volume of a lubricating fluid. By assuming that the lubricating fluid is in steady state, the inertial terms of the Navier-Stokes equations can be neglected. Considering that the thickness of the lubricating film is much smaller compared to its length and width, we omit the z-direction variables and pressure gradients. We also neglect the body forces acting on the fluid. With these simplifications the Navier-Stokes equations reduce to the following momentum equations,

$$\frac{\partial p}{\partial x} = \frac{\partial}{\partial z}(\mu \frac{\partial \bar{u}}{\partial z}) \tag{2.48}$$

$$\frac{\partial p}{\partial y} = \frac{\partial}{\partial z}(\mu \frac{\partial \bar{v}}{\partial z}) \tag{2.49}$$

where, p is the fluid pressure, $\bar{u}$, and $\bar{v}$ are the fluid velocities in the x and y-directions, respectively, and μ is the viscosity of the fluid. The continuity equation determines the balance of mass in a control volume,

$$\frac{\partial \rho \bar{u}}{\partial x} + \frac{\partial \rho \bar{v}}{\partial y} + \frac{\partial \rho \bar{w}}{\partial z} + \frac{\partial \rho}{\partial t} = 0 \tag{2.50}$$

[3]Gans showed that the first order correction can be used for arbitrarily small clearances, [23].

In this equation $\bar{w}$ denotes the fluid velocity in the z-direction. When the lubricant is gas the density can be interchanged with pressure according to the fifth assumption stated at the end of the last section.

In the foil bearing problem the Knudsen number becomes considerably high, due to low flying height requirements. For this reason the slip correction factors as suggested, in the context of Reynolds equation, by Burgdorfer in 1959 are used to modify the no-slip boundary conditions [13]. The corrections derived by Burgdorfer came to be known as the first order corrections. Later Hsia and Domoto introduced the second order correction in 1983 [33], and Mitsuya introduced the 1.5-order correction in 1993 [45]. The slip velocity considering the second order effects is given as follows:

$$\bar{u}_{slip}\,|_{z=0} = (\frac{2-\sigma}{\sigma})\lambda[\frac{\partial \bar{u}}{\partial z} - \frac{\lambda}{2}\frac{\partial^2 \bar{u}}{\partial z^2}]_{z=0} \tag{2.51}$$

$$\bar{u}_{slip}\,|_{z=h} = (\frac{2-\sigma}{\sigma})\lambda[-\frac{\partial \bar{u}}{\partial z} - \frac{\lambda}{2}\frac{\partial^2 \bar{u}}{\partial z^2}]_{z=h} \tag{2.52}$$

where, σ is the momentum transfer ratio when an air molecule strikes a surface, and λ is the length of the mean free molecular path of the lubricating fluid. The combined coefficient $(\frac{2-\sigma}{\sigma})\lambda$ represents the distance the wall should be moved back to recover no-slip conditions, and it is called *the coefficient of slip*, [35]. The slip velocities for $\bar{v}$ are similar to above equations. We consider the first order correction term in this study. Then boundary conditions for the fluid velocity become,

$$\begin{aligned} \text{at } z = 0 \quad & \bar{u}(x,y,0) = V_x\,|_{z=0} + \bar{u}_{slip}\,|_{z=0} \\ & \bar{v}(x,y,0) = V_y\,|_{z=0} + \bar{v}_{slip}\,|_{z=0} \\ \text{at } z = h \quad & \bar{u}(x,y,h) = V_x\,|_{z=h} + \bar{u}_{slip}\,|_{z=h} \\ & \bar{v}(x,y,h) = V_y\,|_{z=h} + \bar{v}_{slip}\,|_{z=h} \end{aligned} \tag{2.53}$$

When we model linear recording with the foil bearing problem, we take the lower surface of the bearing as stationary and the upper surface moving only in the x-direction. However, for helical-scan recording both lower and upper surfaces are in motion. Therefore, to retain generality we keep all of the four surface speeds in the analysis, and we define

the following,

$$\begin{aligned} V_x^G &= V_x \mid_{z=0} \\ V_y^G &= V_y \mid_{z=0} \\ V_x &= V_x \mid_{z=h} \\ V_y &= V_y \mid_{z=h} \end{aligned} \tag{2.54}$$

The superscript G is used to denote the guide. After this definition, the boundary conditions for the velocities take their final form,

$$\begin{aligned} \text{at } z = 0 \quad \bar{u}(x,y,0) &= V_x^G + \lambda \tfrac{\partial \bar{u}}{\partial z} \mid_{z=0} \\ \bar{v}(x,y,0) &= V_y^G + \lambda \tfrac{\partial \bar{v}}{\partial z} \mid_{z=0} \\ \text{at } z = h \quad \bar{u}(x,y,h) &= V_x - \lambda \tfrac{\partial \bar{u}}{\partial z} \mid_{z=h} \\ \bar{v}(x,y,h) &= V_y - \lambda \tfrac{\partial \bar{v}}{\partial z} \mid_{z=h} \end{aligned} \tag{2.55}$$

Using these boundary conditions the momentum equations can be integrated through the thickness of the gap to give,

$$\bar{u} = \frac{1}{2\mu}\frac{\partial p}{\partial x}[z^2 - zh - h\lambda] + (V_x - V_x^G)[\frac{z+\lambda}{2\lambda + h}] + V_x^G \tag{2.56}$$

$$\bar{v} = \frac{1}{2\mu}\frac{\partial p}{\partial y}[z^2 - zh - h\lambda] + (V_y - V_y^G)[\frac{z+\lambda}{2\lambda + h}] + V_y^G \tag{2.57}$$

The momentum transfer ratio, σ, depends on the surface characteristics, and it is an experimentally determined constant. We are not aware of any study that has determined the momentum transfer ratio between air and the magnetic recording tape. Therefore, in Equations (2.55-2.57) the momentum transfer ratio is taken as one. This choice represents a case where all of the incident momentum of the air molecule is transferred to the surface, [35]. The modified Reynolds equation is obtained by using (2.56, 2.57) in the continuity equation and then integrating the result in the z-direction,

$$\begin{aligned} \tfrac{\partial}{\partial x}[h^3 p \tfrac{\partial p}{\partial x}(1 + 6\tfrac{\lambda_a}{h})] \quad + \quad & \tfrac{\partial}{\partial y}[h^3 p \tfrac{\partial p}{\partial y}(1 + 6\tfrac{\lambda_a}{h})] = \\ & 12\mu_a \tfrac{\partial ph}{\partial t} + 6\mu_a(V_x + V_x^G)\tfrac{\partial ph}{\partial x} + 6\mu_a(V_y + V_y^G)\tfrac{\partial ph}{\partial y} \end{aligned} \tag{2.58}$$

Note that the subscript a indicates that the variables have the properties of air. The variables used in this equation are explained in Table 2.2. The first term on the right

p	Lubricant pressure
h	Bearing clearance
V_x, V_y	Tape speeds in x and y directions.
V_x^G, V_y^G	Guide speeds in x and y directions.
μ_a	Air viscosity
λ_a	Mean free path length of air

Table 2.2: Variables of the Reynolds equation

hand side of Equation (2.58) is called the *squeeze term.* It characterizes the contribution of relative motion normal to the bearing surface. The second term on the right hand side is the *wedge term,* representing the contribution of the shape of the fluid film and the tangential motion of the surfaces [28].

2.4.2 Boundary Conditions

The boundary conditions of the Reynolds equation are such that the pressure is ambient, P_a, outside the head region and along the edges of the tape.

$$p(0, y) = p(L_x, y) = p(x, 0) = p(x, L_y) = P_a \tag{2.59}$$

2.5 Tape-Guide Spacing, h

The Reynolds equation and the tape equation are coupled by the variable h. This variable represents the distance between the tape and the surface of the rigid guide. It is defined as follows:

$$h(x, y, t) = w(x, y, t) + \delta(x, y) \tag{2.60}$$

Note that in this definition the tape deflection, w, is added to guide shape, δ, instead of being subtracted which is usually the case in the formulations in which the reference configuration is taken as the line connecting the simple supports, i.e. $\bar{Y} = 0$ in Figure 2-3.

2.6 Contact Pressure

Under some operating conditions the distance between the tape and the rigid guide becomes as low as the mean value of the surface roughness height of the matching surfaces. Such conditions include, low tape speeds and high tape tensions. In such cases the tape is supported by the combined action of the contact pressure, P_c, and air pressure, p. In our simulations the contact was encountered at the free edges of the tape where the net air pressure is zero. In this section two approaches that can be used to calculate a contact pressure value based on the distance between two surfaces are presented.

As the two surfaces approach each other the first contact occurs between the asperities. The behavior of a single asperity, based on the elastic, Hertzian-contact, is known from the study of Greenwood and Williamson, [26]. In this model all of the asperities are assumed to have spherical tips with radius, R_p and their distribution on the surface is assumed to follow a known statistical distribution, ϕ. The contact pressure, thus, can be expressed as a function of the tip radius, the mean surface roughness height, the density of the asperities, η, the elastic moduli, E, E_{guide}, and the Poisson's ratios, ν, ν_{guide}, of the two surfaces, and the tape-guide separation h,

$$P_c = \frac{4}{3}(\sigma_t R_p \eta) E_c (\frac{\sigma_t}{R_p})^{1/2} \int_h^\infty (z-h)^{3/2} \phi(z) dz \tag{2.61}$$

In general, the mean surface roughness height, σ_t, of the back side of a magnetic recording tape is considerably higher than the surface roughness of a steel guide. Therefore, in this study we neglect the latter. Another approach would be to compound the two roughnesses into one value as suggested by Bhushan, [8]. That would be a negligibly small change on σ_t. The composite modulus, E_c, is given as

$$E_c^{-1} = \frac{1-\nu^2}{E} + \frac{1-\nu_{guide}^2}{E_{guide}} \tag{2.62}$$

Bhushan used a Gaussian distribution for the statistical distribution of the asperities and used tabulated values for integration, and fitted the resulting curves into a power form

using least squares fit [8]. The equation for the contact pressure then becomes,

$$P_c = 0.57(\sigma_t R_p \eta) E_c (\frac{\sigma_t}{R_p})^{1/2} 10^{-(\frac{h}{1.4\sigma_t})^{1.54}} \tag{2.63}$$

Lacey, on the other hand, used an experimental approach to directly measure the contact pressure between the tape and a guide surface [39]. He used an interferometric technique in which he measured the tape-guide spacing, as the tape is statically pushed against a glass guide with varying tensions. The results are plotted and then curve-fitted to a second order polynomial, as follows:

$$P_c = \begin{cases} (\frac{\sqrt{P_m}}{\sigma_t}(\sigma_t - h))^2 & \text{if } h \leq \sigma_t \\ 0 & \text{if } h \geq \sigma_t \end{cases} \tag{2.64}$$

where, P_m is the pressure required to force the spacing, h to zero. The values of P_m and σ_t for chromium dioxide tape are reported as $4.72MPa$ and $93.4nm$, respectively, [39]. We feel that the empirical relation given in Equation (2.64) would represent the contact in magnetic tapes better than the theoretical relation given by Equation (2.63), because it directly measures some of the assumptions regarding asperity densities, η, and the uniformity of the asperity radius, R_p. This function is used for calculating the contact pressure on the right hand side of the equation of motion of the tape, (7.1).

Chapter 3

Solution Methods

3.1 Introduction

In this chapter the numerical approaches that we used to solve the two governing equations of our model of the foil bearing problem are presented. In order to solve the equation of motion of the cylindrical shell it is first put into a semidiscrete form using second order accurate finite difference equations. Then it is integrated in time using the so called "α-family" of methods (Hilbert-Hughes-Taylor method), [34]. Sections 3.2 and 3.3 show this development. Reynolds equation is solved using the alternating direction implicit (ADI) method, which is explained in Section 3.5. The solution technique for the Reynolds equation follows White and Nigam, [68]. Finally the algorithm for coupling the two equations in the transient domain is given in Section 3.6. This chapter is prepared in such a way that using the contained information the reader would be able reconstruct the building blocks of our solution method.

3.2 Spatial Discretization of the Equation of Motion of the Tape

The equation of motion of the tape is repeated below. Note that the biharmonic operator is given in its Cartesian form,

$$D[\frac{\partial^4 w}{\partial x^4} + 2\frac{\partial^4 w}{\partial x^2 \partial y^2} + \frac{\partial^4 w}{\partial y^4}] + Kw + (\rho_a V_x^2 - T_x)\frac{\partial^2 w}{\partial x^2} + 2\rho_a V_x \frac{\partial^2 w}{\partial x \partial t} + \rho_a \frac{\partial^2 w}{\partial t^2} = F \quad (3.1)$$

In this equation F represents sum of the gage pressure, $p - P_a$, the contact pressure, P_c, and the belt wrap pressure, P_{BW},

$$F = p + P_c - P_a - P_{BW} \quad (3.2)$$

The belt wrap pressure, P_{BW}, and the shell stiffness, K, are defined by Equations (2.44) and (2.43), respectively.

The discretization process consists of replacing the derivatives of Equation (3.1) with their finite difference equivalents, as given in Equations (3.8-3.14), and discretizing the tape into a rectangular mesh of nodes.

3.2.1 The Finite Difference Mesh

The tape is discretized to $M+2$ nodes in the x-direction and N nodes in the y-direction. See Figure 3-1. First and last of the $M+2$ nodes in the x-direction are placed on the simply supported boundaries. The displacements of these boundaries are known from the boundary conditions. Therefore, these two nodes fall out of the list of unknown nodes. The number of nodes in the x-direction at which displacement is calculated becomes M, and the number of unknowns in the y-direction is N. This discretization gives rise to $NEQ = N \times M$ nodes placed on the tape. Note that in Figure 3-1 the nodes at which the displacements are unknown are indicated by "+", whereas the nodes with known displacements are indicated by "•". The spacing between the nodes in the x and

y-directions are given by,

$$\Delta x = \frac{L_x}{M+1} \tag{3.3}$$

$$\Delta y = \frac{L_y}{N-1} \tag{3.4}$$

The location of a point (x, y) is given by the following pair on the discretized tape,

$$(x, y) \rightarrow (i\Delta x, (j-1)\Delta y) \tag{3.5}$$

where, i and j are the nodes in the x and y-directions. They range as follows,

$$\begin{aligned} 1 \leq i \leq M \\ 1 \leq j \leq N \end{aligned} \tag{3.6}$$

It is cumbersome to use (i, j) pairs to locate a node on the discretized tape from programming point of view. For this reason we assigned a node number, k, to every point on the discretized tape. The following numbering scheme is used:

$$k = (i-1)N + j \quad \text{where} \quad 1 \leq i \leq M \quad \text{and} \quad 1 \leq j \leq N \tag{3.7}$$

The point $k = 1$, or equivalently $(i, j) = (1, 1)$, corresponds to the lower left corner, $(\Delta x, 0)$, of the tape. The node numbers are augmented in the y-direction. This scheme results in the smallest half band width $(2N)$ for the stiffness matrix, that is introduced later in this chapter, provided that $N < M$.

3.2.2 The Finite Difference Equations

The tape equation, (3.1), and the boundary conditions, (2.36-2.39), are discretized in space by replacing the derivatives with the following second order accurate, $O(\Delta x^2)$, finite difference formulas, [61],

$$\frac{\partial w}{\partial x} \simeq \frac{1}{2\Delta x}(w_{k-N} - w_{k+N}) \tag{3.8}$$

$$\frac{\partial^2 w}{\partial x^2} \simeq \frac{1}{\Delta x^2}(w_{k-N} - 2w_k + w_{k+N}) \tag{3.9}$$

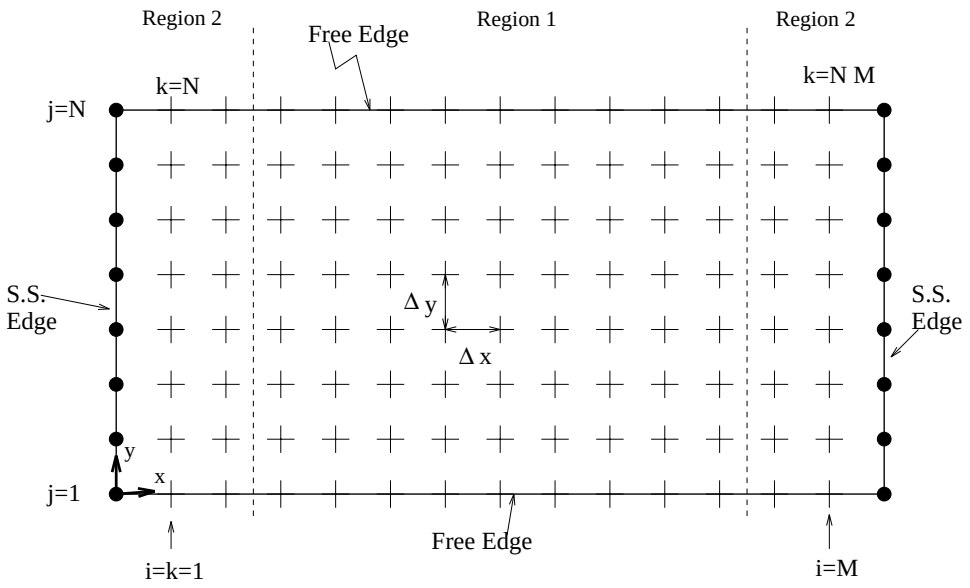

Figure 3-1: Discretized tape where x is the circumferential and y is the axial direction. The "+" indicates nodes at which the displacements are unknown. At "•"s displacements are known.

$$\frac{\partial^4 w}{\partial x^4} \simeq \frac{1}{\Delta x^4}(w_{k-2N} - 4w_{k-N} + 6w_k - 4w_{k+N} + w_{k+2N}) \tag{3.10}$$

$$\frac{\partial^3 w}{\partial y^3} \simeq \frac{1}{2\Delta y^3}(-w_{k-2} + 2w_{k-1} - 2w_{k+1} + w_{k+2}) \tag{3.11}$$

$$\frac{\partial^3 w}{\partial x^2 \partial y} \simeq \frac{1}{2\Delta x^2 \Delta y}(w_{k-N+1} - w_{k-N-1} - 2w_{k+1} + 2w_{k-1} + w_{k+N+1} - w_{k+N-1}) \tag{3.12}$$

$$\frac{\partial^4 w}{\partial y^4} \simeq \frac{1}{\Delta y^4}(w_{k-2} - 4w_{k-1} + 6w_k - 4w_{k+1} + w_{k+2}) \tag{3.13}$$

$$\frac{\partial^4 w}{\partial x^2 \partial y^2} \simeq \frac{1}{\Delta x^2 \Delta y^2}(w_{k-N-1} - 2w_{k-N} + w_{k_N+1} - 2w_{k-1} + 4w_k - 2w_{k+1} + w_{k+N-1} - 2w_{k+N} + w_{k+N+1}) \tag{3.14}$$

The first and second derivatives of w with respect to time, t, are not affected by the substitution of the finite difference approximations and they are retained in the equations, given below, as $\dot{w}_k$ and $\ddot{w}_k$, respectively.

On the free edges of the tape, $y = 0, L_y$, substitution of the finite difference equa-

tions gives rise to two rows of "fictitious" nodes (not shown in Figure 3-1). However, these nodes also appear in the discretized form of the free edge boundary conditions, Equations (2.38) and (2.39). Therefore, the fictitious nodes are eliminated from the tape equation by using the free edge boundary conditions.

On the simply supported edges of the tape, $x = 0, L_x$, the displacement is known from the boundary condition, (2.37), therefore, the tape equation is not evaluated there. Evaluation of the zero moment boundary condition, (2.36), on the pin boundaries, and the tape equation at $x = \Delta x, L_x - \Delta x$ gives rise to one column of fictitious nodes (not shown in Figure 3-1, either) extending beyond the simply supported boundaries. These nodes are eliminated from the tape equation as described above. Thus, for each node on the tape, an ordinary differential equation (ODE) in time, t, is obtained. Elimination of the fictitious nodes is straight forward but laborious. For this reason only the resulting equations are shown below. Note that nodes affected by the simple support boundary conditions are in **Region 2**. All of the other nodes are in **Region 1**.

Region 1: $2N + 1 \leq k \leq N(M-2)$

Lower Free Edge, $(2N+1, 3N+1, \ldots, (M-3)N+1)$:

$$\begin{aligned} &Q_1(w_{k-2N} + w_{k+2N}) + Q_2 w_{k-2} + Q_3(w_{k+N-1} + w_{k-N-1}) + Q_4(w_{k-N} + w_{k+N}) + \\ &Q5 w_{k-1} + (Q_6 + Q_{M_2}) w_k + Q_{t_2}(\dot{w}_{k+N} - \dot{w}_{k-N}) + Q_{t_1}\ddot{w}_k = F_k \end{aligned} \tag{3.15}$$

Nodes Adjacent to the Lower Free Edge, $(2N+2, 3N+2, \ldots, (M-3)N+2)$:

$$\begin{aligned} &Q_7(w_{k-2N} + w_{k+2N}) + Q_8 w_{k-2} + Q_9 w_{k+1} + Q_{10}(w_{k-N+1} + w_{k+N+1}) + \\ &(Q11 + Q_{M_2}) w_k + Q_{12}(w_{k-N-1} + w_{k+N-1}) + (Q_{13} + Q_{M_1})(w_{k-N} + w_{k+N}) + \\ &Q_{14} w_{k-1} + Q_{t_2}(\dot{w}_{k+N} - \dot{w}_{k-N}) + Q_{t_1}\ddot{w}_k = F_k \end{aligned} \tag{3.16}$$

Middle Nodes,

$(k = (2N+3, \ldots 3N-2), (3N+3, \ldots 4N-2), \ldots ((M-3)N+3, ..(M-2)N-2))$:

$$Q_7(w_{k-2N} + w_{k+2N}) + Q_8(w_{k-2} + w_{k+2}) + Q_{12}(w_{k-N-1} + w_{k-N+1} + w_{k+N-1} + w_{k+N+1}) + (Q15 + Q_{M_2})w_k + (Q_{13} + Q_{M_1})(w_{k-N} + w_{k+N}) + Q_{14}(w_{k-1} + w_{k+1}) + Q_{t_2}(\dot{w}_{k+N} - \dot{w}_{k-N}) + Q_{t_1}\ddot{w}_k = F_k \tag{3.17}$$

Nodes Adjacent to the Upper Free Edge, $(k = 3N-1, 4N-1, \ldots, (M-2)N-1)$:

$$Q_7(w_{k-2N} + w_{k+2N}) + Q_8 w_{k+2} + Q_9 w_{k-1} + Q_{10}(w_{k-N-1} + w_{k+N-1}) + (Q_{11} + Q_{M_2})w_k + Q_{12}(w_{k-N+1} + w_{k+N+1}) + (Q_{13} + Q_{M_1})(w_{k-N} + w_{k+N}) + Q_{14}w_{k+1} + Q_{t_2}(\dot{w}_{k+N} - \dot{w}_{k-N}) + Q_{t_1}\ddot{w}_k = F_k \tag{3.18}$$

Upper Free Edge, $(k = 3N, 4N, \ldots, (M-2)N)$:

$$Q_1(w_{k-2N} + w_{k+2N}) + Q_2 w_{k+2} + Q_3(w_{k-N+1} + w_{k+N+1}) + (Q_4 + Q_{M_1})(w_{k-N} + w_{k+N}) + Q5 w_{k+1} + (Q_6 + Q_{M_2})w_k + Q_{t_2}(\dot{w}_{k+N} - \dot{w}_{k-N}) + Q_{t_1}\ddot{w}_k = F_k \tag{3.19}$$

Region 2: $1 \le k \le 2N$ **and** $MN - 2N + 1 \le k \le MN$

In order to save space we will only give the equations written for the left-hand -side simple support. The equations that apply to the right-hand-side simple support can be obtained by replacing N with $-N$, and w_L with w_R in the below equations. The displacements of the left and right hand side supports are given by w_L and w_R as shown in Figure 2-3.

Free lower edge, $k = 1$:

$$Q_1 w_{k+2N} + Q_2 w_{k+2} + Q_3 w_{k+N+1} + (Q_4 + Q_{M_1})w_{k+N} + Q_5 w_{k+1} + (Q_6 + Q_{M_2} - Q_1)w_k + Q_{t_2}(\dot{w}_{k+N} - \dot{w}_{k-N}) + Q_{t_1}\ddot{w}_k = F_k - (2Q_1 + Q_3 + Q4 + Q_{M_1})w_L \tag{3.20}$$

$\underline{k = 2:}$

$$Q_7 w_{k+2N} + Q_8 w_{k+2} + Q_9 w_{k-1} + Q_{10} w_{k+N-1} + (Q_{11} + Q_{M_2} - Q_7) w_k + Q_{12} w_{k+N+1} + (Q_{13} + Q_{M_1}) w_{k+N} + Q_{14} w_{k+1} + Q_{t_2}(\dot{w}_{k+N} - \dot{w}_{k-N}) + Q_{t_1} \ddot{w}_k = F_k - (2Q_7 + Q_{10} + Q_{12} + Q_{13} + Q_{M_1}) w_L \tag{3.21}$$

$\underline{\text{Middle nodes, } 3 \leq k \leq N-2:}$

$$Q_7 w_{k+2N} + Q_8 (w_{k-2} + w_{k+2}) + Q_{12} (w_{k+N-1} + w_{k+N+1}) + (Q_{15} + Q_{M_2} - Q_7) w_k + (Q_{13} + Q_{M_1}) w_{k+N} + Q_{14} (w_{k-1} + w_{k+1}) + Q_{t_2}(\dot{w}_{k+N} - \dot{w}_{k-N}) + Q_{t_1} \ddot{w}_k = F_k - (2Q_7 + 2Q_{12} + Q13 + Q_{M_1}) w_L \tag{3.22}$$

$\underline{k = N-1:}$

$$Q_7 w_{k+2N} + Q_8 w_{k-2} + Q_9 w_{k+1} + Q_{10} w_{k+N+1} + (Q_{11} + Q_{M_2} - Q_7) w_k + Q_{12} w_{k+N-1} + (Q_{13} + Q_{M_1}) w_{k+N} + Q_{14} w_{k-1} + Q_{t_2}(\dot{w}_{k+N} - \dot{w}_{k-N}) + Q_{t_1} \ddot{w}_k = F_k - (2Q_7 + Q_{10} + Q_{12} + Q_{13} + Q_{M_1}) w_L \tag{3.23}$$

$\underline{\text{Free upper edge, } k = N:}$

$$Q_1 w_{k+2N} + Q_2 w_{k-2} + Q_3 w_{k+N-1} + (Q_4 + Q_{M_1}) w_{k+N} + Q_5 w_{k-1} + (Q_6 + Q_{M_2} - Q_1) w_k + Q_{t_2}(\dot{w}_{k+N} - \dot{w}_{k-N}) + Q_{t_1} \ddot{w}_k = F_k - (2Q_1 + Q_3 + Q4 + Q_{M_1}) w_L \tag{3.24}$$

$\underline{k = N+1:}$

$$Q_1 w_{k+2N} + Q_2 w_{k+2} + Q_3 (w_{k-N+1} + w_{k+N+1}) + (Q_4 + Q_{M_1})(w_{k+N} + w_{k-N}) + Q_5 w_{k+1} + (Q_6 + Q_{M_2}) w_k + Q_{t_2}(\dot{w}_{k+N} - \dot{w}_{k-N}) + Q_{t_1} \ddot{w}_k = F_k - Q_1 w_L \tag{3.25}$$

$\underline{k = N+2:}$

$$Q_7 w_{k+2N} + Q_8 w_{k+2} + Q_9 w_{k-1} + Q_{10} (w_{k-N-1} + w_{k+N-1}) + Q_{12} (w_{k+N+1} + w_{k-N+1}) + Q_{14} w_{k+1} + (Q_{13} + Q_{M_1})(w_{k-N} + w_{k+N}) + (Q_{11} + Q_{M_2}) w_k + Q_{t_2}(\dot{w}_{k+N} - \dot{w}_{k-N}) + Q_{t_1} \ddot{w}_k = F_k - Q_7 w_L \tag{3.26}$$

Middle nodes, $N+3 \leq k \leq 2N-2$:

$$\begin{aligned}
&Q_7 w_{k+2N} + Q_8(w_{k-2} + w_{k+2}) + Q_{12}(w_{k+N-1} + w_{k+N+1} + w_{k-N-1} + w_{k-N+1}) + \\
&(Q_{15} + Q_{M_2})w_k + (Q_{13} + Q_{M_1})(w_{k-N} + w_{k-N}) + Q_{14}(w_{k-1} + w_{k+1}) + \\
&Q_{t_2}(\dot{w}_{k+N} - \dot{w}_{k-N}) + Q_{t_1}\ddot{w}_k = F_k - Q_7 w_L
\end{aligned} \tag{3.27}$$

$k = 2N-1$:

$$\begin{aligned}
&Q_7 w_{k+2N} + Q_8 w_{k-2} + Q_9 w_{k-1} + Q_{10}(w_{k-N+1} + w_{k+N+1}) + \\
&Q_{12}(w_{k+N-1} + w_{k-N-1}) + Q_{14} w_{k-1} + (Q_{13} + Q_{M_1})(w_{k-N} + w_{k+N}) + \\
&(Q_{11} + Q_{M_2})w_k + Q_{t_2}(\dot{w}_{k+N} - \dot{w}_{k-N}) + Q_{t_1}\ddot{w}_k = F_k - Q_7 w_L
\end{aligned} \tag{3.28}$$

$k = 2N$:

$$\begin{aligned}
&Q_1 w_{k+2N} + Q_2 w_{k-2} + Q_3(w_{k+N-1} + w_{k-N-1}) + (Q_4 + Q_{M_1})(w_{k+N} + w_{k-N}) + \\
&Q_5 w_{k-1} + (Q_6 + Q_{M_2})w_k + Q_{t_2}(\dot{w}_{k+N} - \dot{w}_{k-N}) + Q_{t_1}\ddot{w}_k = F_k - Q_1 w_L
\end{aligned} \tag{3.29}$$

3.2.3 Constants of the Tape Equation

The constants that are used in the above equations are given in this section. They are grouped according to their origins from the governing tape equations.

The Biharmonic Operator:

$$\begin{aligned}
Q_7 &= D[\tfrac{1}{\Delta x^4}] \\
Q_8 &= D[\tfrac{1}{\Delta y^4}] \\
Q_{12} &= D[\tfrac{2}{\Delta x^2 \Delta y^2}] \\
Q_{13} &= D[-4(\tfrac{1}{\Delta x^4} + \tfrac{1}{\Delta x^2 \Delta y^2})] \\
Q_{14} &= D[-4(\tfrac{1}{\Delta y^4} + \tfrac{1}{\Delta x^2 \Delta y^2})] \\
Q_{15} &= D[6(\tfrac{1}{\Delta x^4} + \tfrac{1}{\Delta y^4}) + \tfrac{8}{\Delta x^2 \Delta y^2}]
\end{aligned} \tag{3.30}$$

Nodes at the Free Edges:

$$\begin{aligned} Q_1 &= D[\tfrac{1-\nu^2}{\Delta x^4}] \\ Q_2 &= D[\tfrac{2}{\Delta y^4}] \\ Q_3 &= D[\tfrac{4-2\nu}{\Delta x^2 \Delta y^2}] \\ Q_4 &= D[\tfrac{2\nu}{\Delta y^4} - \tfrac{4(1-\nu^2)}{\Delta x^4} - \tfrac{2(2-\nu)}{\Delta x^2 \Delta y^2}] \\ Q_5 &= D[\tfrac{4\nu-8}{\Delta x^2 \Delta y^2} - \tfrac{4}{\Delta y^4}] \\ Q_6 &= D[\tfrac{2}{\Delta y^4} + \tfrac{8-8\nu}{\Delta x^2 \Delta y^2} + \tfrac{6-6\nu^2}{\Delta x^4}] \end{aligned} \tag{3.31}$$

Nodes Adjacent to Free Edges:

$$\begin{aligned} Q_7 &= \text{Same as above} \\ Q_8 &= \text{Same as above} \\ Q_9 &= D[(\tfrac{2}{\Delta y^4} + \tfrac{2\nu}{\Delta x^2 \Delta y^2}) - \tfrac{4}{\Delta y^4} - \tfrac{4}{\Delta x^2 \Delta y^2}] \\ Q_{10} &= D[\tfrac{2-\nu}{\Delta x^2 \Delta y^2}] \\ Q_{11} &= D[\tfrac{6}{\Delta x^4} + \tfrac{6}{\Delta y^4} + \tfrac{7}{\Delta x^2 \Delta y^2}] \end{aligned} \tag{3.32}$$

Membrane and Shell Terms:

$$\begin{aligned} Q_{M_1} &= \tfrac{\rho_a V_x^2 - T_x}{\Delta x^2} \\ Q_{M_2} &= -2\tfrac{\rho_a V_x^2 - T_x}{\Delta x^2} + K \end{aligned} \tag{3.33}$$

Cross Derivative and Inertial Terms:

$$\begin{aligned} Q_{t_1} &= \rho_a \\ Q_{t_2} &= 2\tfrac{\rho_a V_x}{\Delta x} \end{aligned} \tag{3.34}$$

3.3 Semidiscrete Form of the Equation of Motion of the Tape

The above equations, (3.15-3.29), written for all of the nodes, constitute a set of NEQ equations. This set of equations can be put into the following matrix form.

$$[K]\{w\} + [G]\frac{d}{dt}\{w\} + [M]\frac{d^2}{dt^2}\{w\} = \{F\} + \{f_b\} \tag{3.35}$$

This equation is the *semidiscrete* form of the equation of motion. The matrices and the vectors of Equation (3.35) are,

$[K]$	:	Stiffness matrix
$[G]$	:	Transport matrix
$[M]$	:	Mass matrix
$\{w\}$	:	Displacement vector
$\frac{d}{dt}\{w\}$	:	Displacement velocity vector
$\frac{d^2}{dt^2}\{w\}$	:	Displacement acceleration vector
$\{F\}$	:	External force vector
$\{f_b\}$	:	Boundary condition vector

The stiffness matrix contains terms representing the bending and membrane terms of the tape equation. It is a banded matrix with a total band width of $4N + 1$, and it is composed of the the coefficients of w_k's of Equations (3.15-3.29).

The transport matrix contains the terms that represent the cross derivative term, $\frac{\partial^2}{\partial x \partial t}$. $[G]$ is a banded matrix with a band width $2N + 1$. It is composed of the terms that are multiplied by $\dot{w}_k$ in Equations (3.15-3.29).

The mass matrix represents the inertial acceleration term of the tape's equation of motion. It is a diagonal matrix populated with tape mass. It is composed of the terms that are multiplied by $\ddot{w}_k$ in Equations (3.15-3.29). These three matrices are $NEQ \times NEQ$ square matrices.

The three vectors involving $\{w\}$ and its time derivatives represent the values of these variables at each node of the discretized tape. At this point these vectors are spatially discrete but temporally continuous.

The external force vector, $\{f_b\}$, contains the terms arising from discretizing the simple support boundary conditions. They are given on the right hand sides of equations (3.20-3.29). This vector vanishes when $w_L = w_R = 0$. Also, note that the vector $\{f_b\}$ is time invariant.

3.4 Numerical Solution of the Semidiscrete Equation of Motion

Once the continuous partial differential equation (PDE), (3.1), is reduced to a set of ordinary differential equations, as given by (3.35), a practical way to solve this set of equations is to use numerical time integration. This technique should control the high frequency noise of the response, which is a result of the spatial discretization of the PDE [31]. The analysis of this situation for the equation of motion of the cylindrical shell is given in Chapter 4. The method chosen in this study, the α-method, or otherwise known as Hilber-Hughes-Taylor method, possesses good high frequency dissipation behavior.

In the α-method the semidiscrete system is further discretized in the time domain. The temporally continuous variables $\{w\}, \{\dot{w}\}$, and $\{\ddot{w}\}$ become the following discrete variables $\{w^n\}, \{v^n\}$, and $\{a^n\}$ calculated at time step n, respectively. If the upper time limit on the time integration is τ and the total number of discrete time steps are N_T then the time steps size is $\Delta t = \frac{\tau}{N_T}$. The initial value problem given in Equation (3.35) thus becomes,

$$[K]\{w^{n+1}\} + [G]\{v^{n+1}\} + [M]\{a^{n+1}\} = \{F^{n+1}\} + \{f_b\} \tag{3.36}$$

with the following initial conditions,

$$\{w(0)\} = \{w^o\} \tag{3.37}$$

$$\{v(0)\} = \{v^o\} \tag{3.38}$$

3.4.1 Concepts Related to Discrete Time Integration

The numerical time integration of a semidiscrete system is expected to converge to the analytical solution of the PDE. The convergence is stated for a fixed τ and $\Delta t = \frac{\tau}{N_T}$ as,

$$w^n \rightarrow w(t) \text{ as } \Delta t \rightarrow 0$$

It is shown that the necessary and sufficient conditions for convergence of the numerical integration scheme that we are considering, are *stability* and *consistency* [7]. The stability

of the numerical solution procedure can be defined as its ability to predict a bounded (displacement) response for $t \in [0, \tau]$. A consistent numerical solution has a bounded truncation error $\varepsilon(t)$[1] for $t \in [0, \tau]$.

If the numerical integration scheme uses the variables ($\{w^{n+1}\}$, $\{v^{n+1}\}$, $\{a^{n+1}\}$) of the yet unknown time step $n+1$ to determine them an *implicit* integration is obtained. On the other hand, if the integration scheme uses only the information from the previous time steps the integration scheme is called *explicit*. Implicit schemes are generally unconditionally stable, but they have the disadvantage of requiring matrix "inversions"[2]. If the system parameters such as tension or velocity are time dependent then inversion is required at each time step making the procedure computationally costly. The explicit schemes, on the other hand, do not require any matrix inversion, hence they have faster execution times per time step, but they are only conditionally stable. Stability requires small time steps making the total execution times generally longer.

3.4.2 The α-*method* for Time Integration

The α-method was developed specifically to fulfill the need for a time integration method which can add controlled numerical damping, without sacrificing the accuracy of the time integration, [31]. The Newmark method, which is similar to the α-method, suffers an accuracy drop to $O(\Delta t)$ when its numerical damping is enabled, [34].

In the α-method the semidiscrete equation of motion becomes,

$$(1+\alpha)[K]\{w^{n+1}\} - \alpha[K]\{w^{n}\} + (1+\alpha)[G]\{v^{n+1}\} - \alpha[G]\{v^{n}\} + [M]\{a^{n+1}\} = (1+\alpha)\{F^{n+1}\} - \alpha\{F^{n}\} + \{f_b\} \quad (3.39)$$

where, α is the numerical damping parameter. The displacements and velocities for time step $n+1$ are approximated by,

$$\{w^{n+1}\} = \{\tilde{w}^{n+1}\} + \beta\Delta t^2\{a^{n+1}\} \quad (3.40)$$

[1] The difference between the exact solution of the differential equation and the numerical solution is the truncation error, $\varepsilon(t) = Kw(t) + G\dot{w}(t) + M\ddot{w}(t) - Kw^n - Gv^n - Ma^n$

[2] See Section 3.4.3.

$$\{v^{n+1}\} = \{\tilde{v}^{n+1}\} + \gamma\Delta t\{a^{n+1}\} \tag{3.41}$$

where, β and γ are the parameters controlling the accuracy and stability of the time integration procedure, and $\{\tilde{w}^{n+1}\}$ and $\{\tilde{v}^{n+1}\}$ are the predictors defined as follows,

$$\{\tilde{w}^{n+1}\} = \{w^n\} + \Delta t\{v^n\} + (\frac{1}{2} - \beta)\Delta t^2\{a^n\} \tag{3.42}$$

$$\{\tilde{v}^{n+1}\} = \{v^n\} + (1-\gamma)\Delta t\{a^n\} \tag{3.43}$$

3.4.3 Implicit Integration Algorithm

By substituting Equations (3.40) and (3.41) into (3.39) the acceleration form of an implicit algorithm is obtained.

1. Predict displacement and velocity vectors by $\{\tilde{w}^{n+1}\}$ and $\{\tilde{v}^{n+1}\}$.
   If $n = 0$ then use the initial conditions $\{w^o\}$, and $\{v^o\}$.
2. Obtain the acceleration vector at time n+1, by solving

$$[K]_{eq}\{a^{n+1}\} = \{f^{n+1}\}_{eq} \tag{3.44}$$

3. Calculate $\{w^{n+1}\}$ and $\{v^{n+1}\}$ vectors at time $n+1$ by using Equations (3.42) and (3.43).
4. Increment time by Δt, let $n+1 \rightarrow n$, and go to Step 1.

In the preceding the *equivalent stiffness matrix*, $[K]_{eq}$, and the *equivalent force vector*, $\{f\}_{eq}$, are given by the following expressions,

$$[K]_{eq} = \Big[[M] + (1+\alpha)\gamma\Delta t[G] + (1+\alpha)\beta\Delta t^2[K]\Big] \tag{3.45}$$

$$\{f^{n+1}\}_{eq} = (1+\alpha)\{F^{n+1}\} - \alpha\{F^n\} - (1+\alpha)([G]\{\tilde{v}^{n+1}\} + [K]\{\tilde{w}^{n+1}\}) + \alpha([G]\{v\}^n + [K]\{w\}^n) + \{f_b\} \tag{3.46}$$

If the parameters are chosen in the following range, for this implicit α-method,

$$\alpha \in [-\frac{1}{3}, 0], \quad \gamma = \tfrac{1}{2}(1-2\alpha), \quad \text{and } \beta = \tfrac{1}{4}(1-\alpha)^2 \tag{3.47}$$

an unconditionally stable second-order accurate scheme results. Decreasing α increases the amount of numerical dissipation [7]. The matrix inversion to obtain $\{a^{n+1}\}$ from Equation (3.44), in the true sense of matrix algebra, is a costly operation. For this reason LU decomposition is used to factor the equivalent stiffness matrix, $[K]_{eq}$. The solution is then obtained by multiplying this factorized matrix with the equivalent force vector, $\{f^{n+1}\}_{eq}$, for each time step provided that $[K]_{eq}$ is time invariant. We use the implicit time integration in Chapter 5 where we study the shell's response to a point load.

Note that for $\alpha = 0$, the α-method reduces to Newmark's family of methods [7]. For completeness we are giving the limits for parameters α and β for unconditional stability for the Newmark method,

$$\gamma \geq \tfrac{1}{2}, \quad \beta \geq \frac{(\gamma + \frac{1}{2})^2}{4} \tag{3.48}$$

Selecting $\gamma = 1/2$ and $\beta = 1/4$ gives a second order accurate system without any numerical damping. Choosing the parameters in the range given by Equations (3.48) filters out high frequencies, however, if $\gamma \neq 1/2$ the order of accuracy of the solution drops to $O(\Delta t)$.

3.4.4 Explicit Integration Algorithm

The high volume of matrix multiplications necessary for an implicit algorithm becomes burdensome for the foil bearing problem especially when some of the problem parameters such as tape tension, T_x, and speed, V_x are time dependent[3]. Therefore, to speed up the calculations in the solution of the foil bearing problem we use an explicit method. In order to obtain the explicit algorithm the following replacement is made in Equation (3.39) [34],

$$\{w^{n+1}\} \rightarrow \{\tilde{w}^{n+1}\} \tag{3.49}$$

$$\{v^{n+1}\} \rightarrow \{\tilde{v}^{n+1}\} \tag{3.50}$$

[3]Tape tension and speed are represented in the equivalent stiffness matrix, $[K]_{eq}$. When they are time dependent, for an implicit method this matrix needs to be factorized with the LU decomposition at each time step.

As the predictors, $\{\tilde{w}^{n+1}\}, \{\tilde{v}^{n+1}\}$, consist of terms which belong to the known time step n they can be transformed to the right hand side of Equation (3.39). Thus, the only unknown for time step $n+1$ becomes $\{a^{n+1}\}$ which can be obtained by a simple division operation, since $[M]$ is a diagonal matrix. The explicit time integration algorithm is as follows:

1. Predict displacements and velocities using $\{\tilde{w}^{n+1}\}$ and $\{\tilde{v}^{n+1}\}$.
   If $n = 0$ use the initial conditions, $\{w^o\}$, and $\{v^o\}$.
2. Solve for accelerations at time step $n+1$ using,

$$\{a^{n+1}\} = [M]^{-1}[(1+\alpha)\{F^{n+1}\} - \alpha\{F^n\} - (1+\alpha)([G]\{\tilde{v}^{n+1}\} + [K]\{\tilde{w}^{n+1}\}) \\ +\alpha([G]\{v^n\} + [K]\{w^n\})] \quad (3.51)$$

3. Calculate $\{w^{n+1}\}$ and $\{v^{n+1}\}$ using equations (3.40) and (3.41).
4. Increment time by Δt, let $n+1 \rightarrow n$, and go to Step 1.

Analysis of the stability of the α-method with the above explicit algorithm is not known to us at this point[4]. However, the stability analysis of the explicit algorithm defined by Equations (3.40-3.43) and (3.51), for Newmark's method, ($\alpha = 0$,) is given by Hughes, [34, pp. 559-561]. There are no unconditionally stable explicit algorithms available in the Newmark family. The stability conditions of the explicit algorithm, with $\alpha = 0$, are as follows:

$$\gamma \geq \frac{1}{2} \quad (3.52)$$

$$\omega\Delta t \leq \Omega_{crit} \equiv (\frac{2}{\gamma})^{1/2} \quad (3.53)$$

Stability is independent of the choice of β which is chosen as,

$$\beta = \frac{(\gamma + \frac{1}{2})^{1/2}}{4} \quad (3.54)$$

[4]We were able to obtain results with $\alpha = -0.05$ and corresponding β and γ using Equation (3.47). Smaller α values resulted in catastrophic runs.

As the PDE representing the equation of motion of the tape, (3.1), is a highly dispersive one, the critical frequency of the tape equation does not attain a single value[5]. Therefore, we determined the critical value for the time step size, Δt, for the coupled problem by using an implicit tape equation solver in the coupled algorithm[6]. The critical time step, Δt, was found to be $0.15\mu s$ for the coupled problem with the implicit tape integration algorithm. Time steps larger than this value caused unsuccessful runs.

3.5 Numerical Solution of the Reynolds Equation

Solving the transient form of the Reynolds equation is an effective method for determining the steady state solution of a bearing as well as obtaining a time dependent response.

Castelli and Pirvics [15], summarize methods used until 1968 for the solution of the transient Reynolds equation. Possible solution methods deal with the time derivative in "explicit", "implicit" and "semi-implicit"[7] manner. Moreover, they point out that alternating direction schemes, in which the derivatives in different spatial directions are dealt with separately, mixed with the latter two temporal differentiation schemes, decrease the solution effort. Methods that they discuss are $O(\Delta t)$ accurate.

Coleman [16] pointed out that phase shifts that are inherent in a numerical time integration can cause the failure of the first order accurate implicit schemes, unless very small time steps are used. In his case, phase shifts were characterized by the amplitude error in the numerical temporal integration. In general period errors can also contribute to the overall error [34]. Coleman demonstrated that employing a second order accurate time differentiation scheme improves the handling of these errors.

White and Nigam, [68] used the alternating direction implicit (ADI) method with second order accurate, $O(\Delta t^2)$, time differentiation to solve the two dimensional Reynolds equation. Easy implementation of this method has enabled other investigators to use it

[5] Refer to Chapter 4 for further discussion on this.
[6] See Section 3.6.
[7] Implicit in one spatial direction only.

in transient elastohydrodynamic problems, as well as slider bearing problems, [46, 55]. This method is adopted here for the transient solution of the Reynolds equation.

The ADI method applied to the Reynolds equation reduces to the solution of the following set of linear equations. Interested reader may find the details of this linearization in [46] or [68].

$$[1 - \mathrm{L}_x(\quad)][1 - \mathrm{L}_y(\quad)]\Delta\{z\} = \{R\} \tag{3.55}$$

The variables of this equation are as follows,

$$\{z\} = \{p\}\{h\} \tag{3.56}$$

$$\Delta\{z\} = \{z^{n+1}\} - \{z^n\} \tag{3.57}$$

where, $\{p\}$ is the vector containing air pressure values and $\{h\}$ is the vector containing the bearing height values at nodal points. The difference operators $\mathrm{L}_x(\quad)$ and $\mathrm{L}_y(\quad)$ are given as follows,

$$\begin{aligned}
\mathrm{L}_x(\quad) \;=\; & a[(2hz_{,x} - zh_{,x} - 6\mu V_x)\frac{x_k - x_{k-N}}{D2X0} + (z + 6\lambda_a P_a h\frac{2}{D2X0}]^n(\quad)_{k-N} \\
& a[(2hz_{,x} - zh_{,x} - 6\mu V_x)\frac{2x_k - x_{k-N} - x_{k+N}}{D2X1} + hz_{,xx} - h_{,x}z_{,x} - \\
& (2z + 6\lambda_a P_a)h_{,xx} + (z + 6\lambda_a P_a h\frac{-2}{D2X1}]^n(\quad)_k \\
& a[(2hz_{,x} - zh_{,x} - 6\mu V_x)\frac{x_{k+N} - x_k}{D2X2} + (z + 6\lambda_a P_a)h\frac{2}{D2X2}]^n(\quad)_{k+N}
\end{aligned} \tag{3.58}$$

$$\begin{aligned}
\mathrm{L}_y(\quad) \;=\; & a[(2hz_{,y} - zh_{,y} - 6\mu V_y)\frac{y_k - y_{k-1}}{D2Y0} + (z + 6\lambda_a P_a h\frac{2}{D2Y0}]^n(\quad)_{k-1} \\
& a[(2hz_{,y} - zh_{,y} - 6\mu V_y)\frac{2y_k - y_{k-1} - y_{k+1}}{D2Y1} + hz_{,yy} - h_{,y}z_{,y} - \\
& (2z + 6\lambda_a P_a)h_{,yy} + (z + 6\lambda_a P_a h\frac{-2}{D2Y1}]^n(\quad)_k \\
& a[(2hz_{,y} - zh_{,y} - 6\mu V_y)\frac{y_{k+1} - y_k}{D2Y2} + (z + 6\lambda_a P_a)h\frac{2}{D2Y2}]^n(\quad)_{k+1}
\end{aligned} \tag{3.59}$$

Note that the difference operators, given in Equations (3.58) and (3.59), contain terms all of which are calculated at time step n. On the other hand, the right hand side vector, $\{R\}$, contains h_k^{n+1}, which is at time step $n+1$. For this reason the value of h_k^{n+1} needs

to be known before $\{R\}$ can be calculated. In this study this value is obtained by solving the tape equation before the Reynolds equation. See the coupling algorithm given in Section 3.6.

$$\begin{aligned} R = (z^n + 6\lambda_a P_a)(h^{n+1} + \frac{1-\gamma}{\gamma}h^n)[(z^n_{,xx} + z^n_{,yy}) + (z^n_{,x} + z^n_{,y})] - \\ z^n(z^n + 6\lambda_a P_a)[(h^{n+1}_{,xx} + h^{n+1}_{,yy}) + \frac{1-\gamma}{\gamma}(h^n_{,xx} + h^n_{,yy})] - \\ z^n[z^n_{,x}(h^{n+1}_{,x} + \frac{1-\gamma}{\gamma}h^n_{,x}) + z^n_{,y}(h^{n+1}_{,y} + \frac{1-\gamma}{\gamma}h^{n+1}_{,y})] - \\ 2\mu(V_x z^n_{,x} + V_y z^n_{,y}) \end{aligned} \tag{3.60}$$

In these equations,

$$a = \frac{\gamma \Delta t}{12\mu} \tag{3.61}$$

where, γ is an integration parameter. For second order accuracy it is taken as $1/2$ [46]. The constants $D2X0, D2X1, D2X2, D2Y0, D2Y1$, and $D2Y2$ are finite difference denominator expressions derived for non-uniformly spaced finite difference grid points,

$$\begin{aligned} D2X0 &= (x_k - x_{k-N})(x_{k+1} - x_{k-1}) \\ D2X1 &= (x_k - x_{k-N})(x_k - x_{k+N}) \\ D2X2 &= (x_{k+N} - x_k)(x_{k+N} - x_{k-N}) \\ D2Y0 &= (x_k - x_{k-1})(x_{k+1} - x_{k-1}) \\ D2Y1 &= (x_k - x_{k-1})(x_k - x_{k+1}) \\ D2Y2 &= (x_{k+1} - x_k)(x_{k+1} - x_{k-1}) \end{aligned} \tag{3.62}$$

Equation (3.55) is cast in such a way that it can be solved in x and y-directions in separate sweeps. This is done by defining,

$$\{\phi\} = [1 - \mathrm{L}_y(\quad)]\Delta\{z\} \tag{3.63}$$

Then Equation (3.55) can be reduced to solving,

$$[1 - \mathrm{L}_x(\quad)]\{\phi\} = \{R\} \tag{3.64}$$

Moreover, the solution of this equation is further simplified by the way Equation (3.58) is given. When (3.58) is investigated closely we see that it consists of operations in the

row-wise (j =constant) manner. These operations actually reduce to solutions of a set of tri-diagonal matrices. Therefore, the operation defined by Equation (3.64) turns out to be N solutions of $M \times M$ tri-diagonal matrices. Completion of this first part of the procedure gives the vector $\{\phi\}$. Then (3.63) is used to determine Δz. The solution of this equation is similar to the x-direction "sweep". The only difference is that in the y-direction operation the $N \times N$ tri-diagonal matrices are solved M times using Equation (3.59). A system of equations, given in the tri-diagonal matrix form can be solved by a special LU decomposition algorithm which takes advantage of the positions of the components of the matrix. Therefore, the solution of Equation (3.55) is an efficient integration scheme.

3.6 Coupled Solution of the Governing Equations

The equation of motion of the tape, (3.1), and the Reynolds Equation (2.58) are solved separately, and coupled through the tape guide spacing equation, (2.60). Due to strongly nonlinear dependency of the air pressure, p, on tape guide spacing, h, it is necessary to repeatedly solve all of the three equations, within a given time step, until these two variables converge, at all of the nodes in the solution domain. The convergence tolerance is indicated by ϵ_p and ϵ_w for air pressure and radial tape displacement. See the algorithm given below for the definition of ϵ_p and ϵ_w. We used a convergence tolerance of 0.1% for both variables.

The algorithm which couples the explicit solution of the tape equation with the ADI solution of the Reynolds equation is given below. A similar algorithm for the implicit solution of the tape equation can be obtained easily by using the information given in Section 3.4.3[8].

[8]Heinrich and Connelly, used a similar implicit algorithm, [29].

0. Initial Conditions

$$w^0 = \bar{w}, \qquad p^0 = \bar{p}, \qquad v^0 = \bar{v}, \qquad n = 0, \qquad a^0 = 0, \qquad t = \Delta t.$$

1. Predictors:

$$\begin{aligned} \tilde{w}^{n+1} &= w^n + v^n \Delta t + (\tfrac{1}{2} - \beta)\Delta t^2 a^n, & \tilde{p}^{n+1^{(i)}} &= p^n, \\ \tilde{v}^{n+1} &= v^n + (1-\gamma)\Delta t a^n, & h^n &= w^n + \delta \\ \tilde{a}^{n+1} &= 0, & i &= 0 \end{aligned}$$

2. Start Iterations:

$$\begin{aligned} w^{n+1^{(i+1)}} &= \tilde{w}^{n+1}, & p^{n+1^{(i+1)}} &= \tilde{p}^{n+1^{(i)}}, \\ v^{n+1^{(i+1)}} &= \tilde{v}^{n+1}, & h^{n+1^{(i+1)}} &= h^n \\ a^{n+1^{(i+1)}} &= \tilde{a}^{n+1}, & z^n &= h^n p^n \end{aligned}$$

3. Calculate P_c, f_{eq}, a^{n+1}:

$$\text{IF } h_k^{n+1^{(i+1)}} \leq \sigma_t \text{ THEN } P_{c_k}^{(i+1)} = \tfrac{\sqrt{P_m}}{\sigma_t}(\sigma_t - h_k^{n+1^{(i+1)}}))^2$$

$$\begin{aligned} F^{n+1^{(i+1)}} &= p^{n+1^{(i+1)}} - Pa - P_{BW} + P_c^{(i+1)} + f_b \\ f_{eq} &= \Big[(1+\alpha)F^{n+1^{(i+1))}} - \alpha F^n - (1+\alpha)(G\tilde{v}^{n+1} + K\tilde{w}^{n+1}) + \\ &\quad \alpha(Gv^{n^{(i+1)}} + Kw^{n^{(i+1)}})\Big] \\ a^{n+1^{(i)}} &= \frac{f_{eq}}{\rho_a} \end{aligned}$$

4. Correctors:

$$\begin{aligned} w^{n+1^{(i+1)}} &= \tilde{w}^{n+1} + \beta \Delta t^2 a^{n+1^{(i+1)}} \\ v^{n+1^{(i+1)}} &= \tilde{v}^{n+1} + \gamma \Delta t a^{n+1^{(i+1)}} \\ h^{n+1^{(i+1)}} &= w^{n+1^{(i+1)}} + \delta \end{aligned}$$

5. Solve for p^{n+1}

$$[1 - L_x(\quad)][1 - L_y(\quad)]\Delta z^{n+1} = \phi^{n+1}$$

$$z^{n+1^{(i+1)}} = z^n + \Delta z^{n+1} \tag{3.65}$$

$$p^{n+1^{(i+1)}} = z^{n+1^{(i+1)}} / h^{n+1^{(i+1)}} \tag{3.66}$$

6. Check for Convergence:

$$\left| \frac{p^{n+1^{(i+1)}} - p^{n+1^{(i)}}}{p^{n+1^{(i)}}} \right| < \epsilon_p \quad \text{and} \quad \left| \frac{w^{n+1^{(i+1)}} - w^{n+1^{(i)}}}{w^{n+1^{(i)}}} \right| < \epsilon_w$$

IF (NO) THEN

$p^{n+1^{(i)}} = p^{n+1^{(i+1)}}, \qquad i = i + 1$

GO TO 3

IF (YES) THEN

$p^n = p^{n+1^{(i+1)}}, \qquad v^n = v^{n+1^{(i+1)}},$

$h^n = h^{n+1^{(i+1)}}, \qquad w^n = w^{n+1^{(i+1)}},$

$a^n = a^{n+1^{(i+1)}}, \qquad n = n + 1,$

$t = t + \Delta t,$

IF $t < \tau$ THEN GO TO 1

7. Stop

Chapter 4

Frequency Analysis of the Semidiscrete System

4.1 Introduction

In this chapter we establish the validity bounds of the spatial finite difference scheme that is used to solve the equation of motion of a circumferentially moving cylindrical shell. This is done by comparing the dispersion relations and the wave speeds of the spatially continuous and discrete systems. We first obtain the dispersion relation for the governing partial differential equation (PDE)[1], (2.34). Then the dispersion relation for the spatially discretized form of this equation is derived. Finally, the two equations are compared as the node spacing, Δ, is varied.

The results show that considerable error due to spatial discretization can be introduced into the solution by a careless choice of spatial step size. The sensitivity is greater at smaller wavelengths. The amount of error can be identified by the help of the phase and group velocity error diagrams, such as Figures 4-13 and 4-11. For a given node spacing the error is greater for the wavelength values near Δ, but it is much less than 10% for wavelengths greater than 10Δ.

[1]Equation of motion of the circumferentially moving cylindrical tape.

4.1.1 Background on Dispersion

The study of this subject requires defining the following concepts related to wave propagation in general. These definitions are taken from Brillouin, [12]. The definitions of the *group velocity*, V_g, and the *phase velocity*, V_p, are important ones. The latter represents the motion of elementary wavelets in a wave action, while the group velocity represents the propagation of the modulation imposed on these individual wavelets.

This can be demonstrated by a simple example given in the book by Brillouin. If we assume that a *carrier signal* has frequency ω_o and *modulation* $C(x,t)$, it can be shown that this signal, $w(x,t)$, can be represented as follows:

$$w(x,t) = C(t - \frac{x}{V_g}) \cos \omega_o (t - \frac{x}{V_p}) \tag{4.1}$$

In this equation the modulation, C, moves with V_g and the carrier, $\cos \omega_o (t - \frac{x}{V_p})$, moves with speed, V_p. In this example, V_g is a constant, but V_p is a function of the wavelength. In more complicated systems the group velocity also becomes a function of the wavelength. Thus we arrive at a definition for *dispersive* systems as systems which exihibit wavelength dependent group and phase velocities. In a dispersive medium the following definitions hold,

$$\begin{aligned} &\text{if } V_g > V_p \quad \text{the system is said to have anomalous dispersion} \\ &\text{if } V_p > V_g \quad \text{the system is said to have normal dispersion.} \end{aligned}$$

In a system that has anomalous dispersion, wavelets build up in front of the group and disappear in the rear end of the group. Whereas in a normally dispersive system the wavelets build up at the back end of the group, progress through the group and disappear in front of the group.

The information about the group and wave velocities is obtained by studying the *dispersion curve* of the system. This curve defines the relation between the time frequency, ν, and the wavelength, λ. Along the lines of common practice, in what follows the *wave*

number, k^2,

$$k = \frac{2\pi}{\lambda} \tag{4.2}$$

is used instead of λ, and the frequency is exchanged with ω,

$$\omega = 2\pi\nu \tag{4.3}$$

and for simplicity ω is called the frequency. The dispersion curve for a wave equation can be obtained by assuming the following form for the signal, (displacement in our case)

$$w(x, y, t) = e^{i(\vec{k}.\vec{u}-\omega t)} \tag{4.4}$$

In this equation, $\vec{k}$ is the wave number vector, $\vec{u}$ is the location vector. These two vectors are defined as follows:

$$\vec{k} = p\vec{\subset} + q\vec{\supset} \tag{4.5}$$

and

$$\vec{u} = x\vec{\subset} + y\vec{\supset} \tag{4.6}$$

where, p and q are the coordinate wave numbers, and $\vec{\subset}$ and $\vec{\supset}$ are the unit vectors in the x and y directions, respectively. The magnitude and the direction of the wave number vector are

$$k = (p^2 + q^2)^{1/2} \tag{4.7}$$

and

$$\theta = \arctan\frac{p}{q} \tag{4.8}$$

respectively[3]. An equivalent form of Equation (4.4) is as follows:

$$w(x, y, t) = e^{i(px+qy-\omega t)} \tag{4.9}$$

The dispersion relation gives the dependence of the the frequency, ω, on the wave number, k[4]. For a given system the dispersion relation is obtained by substituting Equation (4.9)

[2]Note that k used in this chapter, is different than the node numbering counter used in Chapter 3.
[3]Note that θ is different from the wrap angle used in the rest of the thesis.
[4]If the frequency is independent of the wave number the system is non-dispersive.

into the wave equation representing the system. The phase velocity of the system is defined by,

$$V_p = \frac{\omega}{k} \tag{4.10}$$

and the group velocity is,

$$V_g = \frac{d\omega}{dk} \tag{4.11}$$

4.1.2 Analyzing the Effects Numerical Solutions

Any form of numerical solution to the governing wave equation requires a spatial discretization of the system. In this section, we present the necessary tools to analyze the effects of the spatial discretization with finite difference equations, on the frequency ω. The approach that we employ follows Birkhoff and Dougalis, [9], and Vichnevetsky and Bowles [66].

This approach uses similar tools to the ones used for obtaining the dispersion curve for a wave equation defined by a (spatially continuous) PDE. A function of the form,

$$w_{m,n}(t) = e^{i(px_m + qy_n - \omega_\Delta t)} \tag{4.12}$$

is substituted into the discretized form of the wave equation. In this equation the nodal locations on the discretized domain are given by (m, n) pairs. The spatial step sizes in the x and y directions are equal, and they are denoted by $\Delta = \Delta x = \Delta y$. The symbol ω_Δ indicates that the frequency is due to spatial discretization. The goal of the analysis is to achieve,

$$\omega_\Delta \to \omega \quad \text{as } \Delta \to 0 \tag{4.13}$$

As noted in Birkhoff and Dougalis, the analysis can be applied to finite difference as well as finite element discretizations [9]. We consider the finite difference case in Section 4.3.

4.2 The Dispersion Relation

In this section the dispersion relation for the equation of motion of a cylindrical thin shell is derived. The governing equation, (3.1), is repeated below,

$$D[\frac{\partial^4 w}{\partial x^4} + 2\frac{\partial^4 w}{\partial x^2 \partial y^2} + \frac{\partial^4 w}{\partial y^4}] + Kw + (\rho_a V_x^2 - T_x)\frac{\partial^2 w}{\partial x^2} + 2\rho_a V_x \frac{\partial^2 w}{\partial x \partial t} + \rho_a \frac{\partial^2 w}{\partial t^2} = 0 \quad (4.14)$$

In this equation D is the bending stiffness, K is the shell stiffness, ρ_a is the areal density, V_x is the tape transport speed, T_x is the circumferential tape tension, w is the radial tape displacement, x is the circumferential coordinate, y is the axial coordinate, and t is time. Table (2.1) gives the definitions of D and K. Note that as we are interested only in the spatial and temporal modes of the equation we omit the forcing term. In what follows in this chapter we assume that the guide pins (See Figure 2-1) are placed close to the surface of the cylinder, so that the tape is completely cylindrical. We also neglect the effect of the boundary conditions on the initial wave propagation.

The following dispersion relation is obtained by substituting Equation (4.9) into Equation (4.14), and using definitions given in Equations (4.7) and (4.8),

$$\omega = V_x k \cos\theta \pm \frac{1}{\sqrt{\rho}}\sqrt{Dk^4 + T_x k^2 \cos^2\theta + K} \quad (4.15)$$

By examining Equation (4.15), we see that the frequency ω is a function of the wave number, k. Therefore, we conclude that the system is dispersive. Furthermore, we note that dispersion is orientation, θ, dependent (anisotropic dispersion). The "+/-" signs correspond to waves moving in $-\vec{u}$ and $+\vec{u}$ directions, respectively. Due to front-to-back symmetry that exists in the tape, it is sufficient to consider θ's in the $-\pi/2 \leq \theta \leq \pi/2$ range.

For small wave numbers Equation (4.15) reduces to,

$$\omega = \sqrt{\tfrac{K}{\rho}} \quad \text{as } k \to 0, \text{ or equivalently as } \lambda \to \infty \quad (4.16)$$

This indicates that the shell stiffness, K, dominates frequencies of the large wavelengths. On the other hand we see that as $k \to \infty$ (or equivalently, $\lambda \to 0$) in Equation (4.15),

the bending and tension effects, represented by D and T_x terms, start to dominate the frequencies. This result should be expected because the bending terms would be more dominant where the derivatives of the displacements are higher due to short wavelengths. On the other hand displacements vary slowly on the long wavelengths thus making the bending stiffness term more dominant.

Typical parameters for a helical-scan application are given in Table 4.1[5]. All of the figures in this chapter use these values. Figure 4-1 displays Equation (4.15) for tape transport speed of $25m/s$. The effect of anisotropy in three θ directions can be seen in this figure.

The phase velocity is obtained by using Equation (4.10),

$$V_p = \frac{\omega}{k} = V_x \cos\theta \pm \frac{1}{\sqrt{\rho}}\sqrt{Dk^2 + T_x \cos^2\theta + \frac{K}{k^2}} \tag{4.17}$$

The interpretation of the "+/-" signs is similar to before. From Equation (4.2) it can be seen that the phase velocity has a minimum at,

$$k^* = (\tfrac{K}{D})^{1/4} \quad \text{or} \quad \lambda^* = 2\pi(\tfrac{D}{K})^{1/4} \tag{4.18}$$

This minimum point indicates that the phase velocity, V_p, of the wave propagation is dominated by,

Shell stiffness effects for $k < (\frac{K}{D})^{1/4}$ or $\lambda^* > 2\pi(\frac{D}{K})^{1/4}$, and

Bending effects for $k > (\frac{K}{D})^{1/4}$ or $\lambda^* < 2\pi(\frac{D}{K})^{1/4}$.

The x and y components of the group velocity are calculated by using Equation (4.11). To do this, k is replaced with p and q for x and y directions, respectively.

$$V_{g_x} = \frac{d\omega}{dp} = V_x \pm \frac{2D(p^3 + pq^2) + T_x p}{\sqrt{\rho(D(p^2+q^2)^2 + T_x p^2 + K)}} \tag{4.19}$$

$$V_{g_y} = \frac{d\omega}{dq} = \pm\frac{2D(p^2 q + q^3)}{\sqrt{\rho(D(p^2+q^2)^2 + T_x p^2 + K)}} \tag{4.20}$$

[5]These parameters are taken from Müftü and Benson [49].

These equations are plotted in Figures 4-2 - 4-4 with wavelength, λ, as the independent variable. The wavelength is obtained from Equation (4.2) by using k for the phase velocity, and p and q for the group velocities in the x and y directions, respectively. These figures show that, for the parameters considered here, at the short wavelength region the cylindrical tape shows anomalous dispersion, and at the long wavelength region it shows normal dispersion. The phase velocity, V_p, and the group velocity in the y-direction, V_{g_y}, switch magnitudes at,

$$k = \sqrt{\frac{T_x}{2D}\cos^2\theta + \sqrt{(\frac{T_x}{2D}\cos^2\theta)^2 + \frac{K}{D}}} \tag{4.21}$$

This value of k is only slightly higher than k^* that we found previously in Equation (4.18) for the tension value, $T_x = 90N/m$, considered. Therefore, after seeing that $K/D >> T_x/D$, we can say that the phase velocity, V_p, and the group velocity in the y-direction, V_{g_y} intersect at k^*. The physical significance of this, if there is any, is not obvious to us.

We also observe for larger wavelengths the group velocity in y-direction asymptotes to zero, whereas the phase velocity linearly increases with λ. For wavelengths approaching zero we notice that both of the velocities asymptote to infinity. This unphysical result is attributed to omitting higher order terms and coupling with the in-plane components of the displacements and stress resultants in deriving the governing equation.

4.3 Dispersion Relation for the Discretized Equation

The semidiscrete form of Equation (4.14) is obtained as described in Chapter 3. In order to keep the notation clearer the location of a node point on the discretized tape is indicated by the (m, n) pair, rather than the node number k used in Chapter 3. The

discretized form of the equation of motion then becomes,

$$\begin{aligned}&\tfrac{D}{\rho\Delta^4}\,[w_{m-2,n}+w_{m,n-2}+w_{m+2,n}+w_{m,n+2}+2(w_{m-1,n-1}+w_{m-1,n+1}+\\&w_{m+1,n-1}+w_{m+1,n+1})-8(w_{m-1,n}+w_{m+1,n}+w_{m,n-1}+w_{m,n+1})+\\&20w_{m,n}]+\tfrac{V_x^2-T_x/\rho}{\Delta^2}(w_{m-1,n}-2w_{m,n}+w_{m+1,n})+\tfrac{K}{\rho}w_{m,n}+\\&\tfrac{V_x}{\Delta}\tfrac{\partial}{\partial t}(w_{m+1,n}-w_{m-1,n})=-\tfrac{\partial^2 w_{m,n}}{\partial t^2}\end{aligned}\tag{4.22}$$

The dispersion relation for this equation is obtained by substituting Equation (4.12) into the above equation. After the necessary substitutions and some work the following dispersion relation is obtained,

$$\omega_\Delta = V_x\frac{\sin p\Delta}{\Delta}\pm\Omega \tag{4.23}$$

where, Ω is,

$$\begin{aligned}\Omega=\{V_x^2(\frac{\sin p\Delta}{\Delta})^2+\frac{2D}{\rho\Delta^4}[&\cos 2p\Delta+\cos 2q\Delta+4\cos p\Delta\cos q\Delta-\\&8(\cos p\Delta+\cos q\Delta)+10]+2\frac{V_x^2-T_x/\rho}{\Delta^2}(\cos p\Delta-1)+\frac{K}{\rho}\}^{1/2}\end{aligned}\tag{4.24}$$

The "+/-" signs are interpreted as before. By inspection of Equation (4.23) we can see that it also is dispersive and anisotropic. The phase velocity corresponding to this case is given by,

$$V_{p_\Delta}=\frac{\omega_\Delta}{k} \tag{4.25}$$

and the group velocities in the x and y directions are calculated as before,

$$\begin{aligned}V_{g_x}^\Delta=\frac{\partial\omega}{\partial p}=V_x\cos p\Delta\pm\frac{1}{\Omega}[&\frac{\sin p\Delta}{\Delta}(V_x^2(\cos p\Delta-1)+\frac{T_x}{\rho})+\\&\frac{D}{\rho\Delta^3}(8\sin p\Delta-4\sin p\Delta\cos q\Delta-2\sin 2p\Delta)]\end{aligned}\tag{4.26}$$

$$V_{g_y}^\Delta=\frac{\partial\omega}{\partial q}=\pm\frac{D}{\rho\Omega\Delta^3}(8\sin q\Delta-4\sin q\Delta\cos p\Delta-2\sin 2q\Delta) \tag{4.27}$$

4.4 Comparison of Wave Action on the Continuous and Discretized Tape

The phase and group velocity equations obtained for the semidiscrete form of the equation of motion are compared with their counterparts for the continuous solution in Figures 4-5 to 4-7. From these figures we observe that when a coarse finite difference mesh is used, the curves for the analytical relations and the semidiscrete relations grow apart. This difference is more severe near the smaller wavelengths (or higher wave numbers). This result shows that;

> *For the finite difference discretization of the equation of motion of the cylindrical shell, the small wavelengths are artifacts of the spatial discretization.*

This conclusion agrees well with a similar statement given by Hughes for the finite element method [34]. Moreover, the same figures also show that, as the size of Δ is made smaller the discrepancy between continuous and discrete cases become smaller. This is seen better with the aid of the following error criteria,

$$\varepsilon_p = \left|\frac{V_p - V_{p_\Delta}}{V_p}\right| \times 100\% \qquad\qquad \varepsilon_g = \left|\frac{V_g - V_{g_\Delta}}{V_g}\right| \times 100\% \tag{4.28}$$

where, ε_p is the phase velocity error, and the ε_g is the group velocity error expressed in percent.

The errors involved in predicting the phase and group velocities using a finite difference scheme as a function of wavelength λ are given in Figures 4-8 - 4-10. These figures show that for a given nodal spacing, discretized equation has high errors for wavelengths close to $\lambda = \Delta$. The error is lower for longer wavelengths. For example, the error for predicting the velocities of a wave with a wavelength of $\lambda = 1mm$, by choosing $\Delta = 0.1mm$ ($\frac{\lambda}{\Delta} = 10$) is 2.5% for V_p and 8% for V_{g_x} and reduces considerably at the longer wavelengths. See Figures 4-8 - 4-9.

Figures 4-11 and 4-12 show the effect of the tape transport speed, V_x, on the phase velocity error, ε_p, and the group velocity error in y direction, ε_{gy}. Again we observe that the error is high on the short wavelengths. These figures demonstrate that faster tape transport speeds cause slightly greater errors, but the the difference is insignificant.

Figure 4-13 shows the error in the phase and group velocities as a function of $\frac{\lambda}{\Delta}$[6]. The tape velocity in this figure is $V_x = 25m/s$ and the wave orientation is $\theta = \pi/4$. In principle the lowest value of wavelength that can be predicted in a finite difference scheme is $\lambda = 2\Delta$. However, our analysis shows that for the discretization and the parameters considered here, the error involved in predicting the velocities of waves with wavelengths close to λ is considerably high. From Figure 4-13 we can see that the highest error involved in predicting the velocities is near 12% for the wavelengths, $\lambda \simeq 10\Delta$.

We also observed that the error introduced to the solution is anisotropic. For the waves that have orientations close to $\theta = 0$, and $\pi/4$, the error curves for V_{g_x} and V_{g_y} are coincident, but as the wave orientation is away from these limits the error in V_{g_x} becomes higher.

Based on the observations made above we conclude that the high frequencies corresponding to short wavelengths should be removed from the numerical solution using numerical damping. The effect of the numerical damping on a previously published work, [49, 50], is presented in the next chapter.

4.5 Summary and Conclusions

In this chapter we showed that the wave propagation in a circumferentially moving thin cylindrical shell is anisotropically dispersive. Upon analyzing the phase speed as a function of the wavelength we determined that the long waves encountered in this medium are dominated by the shell stiffness term, K, and the short waves are dominated by a combination of the bending rigidity, tension and transport speed.

[6] In calculation of $\frac{\lambda}{\Delta}$ the wavelength belonging to each velocity definition was used. For example for calculating this non-dimensional ratio for V_{g_x}, the corresponding wavelength, λ_{g_x} was used.

ρ_a	Areal density	$1400 \times c\ kg/m^2$
V_x	Tape transport speed	variable
T_x	Circumferential tension	$90, N/m$
E	Young's modulus	$4\ GPa$
ν	Poisson's ratio	0.3
c	Tape thickness	$20\ \mu m$
R	Drum radius	$2\ cm$

Table 4.1: Typical parameters for a helical-scan application.

We also analyzed the effect of spatial discretization on the predicted wave speeds in our numerical solution method. We determined that inadequate spatial step size affects the short wave velocities. We showed that in order to prevent the occurence of incorrect wave speeds a safe rule is to use a step size that is 1/10th of the shortest wavelength of interest.

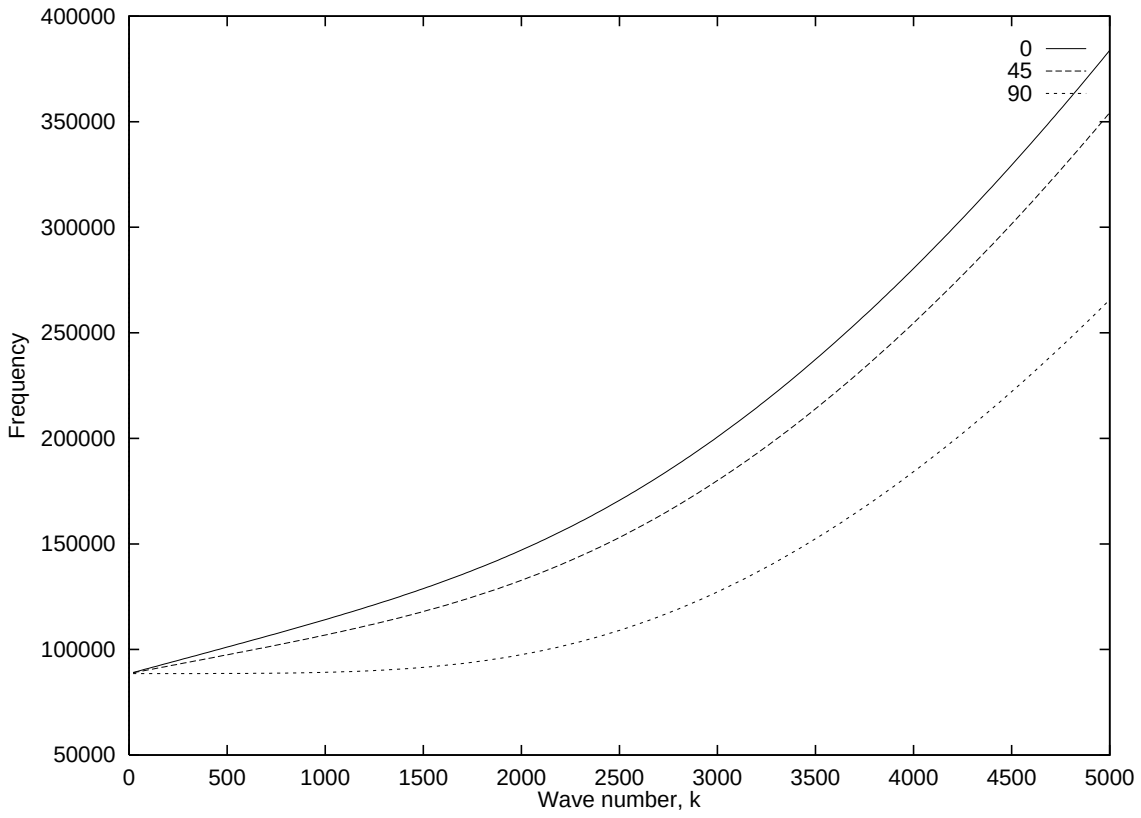

Figure 4-1: Analytical dispersion curve for $V_x = 25m/s$, at different orientations, $\theta = 0, \pi/4, \pi/2$.

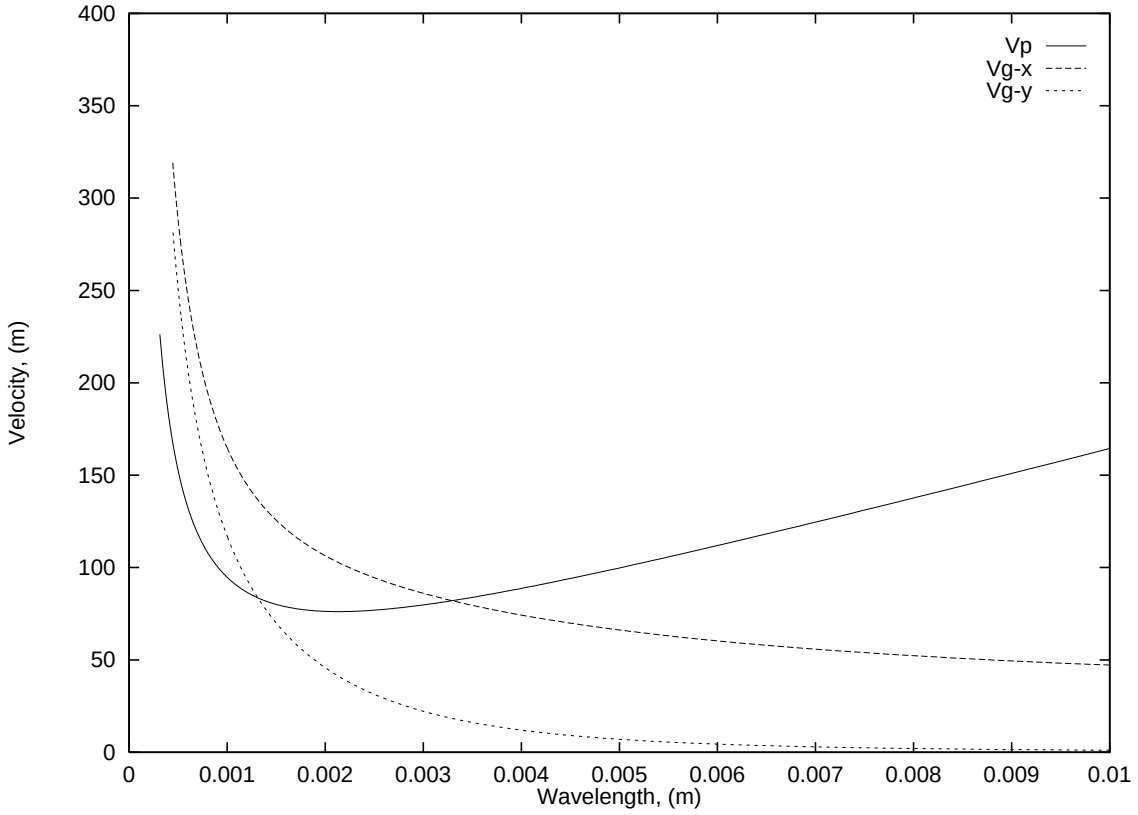

Figure 4-2: Phase and Group Velocities for $V_x = 25, \theta = \pi/4$. The wavelength is given by $2\pi/k, 2\pi/p$, and $2\pi/q$ for V_p, V_{g_x}, and V_{g_y}, respectively. Note that the phase velocity and the group velocities switch magnitudes, so that small wavelengths show anomalous dispersion and large wavelengths show normal dispersion.

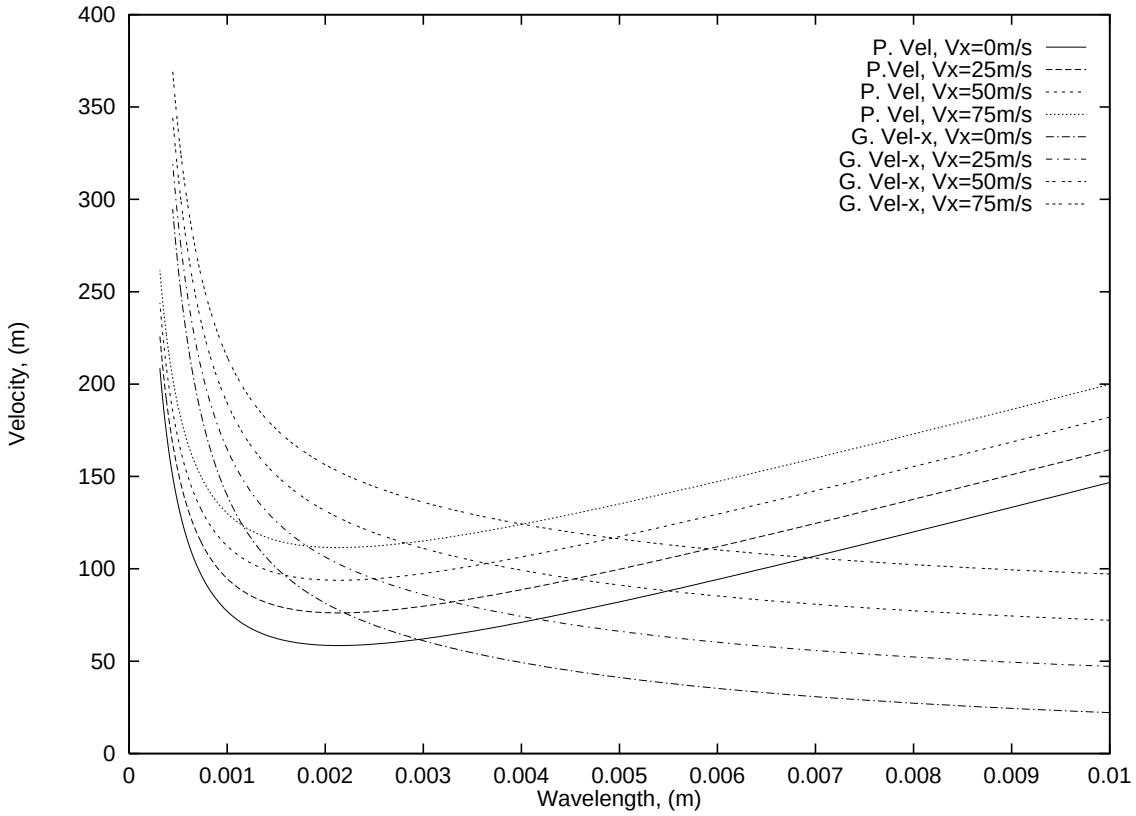

Figure 4-3: Phase and group velocities for different tape transport speeds, $V_x = 0, 25, 50, 75m/s$, at $\theta = \pi/4$. Note that the wavelength is given by $2\pi/k, 2\pi/p$, and $2\pi/q$ for V_p, V_{g_x}, and V_{g_y}, respectively.

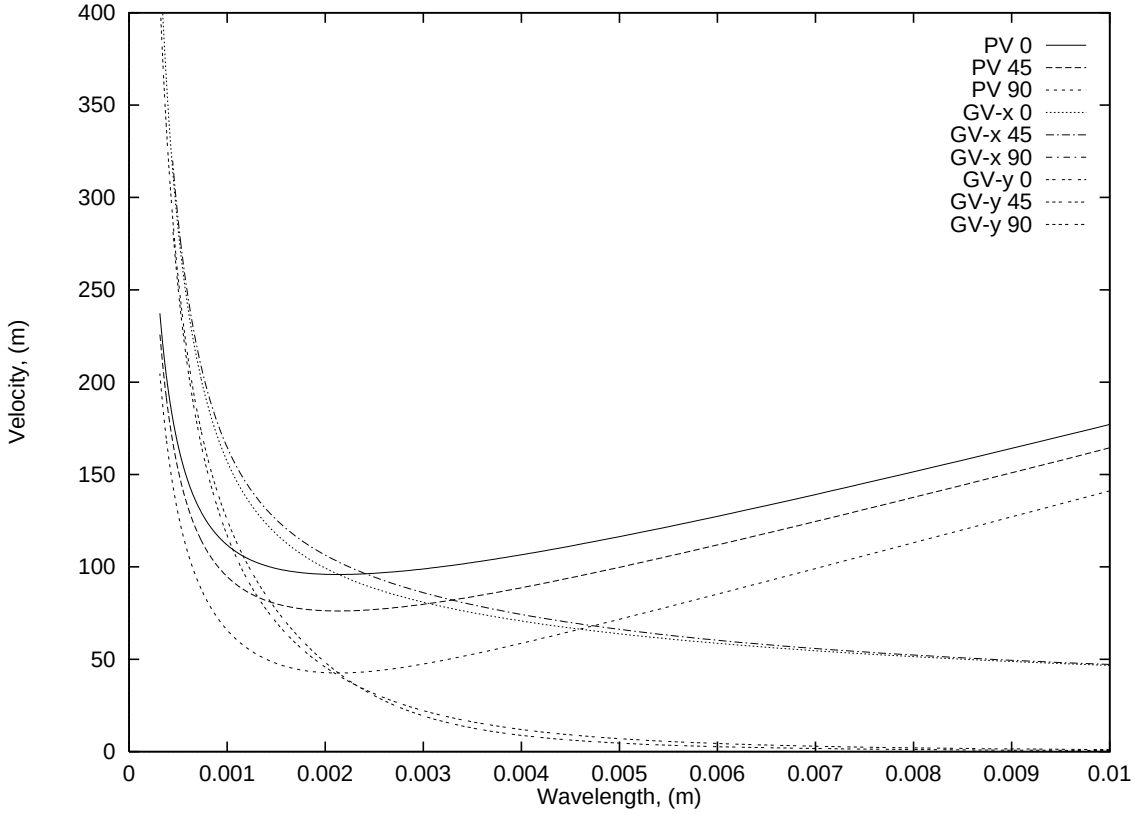

Figure 4-4: Phase and group velocities for different orientations, $\theta = 0, \pi/4, \pi/2$ at tape speed $V_x = 25m/s$. The wavelength is given by $2\pi/k, 2\pi/p$, and $2\pi/q$ for V_p, V_{g_x}, and V_{g_y}, respectively. The phase velocity is highest for the running direction, $\theta = 0$. The x and y direction group velocities coincide for $\theta = 0$ and $\pi/2$ directions.

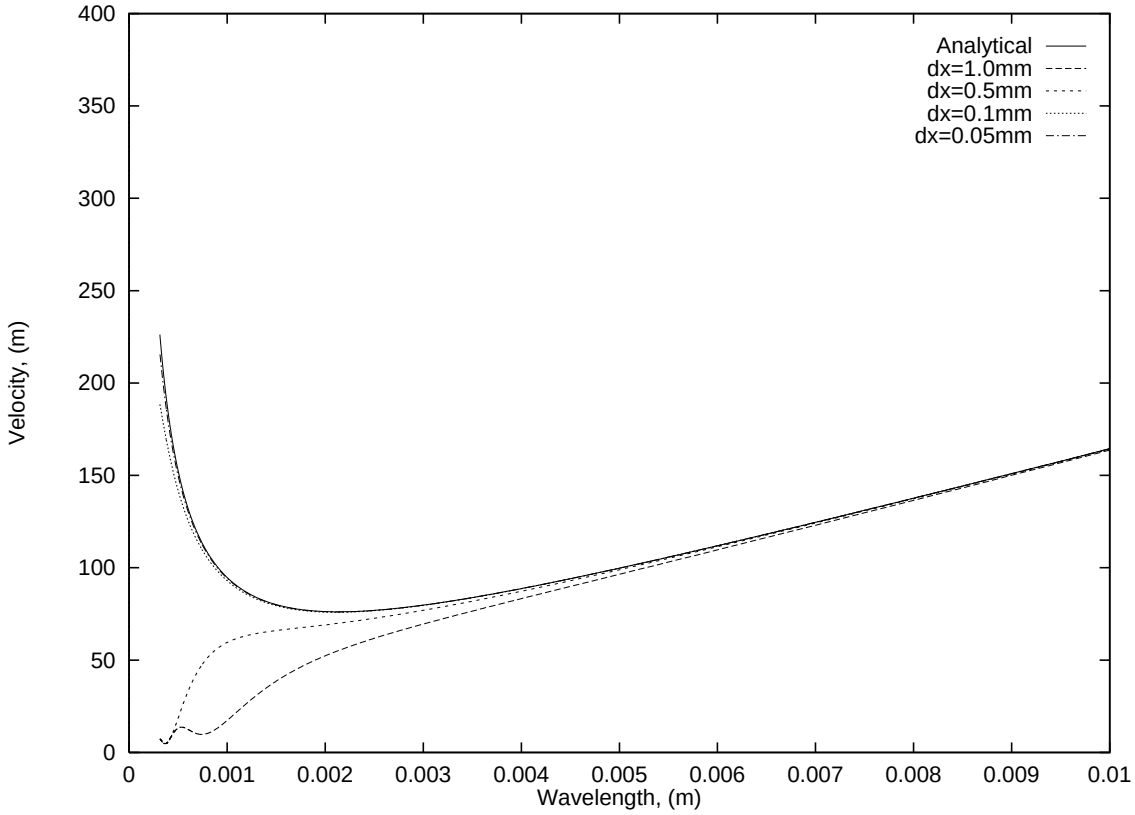

Figure 4-5: The effect of finer Δ on the phase velocity, V_p, predicted by the discretized solution for $V_x = 25m/s, \theta = \pi/4$. As expected, by making Δ smaller the phase velocity curves come closer to the analytical result. Note that the label dx is Δ.

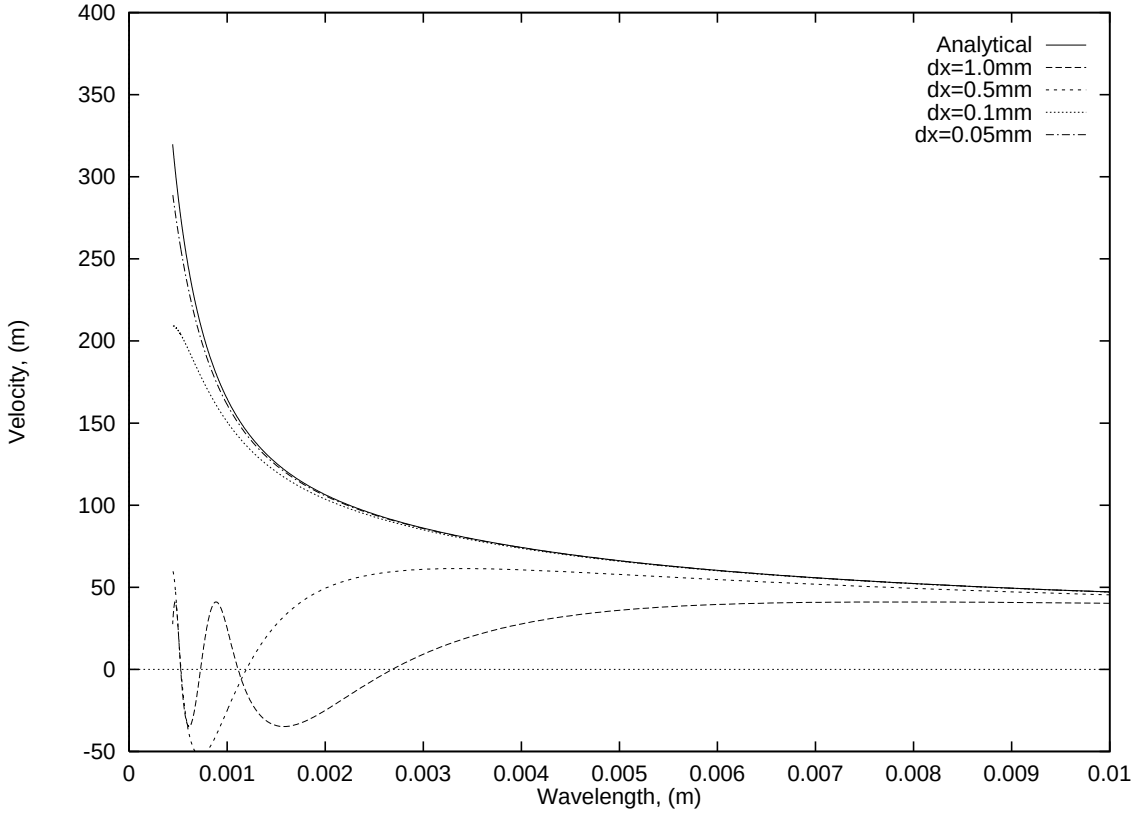

Figure 4-6: The effect of finer Δ on the group velocity, V_{g_x}, predicted by the discretized solution, for $V_x = 25m/s, \theta = \pi/4$. The error is greatly reduced by choosing $\Delta = 0.1mm$ whereas, $\Delta = 1mm$ predicts answers that are entirely wrong. Note that the label dx is Δ.

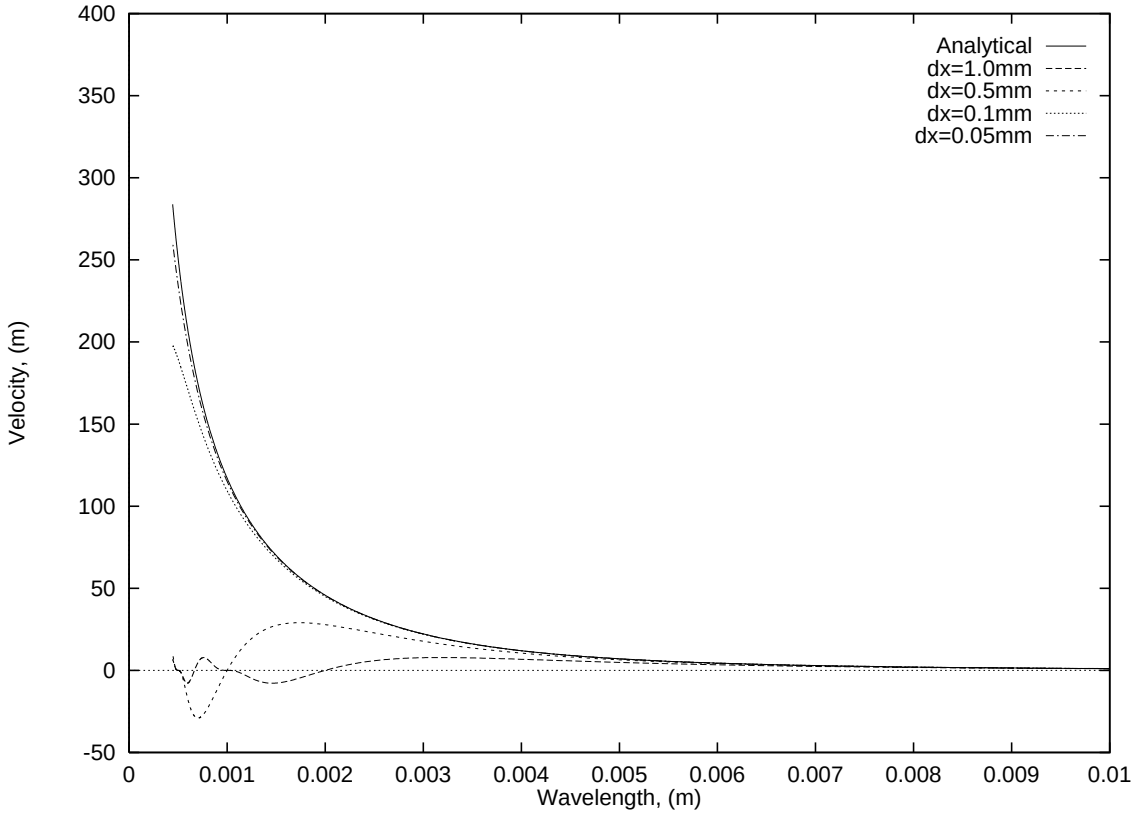

Figure 4-7: The effect of finer Δ on the group velocity, V_{g_y}, predicted by the discretized solution, for $V_x = 25m/s, \theta = \pi = 4$. The numerically obtained group velocity in the x direction for $\Delta = 1mm$ predicts zero velocity. Note that the label dx is Δ.

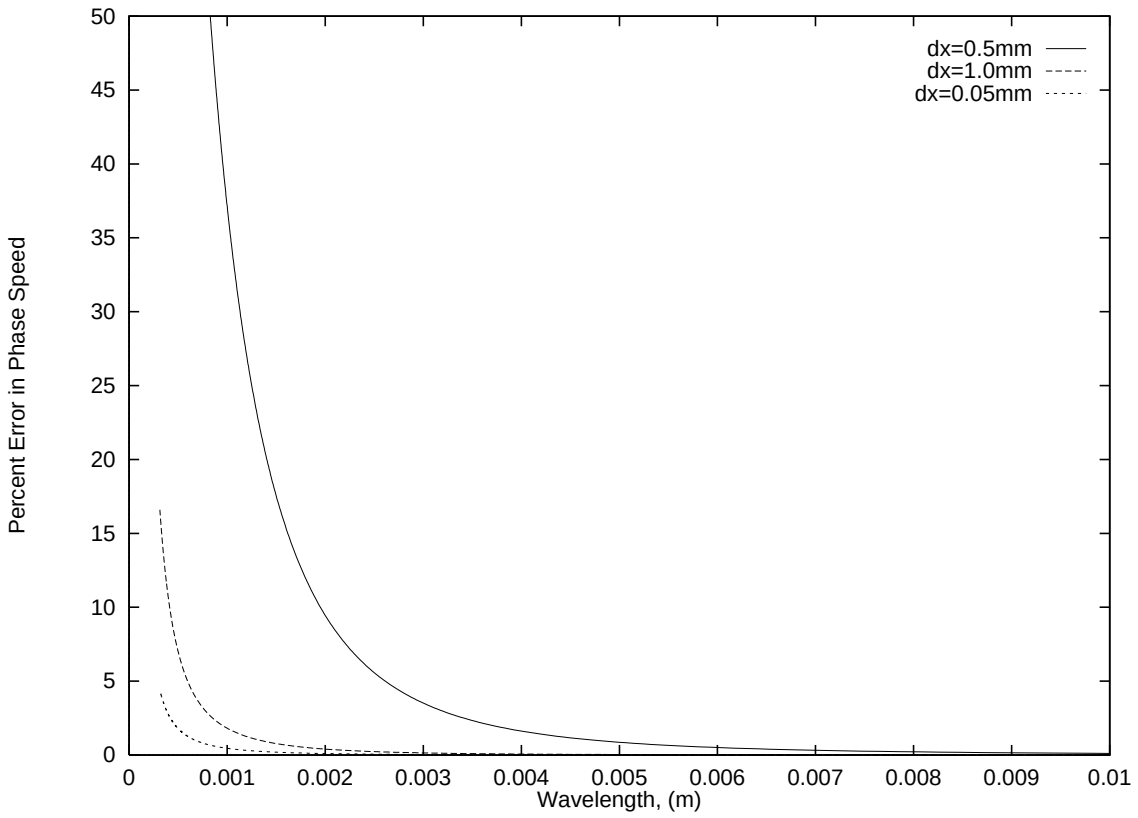

Figure 4-8: The phase velocity error due to discretization, ε_p, variation with Δ, as a function of wavelength , for $V_x = 25m/s, \theta = \pi/4$. Note that the label dx is Δ.

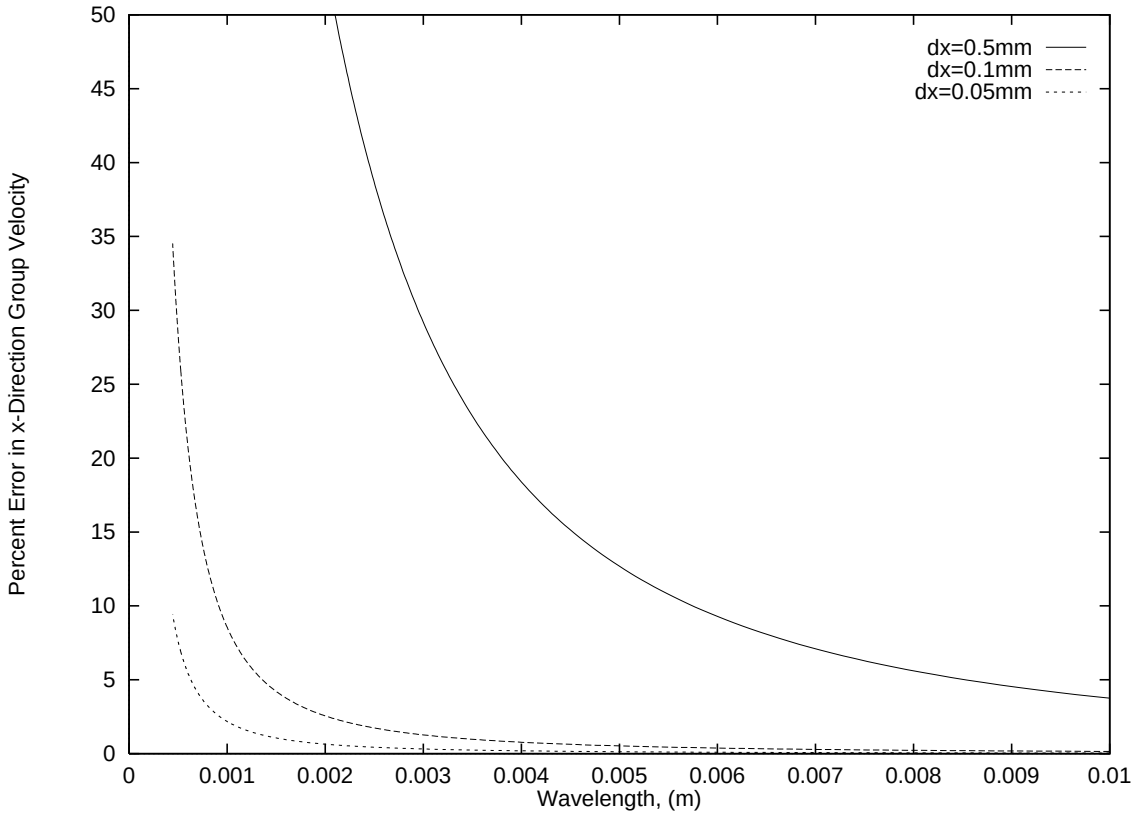

Figure 4-9: The group velocity error in x-direction due to discretization, ε_{g_x}, variation with Δ, as a function of wavelength, for $V_x = 25m/s, \theta = \pi/4$. Note that the label dx is Δ.

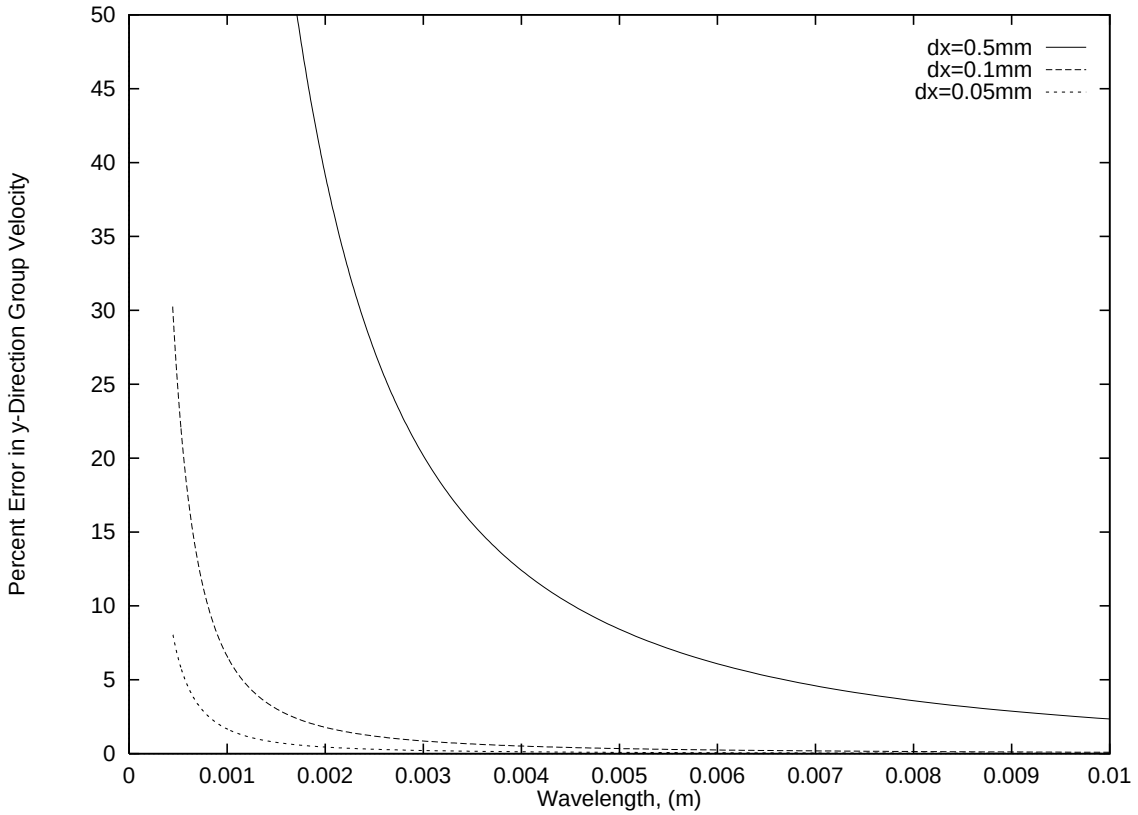

Figure 4-10: The group velocity error in y-direction due to discretization, ε_{g_y}, variation with Δ, as a function of wavelength, for $V_x = 25m/s, \theta = \pi/4$. Note that the label dx is Δ.

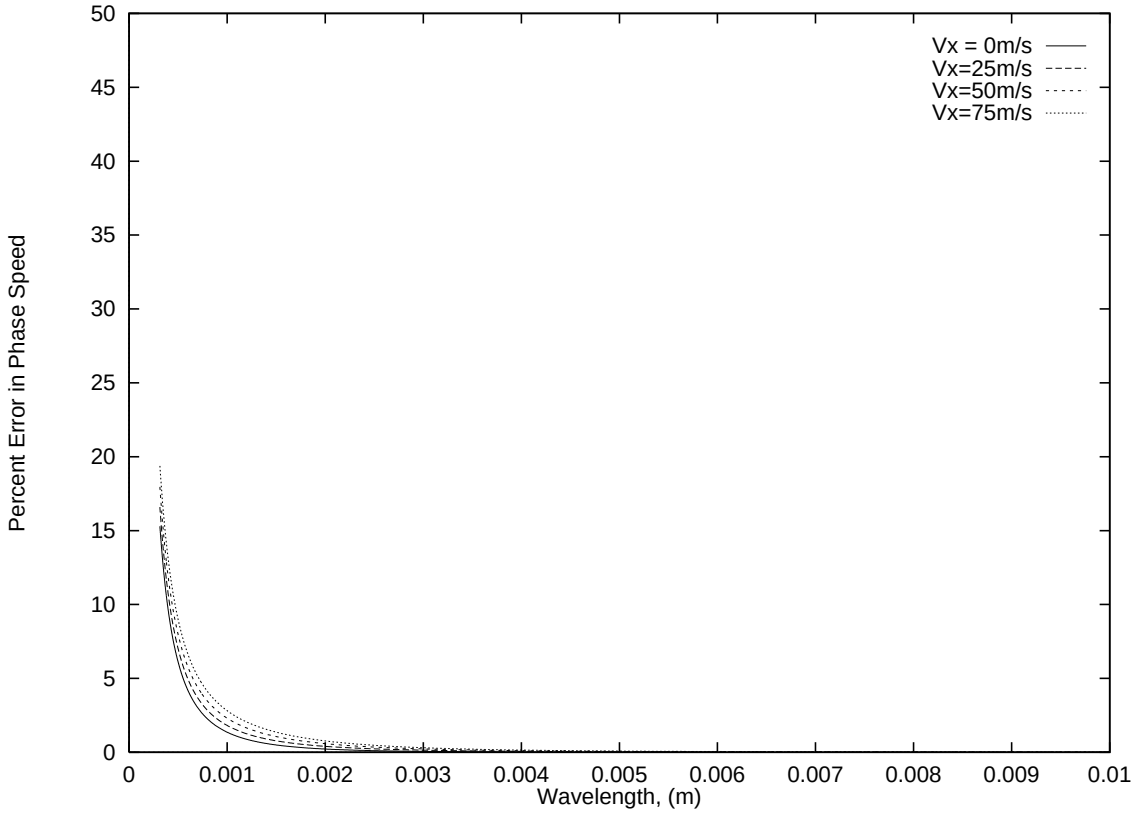

Figure 4-11: The effect of tape transport speed, V_x on the phase velocity error due to discretization, ε_p. The tape speed values are $V_x = 0, 25, 50, 75 m/s$, the orientation is $\theta = \pi/4$, and the spatial step size is $\Delta = 0.1mm$. Note that the error increases at higher tape speeds, but this increase is insignificant.

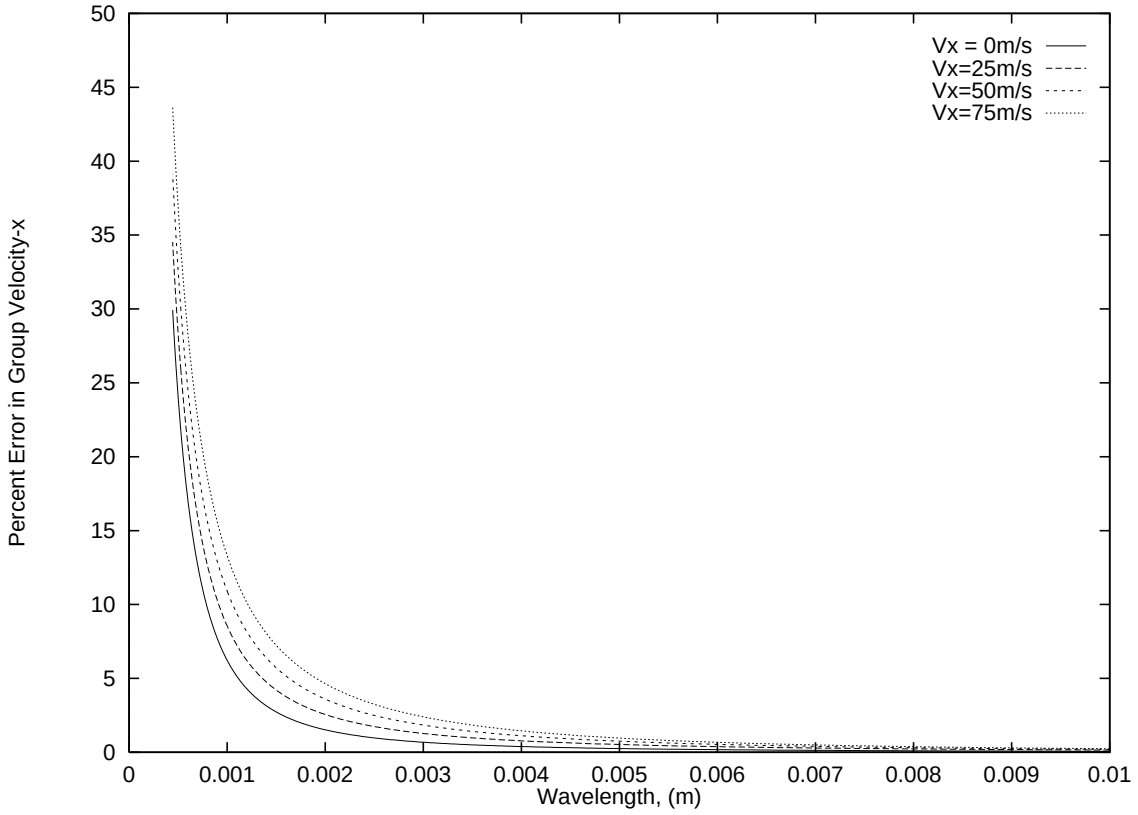

Figure 4-12: The effect of tape transport speed, V_x on the group velocity error due to discretization in x-direction, ε_{g_y}, as a function of wavelength. The tape speed values are $V_x = 0, 25, 50, 75 m/s$, the orientation is $\theta = \pi/4$, and the spatial step size is $\Delta = 0.1 mm$. Note that the error increases at higher tape speeds, but this increase is insignificant.

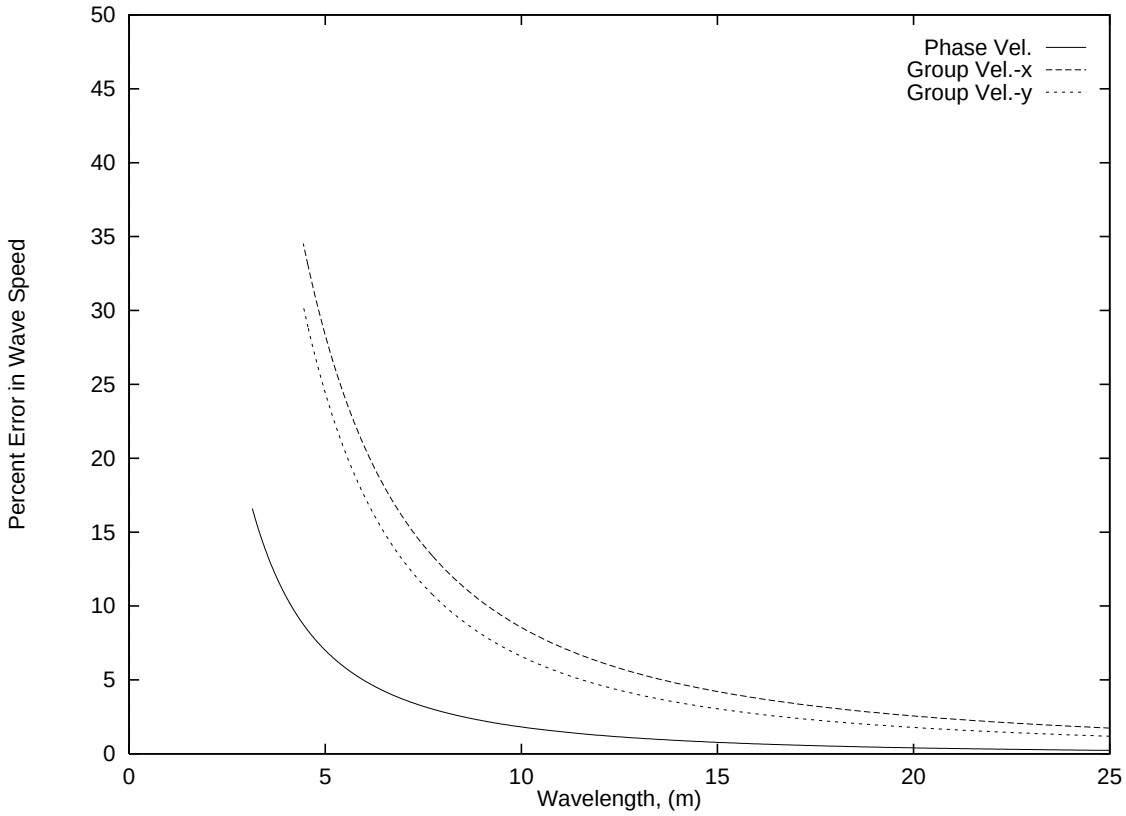

Figure 4-13: The velocity error as a function of λ/Δ, for phase and group velocities. Following parameters are used $V_x = 25m/s$, $\theta = \pi/4$, $\Delta = 0.1mm$. Note that we can predict wave speeds with approximately 10% or better accuracy, for wavelengths $\lambda \geq 10\Delta$. The wavelength is calculated for each type of velocity separately. For example for V_{g_x} corresponding wavelength is λ_{g_x}.

Chapter 5

Numerical Solution of the Transient Displacement of a Circumferentially Moving Cylindrical Shell

5.1 Introduction

In magnetic tape recording control of the tape's displacement as it is transported over guides and recording heads is an important issue. This is especially true in helical-scan recording in which a high velocity read-write head diagonally traverses a magnetic tape that is wrapped around a cylindrical drum in a helical fashion, thus forming magnetic tracks at an angle to the tape length. In this way high data transfer rates can be obtained as a result of the high relative velocity between the head and the tape [43]. However, the quality of the magnetic recording depends on the uniformity of tape deformation that is due to head-tape interaction along a track [60]. This interaction results in a non-symmetrical flexural wave propagation in the tape due to a combination of the following: diagonal path of the head, transient effects at first and last contact of the head with the tape, and wave reflection from the sides of the tape [3], [37].

In this chapter the solution method presented in the Chapter 3 for the equation of

motion is applied to analyze the transient motion of a circumferentially moving cylindrical tape. We, thus, obtain three dimensional transient simulations of flexural waves following a radial load. In this chapter the tape-air interactions, the in-plane tape deflections and the friction and contact between the tape and the underlying surface are neglected.

In the following section we present the effect of numerical damping on the solution. Then we analyze two types of loading. First in Section 5.3 we investigate the effects of a stationary concentrated load on the tape as the tape speed is varied. This system is studied in order to make comparisons with the existing literature. Then in Section 5.4 we look at the case in which the load is allowed to traverse the tape diagonally, as in the case of a recording head of a helical-scan recorder, while the tape is moving slowly.

In this chapter we assume that the tape is wrapped around the cylindrical guide, and that the guide pins are located such that there are not any flat parts of the tape in the analysis domain. See Figure 5-7. Because of this configuration the shell stiffness, K is $Ec/(R^2(1-\nu^2))$ for the entire tape.

5.2 The Effects of Numerical Damping

In Chapter 4 we showed that the high frequency spatial waves are a result of the spatial discretization. In this chapter, in order to be able to introduce numerical damping, we use an implicit time integration method with α damping, as described in Section 3.4.3. To demonstrate the effect of the numerical damping we show three cases with different numerical integration parameters, α, β and γ. These test cases are run with a load that is moving diagonally across the tape as explained in Section 5.4. The parameters of the problem that we considered are given in Table 5.2.

In the first case the Newmark method with $\beta = 1/4$ and $\gamma = 1/2$ is used, and $\alpha = 0$. This case has $O(\Delta t^2)$ accuracy and no numerical damping. In Figure 5-1 a "snapshot" at $t = 240\mu s$ is shown. As there is no numerical damping in this solution any high frequency contribution is retained.

T_x	Tension	$135N/m$
c	Tape thickness	$30\mu m$
V_L	Load Velocity	$90m/s$
V_x	Tape Velocity	$2.5m/s$

Table 5.1: Parameters for Figures 5.1-5.3. Rest of the parameters are identical to that of Table 5.2

To test the effect of numerical damping we ran the same case with the Newmark parameters according to Equation (3.48). In Figure 5-2 we present a case with a small amount of numerical damping where $\alpha = 0, \gamma = 0.55, \beta = 0.275625$. As it can be seen in this figure, this range of parameters affect the amplitude response of the all wavelengths, but no apparent improvement on the high frequency response can be detected.

When we employ the α-method with a comparable amount of dissipation, i.e. $\alpha = -0.05, \gamma = 0.55, \beta = 0.275625$, we recover the same amplitudes as in the first case. This is shown on Figure 5-3. We note that Figures 5-1 and 5-3 are practically identical. From these three figures we conclude that the high frequency reponse for the example parameters that we considered does not constitute a problem. We also confirm that the α method with dissipation gives better results compared to Newmark's method with dissipation.

In a previous study [50], [49] we studied the same problem without using any numerical damping -i.e. $\alpha = 0, \beta = 1/4, \gamma = 1/2$. Here we compared the results obtained in those studies to the results generated with α-dissipation and saw no noticeable difference. Nevertheless, we decided to use the dissipative scheme with $\alpha = -0.05$.

5.3 Simulation of the Effects of a Stationary Load on a Moving Tape

One of the ways to simplify the solution of Equation (2.34) is to make a transformation to a coordinate system that is attached to the magnetic recording head, and study the standing wave pattern that develops at steady state. In this section we are presenting

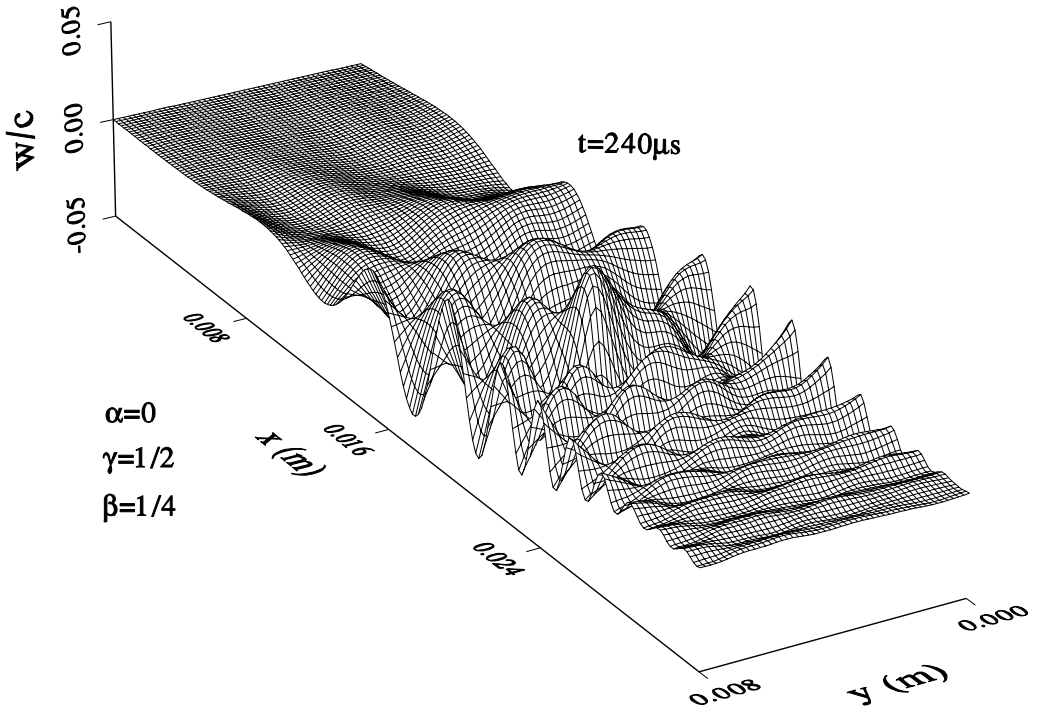

Figure 5-1: The case that is run without numerical damping. Numerical parameters are $\alpha = 0, \gamma = 1/2, \beta = 1/4$.

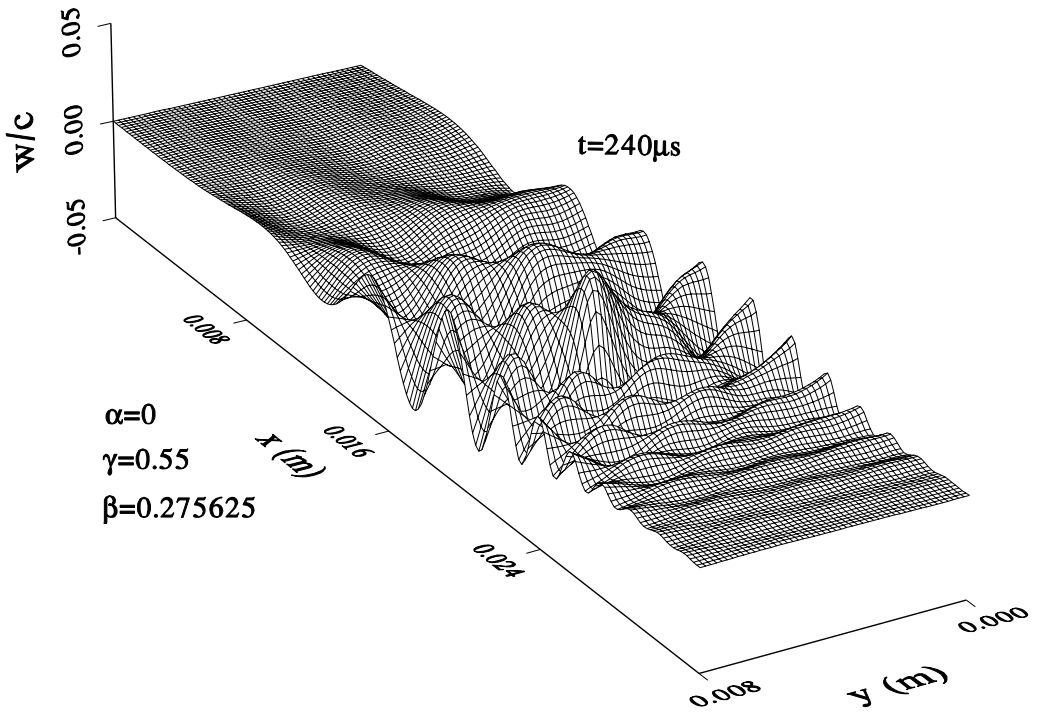

Figure 5-2: The case that is run with numerical damping in the Newmark family. Numerical parameters are $\alpha = 0, \gamma = 0.55, \beta = 0.275625$. The amplitude of the response reduced.

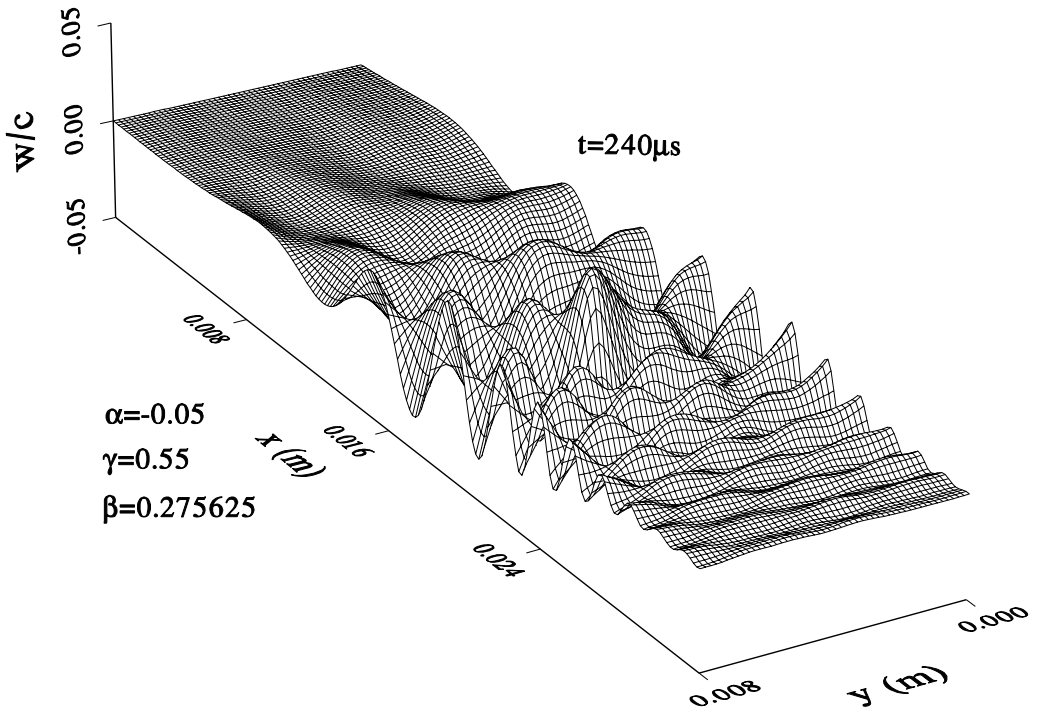

Figure 5-3: The case that is run with α-method damping. Numerical parameters are $\alpha = -0.05, \gamma = 0.55, \beta = 0.275625$. The amplitude response is preserved.

results that are obtained with a similar idea. We apply a time invariant loading to the middle of the tape and study the effects of wave propagation due this loading. To obtain a steady state solution we simply run the code for a long time and obtain a solution that way.

Various investigators studied this problem using analytical techniques. Bogy et al. [10], and Nishida and Hosaka [51] among others, modeled the tape as a cylindrical shell, and computed the steady state tape displacements due to a point load. They have concluded that above a "critical" tape speed the wavelength of the standing wave is smaller upstream of the load in comparison with the wavelength downstream the load. Ono and Ebihara [52] generalized the solution methods for the same problem. Sundaram and Benson [59] solved the transient equations of motion, and investigated the displacements in the cylindrical shell in response to a point load in space applied as a step function in time. Each of these studies represent the tape displacement with infinite series that require calculation of a great number of modes for convergence. The standing wave pattern that is predicted by Bogy et al., and Nishida and Hosaka were qualitatively and experimentally verified by Albrecht et al. [3], Feliss and Talke, and Lacey and Talke [37].

There are few analyses for the transient displacement in a circumferentially moving medium. One exception is Wickert and Mote [70] who studied a traveling string (a spatially one dimensional tape) and showed that mode shapes are non-symmetric when a "gyroscopic" effect is included. This effect vanishes when the tape transport velocity is zero.

The implicit time integration method outlined in Chapter 3 is used here to analyze the time history of a concentrated load. With this method the wave action in the tape is followed by making time history plots consisting of three-dimensional (3D) wire frame drawings. This investigation showed that the continuous reflection and superposition of waves from the *lateral* edges of the tape contribute significantly to the displacement of the load point. We were able to find similar results as the previous studies, on critical tape speed, and dominant period of the displacement at the load point. Moreover, we found

that this dominant period is a function of the tape transport velocity. We also confirmed the dispersive nature of the wave behavior, hence making it impossible to observe a single wave speed. Nevertheless, our time history plots allow for determination of an *apparent* wave speed.

5.3.1 Results and Discussion

The concentrated load is placed at the middle of the tape and is turned on in a step function manner. This is represented mathematically as follows:

$$P = P_o e^{-\bar{\alpha}(x-x_o)^2} e^{-\bar{\alpha}(y-y_o)^2} H(t) \tag{5.1}$$

where, x_o, and y_o mark the centroid of the load, and $H(t)$ is the Heaviside step function. The centroid of the load will be referred to as the *load point* hereafter. The tape was initially in static equilibrium, i.e. $w^o = 0$ and $v^o = 0$. The exponential function in Equation (5.1) is chosen to approximate a concentrated load. The parameter $\bar{\alpha}$ is adjusted so that the function decays to 1% of its maximum within a decay distance of 5% of L_y from the load point. All of the figures related to this section are obtained using the specifications given in Table 5.2.

In Figure 5-4, the transient response of the load point is plotted for $V_x = 0, 50, 70, 80$ and $85 m/s$. The load is located at the center of the tape, $(x_o = \frac{L_x}{2}, y_o = \frac{L_y}{2})$. In order to choose the time step we performed numerical experiments in the range $0.5\mu s \leq \Delta t \leq 12.5\mu s$, on a spatial mesh with $\Delta x = \Delta y = 1.6mm$. We chose the largest possible time step, $\Delta t = 1\mu s$, that did not cause an appreciable difference in the time history of the load point.

We note from Figure 5-4 that at lower tape speeds, the tape motion consists of the superposition of several modes with one dominant period. For the case of $V_x = 0$ the dominant period is close to $2\pi(\rho_a/k)^{\frac{1}{2}}$, which is approximately $50\mu s$ for the specifications of this problem. We also note that the displacement of the tape decays within an envelope that asymptotes at a finite amplitude. As Equation (2.34) does not have a dissipative

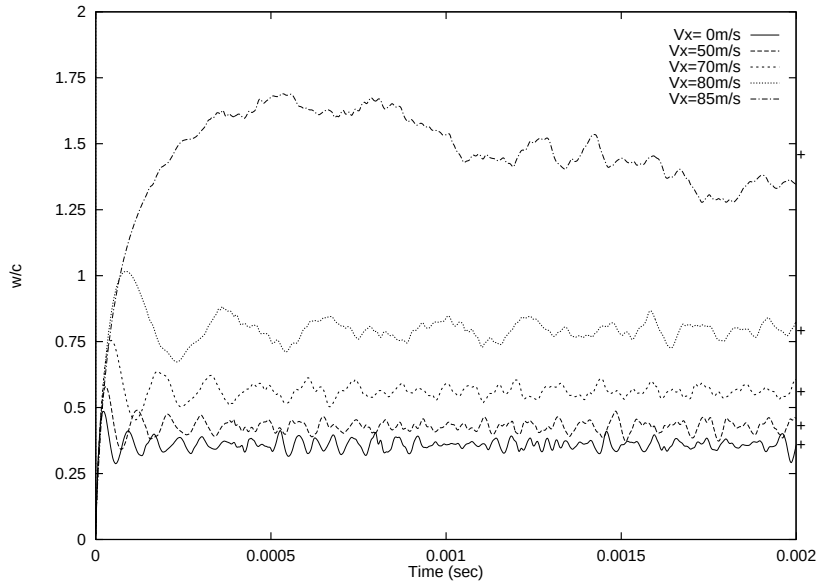

Figure 5-4: Transient displacement of the load point ($x_o = L_x/2, y_o = L_y/2$) for a concentrated step load as a function of tape velocities, $(0, 50, 70, 80, 85m/s)$. Numerical parameters are $\alpha = -0.05, \gamma = 0.55, \beta = 0.275625$.

D	Bending rigidity $(= \frac{Ec^3}{12(1-\nu^2)})$	2.9x10^{-6}Nm
k	Shell stiffness $(= \frac{Ec}{R^2(1-\nu^2)})$	219.8x10$^{6}N/m^3$
E	Young's Modulus	4x10^{9}Pa
ν	Poisson's ratio	0.3
ρ_a	Shell density per unit area	0.014 kg/m^2
R	Radius of the shell	2x10^{-2}m
c	Shell thickness	20x10^{-6}m
$\frac{T_x}{R}$	Belt wrap pressure	$4500Pa$
T_x	Tension per unit length	$90N/m$
L_y	Width of the tape	6.35x10^{-3}m
L_x	Length of the tape	$4L_y$
P_o	Concentrated load Magnitude	200 Pa
$\Delta x = \Delta y$	Spatial Step	1.549x10^{-4}m
Δt	Time Step	2x10^{-6} s
α	Parameter for α-Method	-0.05
β	Parameter for α-Method	0.275625
γ	Parameter for α-Method	0.55

Table 5.2: Variables and typical values for a magnetic recording application

term[1] the tape displacement will asymptote on a quasi-periodic motion around a steady state value. Similar observations were also made by Sundaram and Benson [59]. The dots on Figure 5-4 indicate the non-dimensional displacements at steady state. These values were separately obtained by running the program with parameters $\alpha = 0, \beta = 1$ and $\gamma = 3/2$.[2] The steady state values obtained in this way match the static solution of Equation (2.34).

Furthermore, from Figure 5-4, we observe that the dominant period and the mean displacement increases as the velocity of the tape is increased. These increases are non-linear functions of velocity, and a very large change is observed near $V_x = 85m/s$. Increasing tape transport velocity has an effect of reducing the effective tape tension, $T_{eff} = T_x - \rho V_x^2$. See Equation (2.34). At the transport speed,

$$V_x = \sqrt{\frac{T_x}{\rho_a}} \tag{5.2}$$

the effective tape tension vanishes. At tape transport speeds above this value T_{eff} becomes compressive, and the tape becomes prone to *buckling*. However, the shell stiffness, K, acts as a spring foundation and prevents the immediate appearance of buckling. As the tape transport speed is increased, the in-plane compression created by the effective tension can no longer be counteracted by the resisting effect of the shell stiffness and unbounded displacements occur. The speed at which this phenomenon occurs is called as the *critical* tape speed.

We have found that for the parameters used in this paper, a small positive change in the transport speed from the value $V_x = 85m/s$ causes the unbounded displacements. This value lies between the values calculated by using the approximate critical tape speed expressions that are derived by Wickert and Mote [70], (80 m/s), and Sundaram and Benson [59], (111 m/s). The difference can be explained as follows; in Wickert and Mote, the expression for the critical tape speed is derived for an axially moving beam,

[1] The displacement decay is due to dispersion.

[2] This choice of the integration parameters is used to introduce the maximum amount of damping to reach the steady state quickly [34].

hence the shell stiffness term does not play a role which explains the reason for a lower bound approximation. In Sundaram and Benson, on the other hand, the expression for the critical tape speed is derived for a cylindrical shell simply supported on all of its sides. In our study the tape is modeled as having two free edges, which simulates a structure which would have lesser resistance to buckling loads. Therefore, we find it natural to observe a critical tape speed less than that given by Sundaram and Benson, and greater than that given by Wickert and Mote.

Figures 5-5 and 5-6 show 3D wire frame time history plots of the tape response to two different tape transport velocities, $V_x = 0$ and $50m/s$. These figures show that step loading, (5.1) causes displacements waves in the tape. When $V_x = 0$, waves propagate radially away from the load point, and are symmetrical with respect to the $x = \frac{L_x}{2}$ line. Due to applied tension, the tent-like shape of the displaced tape has an ellipsoidal "footprint" whose major axis is aligned with the tensioned direction.

The waves that reflect from the free edges travel back toward the source. From Figures 5-5 and 5-6, it can be observed that first wave reflection from the free edges occurs near time $t = 30\mu s$. By the time the forward traveling wave front reaches the simply supported edge, several side-to-side wave interactions have already occurred. We believe that the wave reflection from the free edges explains the major reason for the non-periodic behavior of the load point in Figure 5-4.

Figure 5-6 demonstrates the effect of the tape transport velocity ($V_x = 50m/s$) on the wave profiles. In this figure we see that the wavelength of the displacement is larger downstream of the load, than upstream of the load. This was also predicted by the steady state analysis of Bogy et al. [10] and observed experimentally by Lacey and Talke [38] among other investigators.

Comparison of Figure 5-5 to Figure 5-6 shows that the wave front traveling toward the support on the downstream side of the tape has a shorter travel time when the tape transport speed is increased. This result agrees well with the results obtained in Chapter 4 for the x direction group velocity given in Equation (4.19). Numerical

simulations showed that determination of a wave speed is not straight forward. Because the governing equation is dispersive, as shown in Chapter 4, wave fronts with small wavelengths reach the simply supported boundaries in a shorter time than the ones with longer wavelengths[3]. We are able to visually detect only a simple dominant wave front by looking at Figures 5-5 and 5-6.

[3]See Figure 4-2.

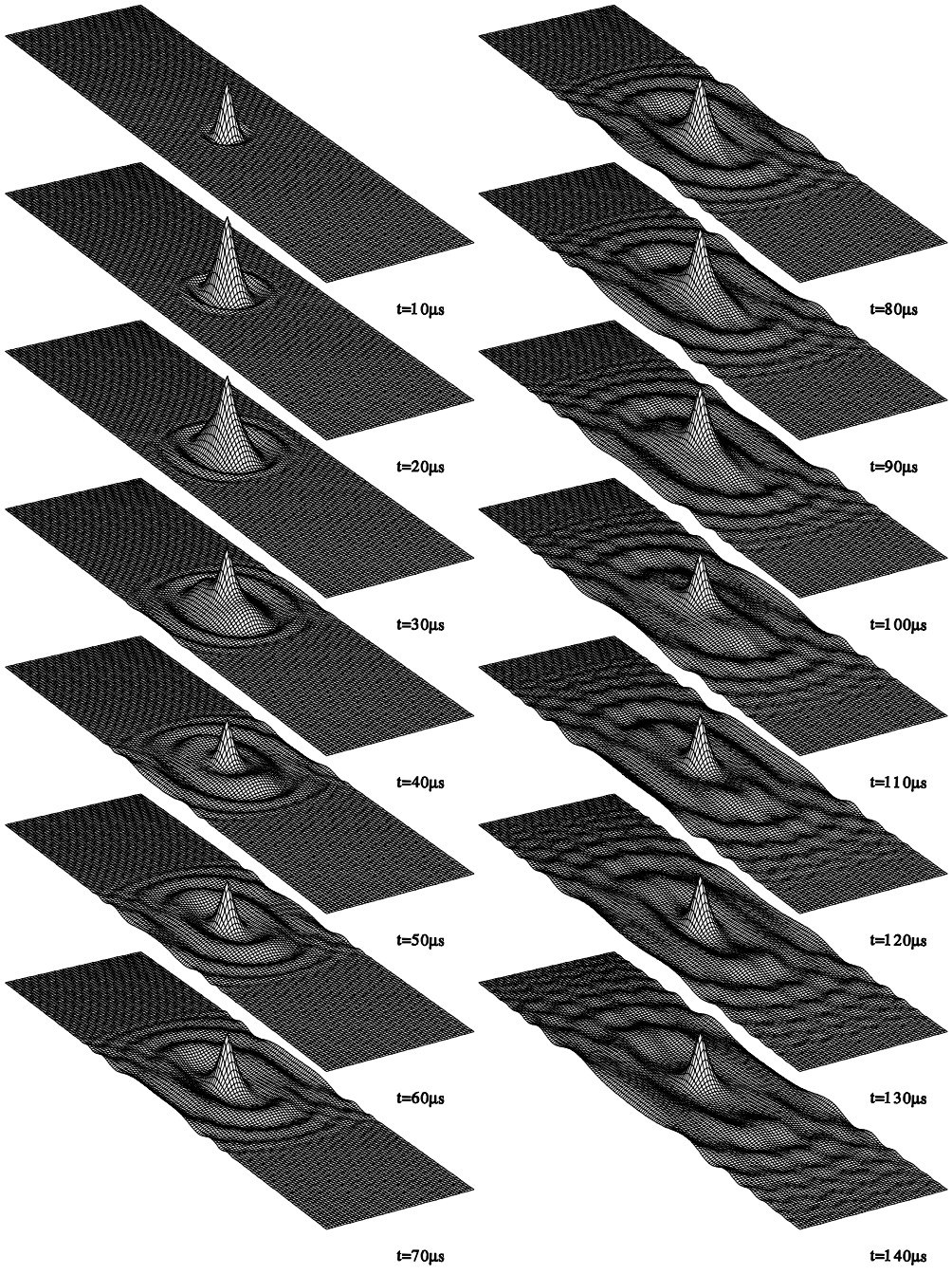

Figure 5-5: Displacement Wave Propagation of the Tape in Response to a Concentrated Step Load, $V_x = 0m/s$.

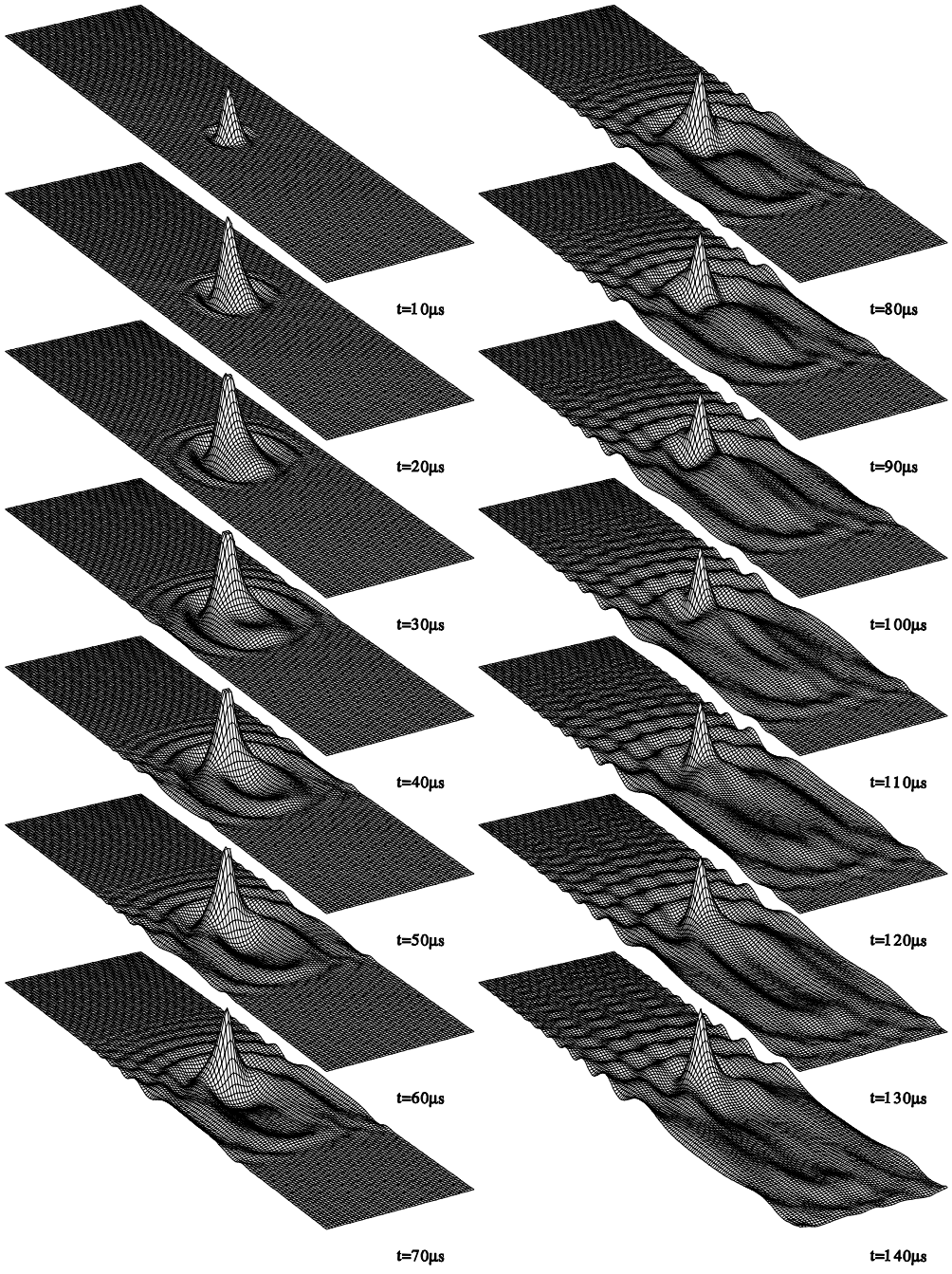

Figure 5-6: Displacement Wave Propagation of the Tape in Response to a Concentrated Step Load, $V_x = 50m/s$. Tape motion is in the + x direction.

5.4 Wave Action Due to a Concentrated Load Moving on a Circumferentially Transported Tape

In this section we are presenting the effects of a moving load acting on a circumferentially moving cylindrical shell. This is done as a first approximation to simulate the interaction between the tape and the recording head of a helical-scan recorder. This analysis is limited because the air lubrication effects, and the contact between the tape and the helical-scan drum, as well as the resulting friction are neglected. Leaving the air lubrication out of the solution results in prediction of more flexural waves than observed by the experimental study by Lacey and Talke [37].

The moving load is modeled by Equation (5.1). The load center moves according to the following line,

$$x_o(t) = V_L t cos\Gamma + x_i$$
$$y_o(t) = V_L t sin\Gamma + y_i \tag{5.3}$$

where, V_L is the speed of the load, Γ is the skew angle (see Figure 5-7), and (x_i, y_i) is the initial location of the load. Here, Γ and (x_i, y_i) are 14^o and $(0, 7.4)mm$, respectively.

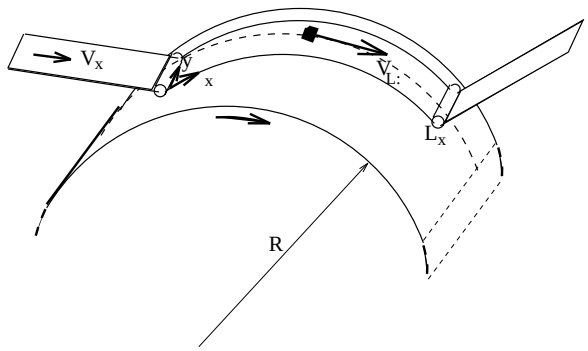

Figure 5-7: Tape configuration in helical-scan recording

5.4.1 Results and Discussion

Each one of Figures 5-8-5-13 shows five wire frame snapshots of the wave propagation at the same load locations along a track. The displacement w is non-dimensionalized by using thickness c. Note that magnification in the z-direction is different on each figure.

In Figure 5-8 the load velocity is $V_L = 50m/s$. A predecessor wave front is seen in this figure as the flexural waves created by the load propagate in the tape faster than the load itself. The non-symmetrical wave front, seen in this figure is attributed to the skewed load path. Figure 5-9 shows the case of $V_L = 80m/s$ at which the load and the predecessor waves have nearly the same speed. This load speed is called the *critical load speed*, $V_{L_{cr}}$. Note that in Figures 5-8 and 5-9 the wave front is essentially straight and moving in the longitudinal direction of the tape. When the load speed is faster than the critical value, the load penetrates the wave front which becomes V-shaped, as seen in Figure 5-10, for $V_L = 100m/s$.

In order to investigate the factors that affect the critical speed, the tape tension, T_x, thickness, c, and tape transport speed, V_x, were changed while the load speed, V_L, was kept constant at $80m/s$. Figure 5-12 shows that increasing the tape tension to $T_x = 135N/m$ restores subcritical conditions, i.e. the predecessor waves return. In Figure 5-11 the tape thickness is doubled to $c = 20\mu m$. Predecessor waves are also visible in this case, and the maximum displacement of the tape reduced significantly, due to increased resistance from shell stiffness, K. The effect of increasing the tape transport speed to $V_x = 25m/s$, on the critical speed is shown in Figure 5-13. In this case, too, an increase in the critical wave speed of the tape is observed.

This study also showed that there is more free edge flutter in thicker tapes than in thinner ones (see Figures 5-9 and 5-11). Near $V_{L_{cr}}$ severe wave interaction may occur near the location where the load leaves the tape (see Figure 5-9).

5.5 Conclusions

In section 5.3 we studied the interaction of a moving tape and a stationary concentrated load. In that section we showed that the wave front propagating in the width (or axial) direction has a substantial effect on the displacement behavior of the load point. As this wave is reflected from the free edges, it contributes to the displacement amplitude of the load point which eventually settles into an *envelope* over time. We concluded that the reason for the irregular load point displacements within this envelope is the continuous superposition of the waves reflecting from the free lateral edges of the tape. We confirmed the observations in [59] that the load point displacement, however irregular looking, has a dominant period which is approximated by $2\pi(\rho_a/k)^{\frac{1}{2}}$ for $V_x = 0$. This period is found to increase with increasing tape transport velocity.

We also observed a critical tape transport speed that was predicted by other investigators. However, since we modeled the lateral sides of the tape as free edges, we were able to evaluate the critical tape transport speed closer to its actual value than predicted by alternative models with different boundary conditions.

In section 5.4 we investigated the a moving tape's response to a moving concentrated load. Through numerical experiments we estimated the critical conditions for which the wave propagation speed equals the load speed. The critical speed was seen to increase with higher tape tension, higher tape transport speed and in thicker tapes.

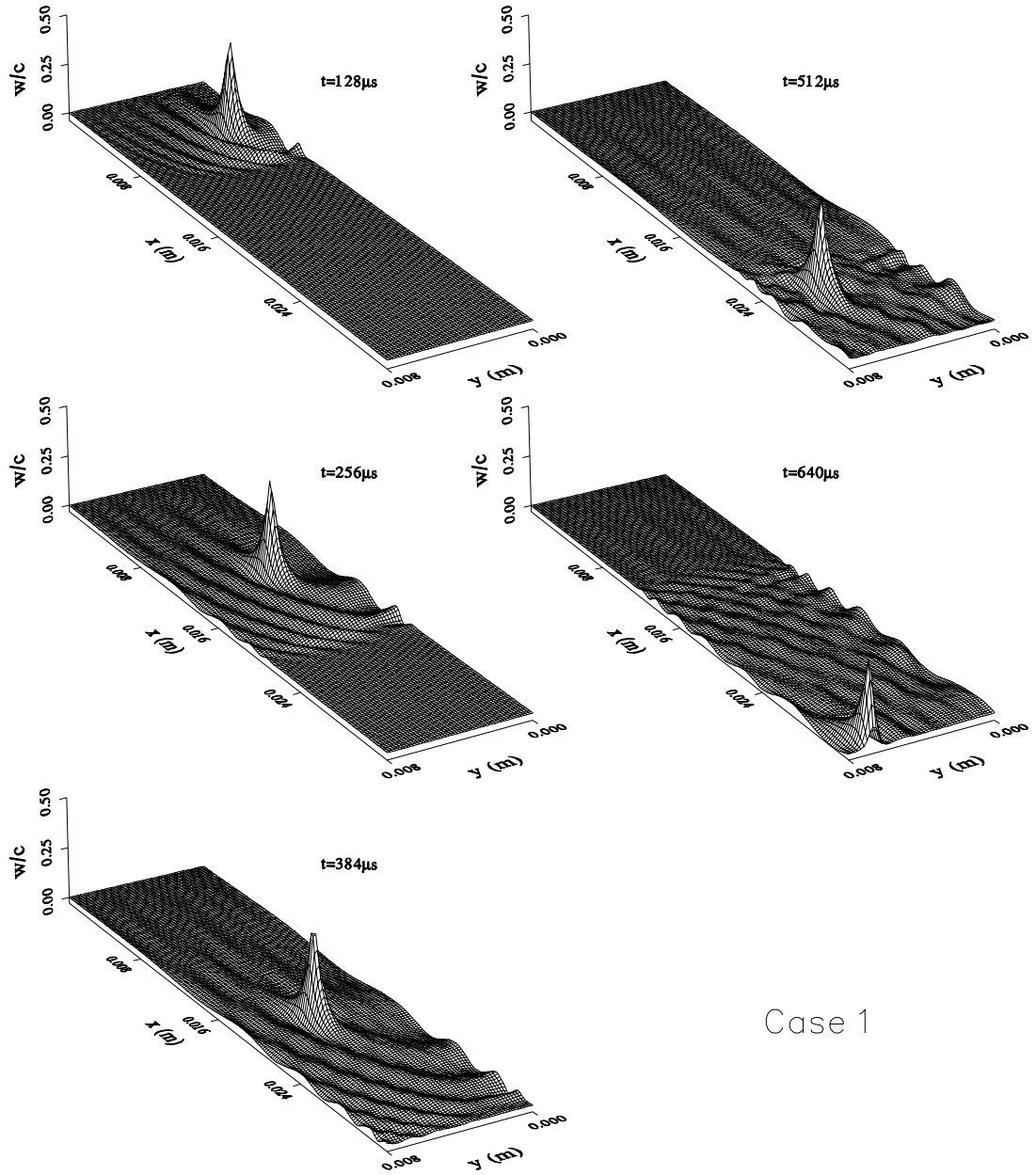

Figure 5-8: Tape deflections at subcritical head velocity, $V_L = 50m/s$. Problem parameters are $c = 10\mu m, T_x = 90N/m, V_x = 2.5m/s$ and $\alpha = -0.05, \beta = 0.275625, \gamma = 0.55$. Tape motion is in the + x direction.

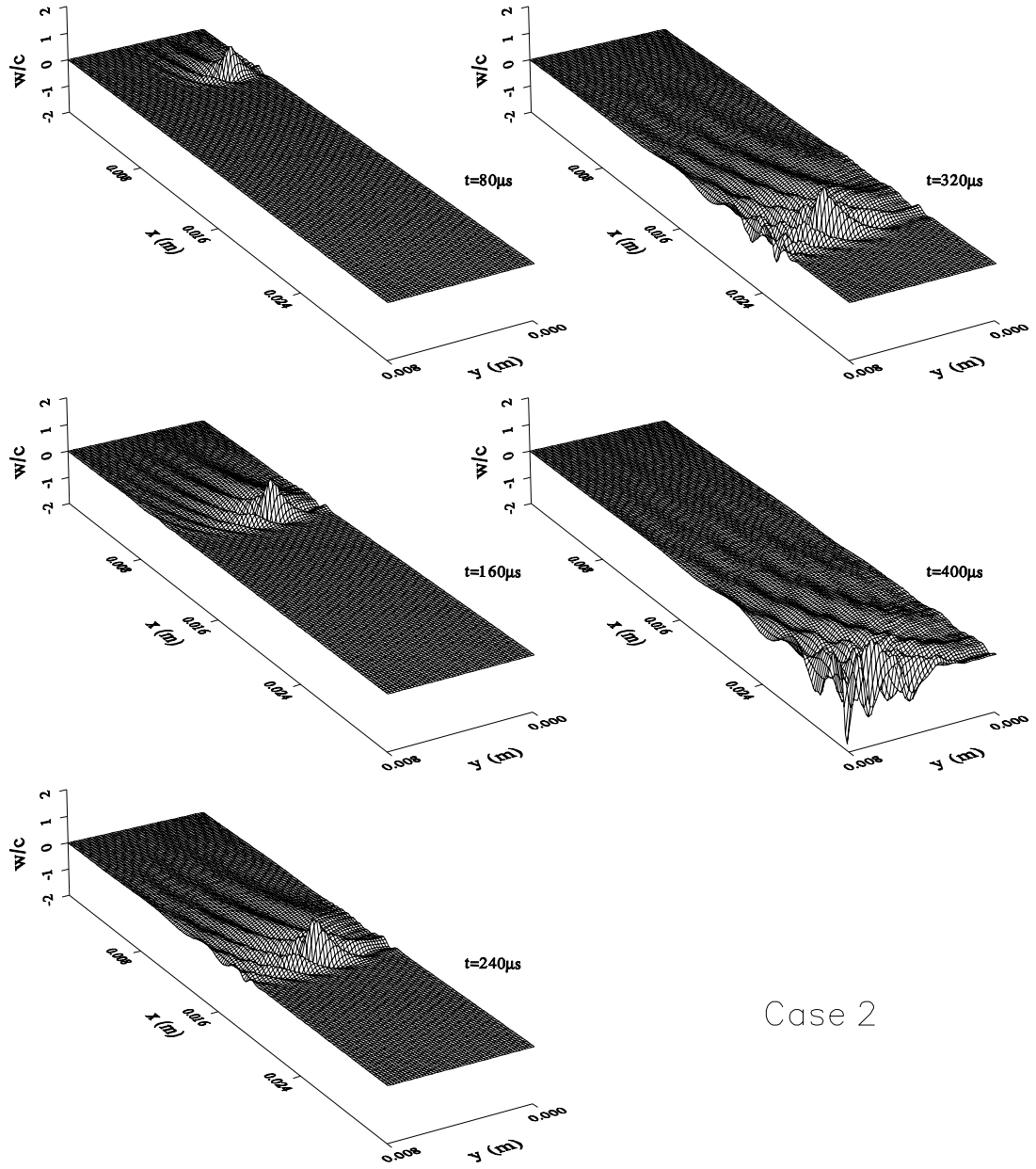

Figure 5-9: Tape deflections near critical head velocity, $V_L = 80m/s$. Problem parameters are $c = 10\mu m, T_x = 90N/m, V_x = 2.5m/s$ and $\alpha = -0.05, \beta = 0.275625, \gamma = 0.55$. Tape motion is in the $+$ x direction.

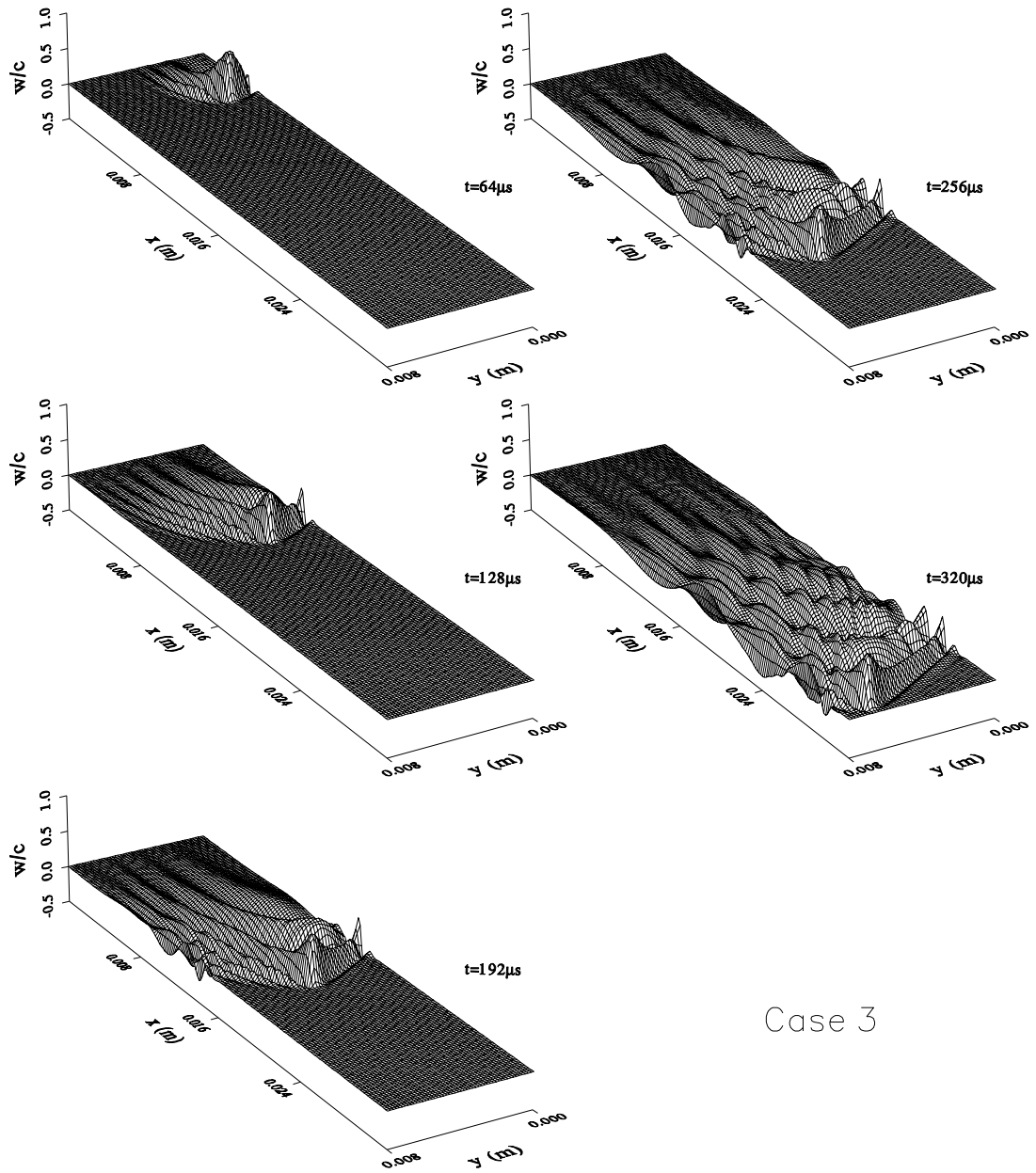

Figure 5-10: Tape deflections at super-critical head velocity, $V_L = 100m/s$. Problem parameters are $c = 10\mu m, T_x = 90N/m, V_x = 2.5m/s$ and $\alpha = -0.05, \beta = 0.275625, \gamma = 0.55$. Tape motion is in the $+$ x direction.

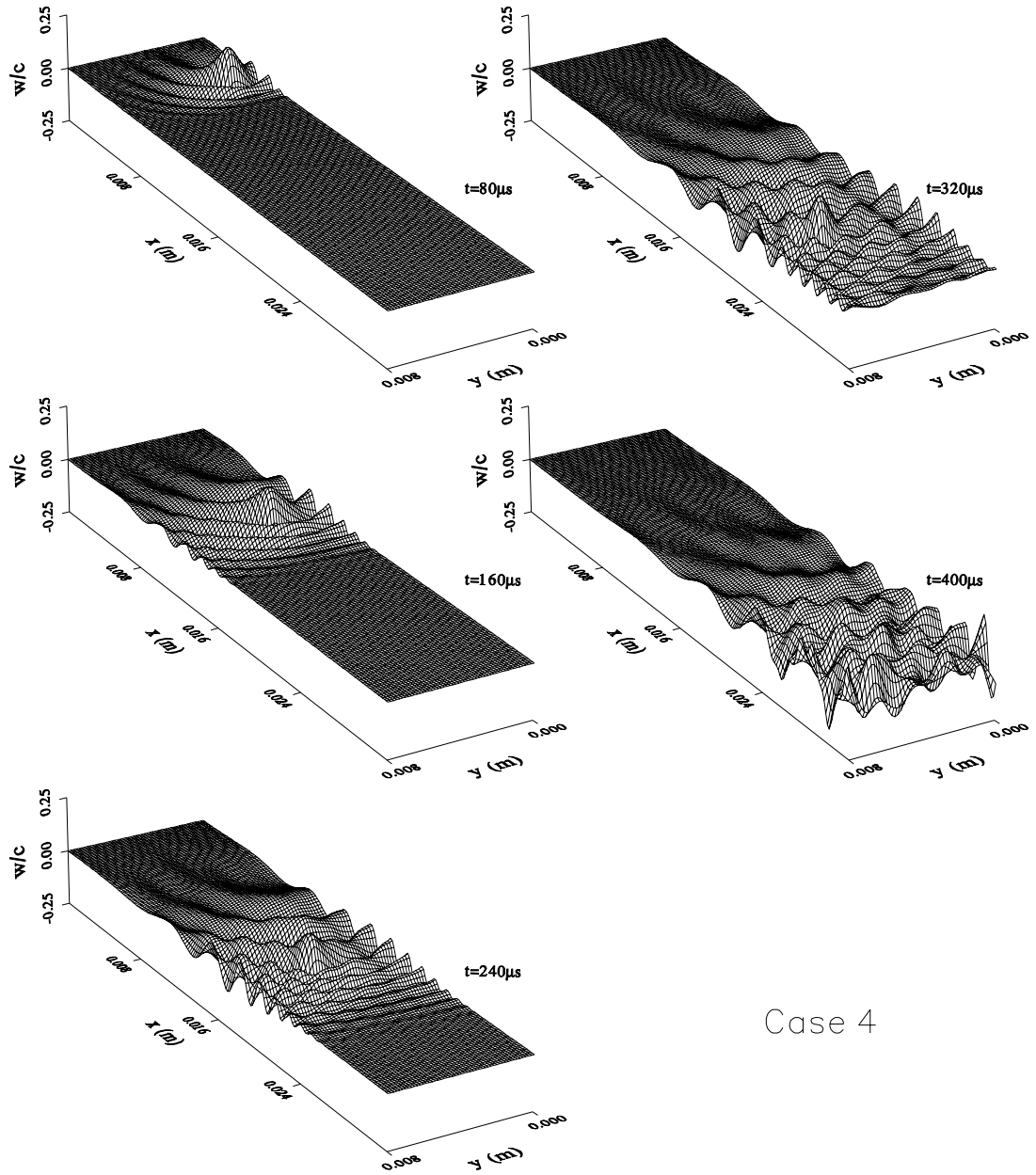

Figure 5-11: The effect of increasing the tape thickness on the critical head velocity, $c = 20\mu m$. Problem parameters are $V_L = 80m/s, T_x = 90N/m, V_x = 2.5m/s$ and $\alpha = -0.05, \beta = 0.275625, \gamma = 0.55$. Tape motion is in the $+ x$ direction.

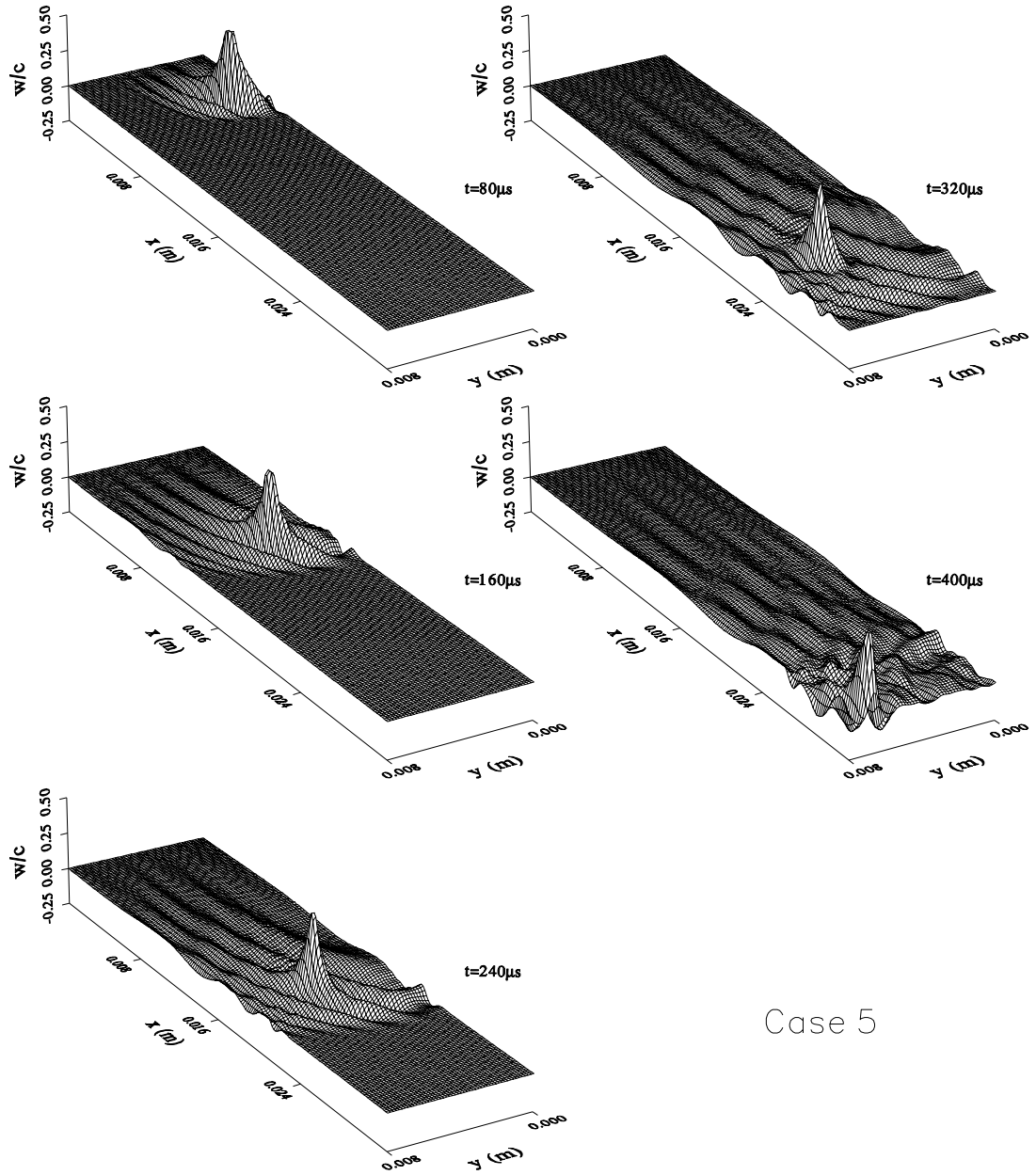

Figure 5-12: The effect of tension increase on the critical head velocity, $T_x = 135N/m$. Problem parameters are $c = 10\mu m, V_L = 80m/s, V_x = 2.5m/s$ and $\alpha = -0.05, \beta = 0.275625, \gamma = 0.55$. Tape motion is in the $+$ x direction.

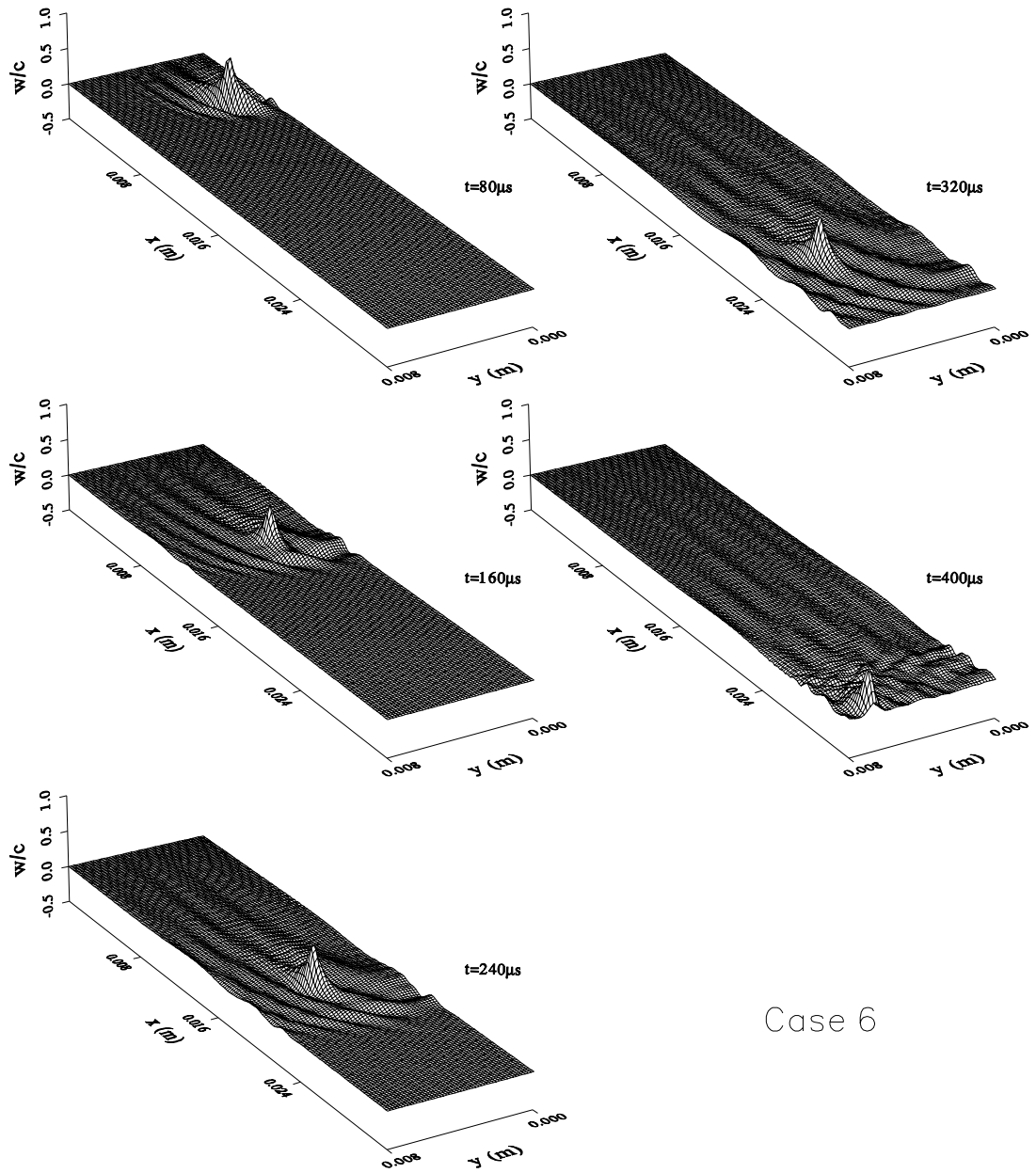

Figure 5-13: The effect tape transport speed increase on the critical head velocity, $V_x = 25m/s$. Problem parameters are $c = 10\mu m, V_L = 80m/s, T_x = 90N/m$ and $\alpha = -0.05, \beta = 0.275625, \gamma = 0.55$. Tape motion is in the + x direction.

Chapter 6

Foil Bearing Problem for a Large Angle of Wrap and Infinitely Wide Tape

6.1 Introduction

The interaction of a flexible magnetic recording tape and air when the tape is transported over a rigid surface, is called the foil bearing problem. As the tape moves, the air that is entrained between the tape and the rigid guide experiences a pressure increase. This super-ambient pressure causes the tape to deflect away from the rigid guide. However, any tape deflection affects the air pressure, because the air pressure and the gap height between the rigid surface and the tape are closely coupled. This system eventually finds a state where the tape deflection and the air pressure acquire steady values.

Experimental studies show that in the steady state the tape takes a "cupped"[1] shape. As a consequence of cupping the two sides of the tape usually have a lower gap height than

[1]The cupped shape can partly be attributed the anti-clastic curvature effects, and partly to the fact that the tape is exposed to ambient pressure at the sides. Due to the latter condition the net air pressure on the tape edge is zero leading to less deflection on the free edges. See Figure 7-6.

the middle region. This situation prevents the air leakage from the sides of the tape [67]. In linear recording applications magnetic tracks are usually laid in the middle region of the tape, therefore the non-uniformity in the gap height on the sides becomes a less important issue. For this type of applications the tape is, usually, modeled by using a beam type of formulation, and the air lubrication effects are modeled by using the one dimensional Reynolds equation. See for example [58]. In this thesis, the problem described above is called to the *one-dimensional (1D)* foil bearing problem, or the *infinitely wide* foil bearing problem.

Recently published studies on the 1D foil bearing problem treat the tape as a beam whose reference configuration is the flat state of the tape (line $\bar{Y} = 0$ in Figure 2-3) [1, 2, 11, 24, 29, 38, 58]. This approach to tape modelling allows the study of non-circular head shapes to a certain extent. However, the applications of this approach are limited to small wrap angles since the head penetration above this reference state is usually several orders of magnitudes bigger than the tape's thickness. Actually, even when the wrap angle is small the validity of the beam equation is violated[2]. In Chapter 2 we presented an alternative formulation in which the reference configuration of the undeflected tape is taken as the surface of the cylindrical head. We are later going to use the results of the 1D study as initial conditions for the finite width (2D) problem.

6.2 Governing Equations

Neglecting side-flow of air, the modified form of the Reynolds equation, (2.58), which takes into account the molecular rarefaction effects at low bearing clearances, is used to model the air lubrication,

$$\frac{d}{ds}(h^3 p\frac{dp}{ds}) + 6\lambda_a P_a \frac{d}{ds}(h^2\frac{dp}{ds}) = 6\mu_a V_x \frac{d}{ds}(ph) + 12\mu_a \frac{d}{dt}(ph) \tag{6.1}$$

[2]The beam equation is valid for deflections less than the thickness of the beam. When the displacement becomes large the middle surface of the beam stretches and the beam behaves additionally stiff, [65]

In this equation p is the air pressure, h is the distance between the two lubricated surfaces, s is the spatial coordinate on the rigid guide in the circumferential direction, t is time, P_a is the ambient air pressure, λ_a is the mean free length for the air molcules, μ_a is the viscosity of air, and V_x is the tape velocity. See Figure 2-3.

The equation of motion of a thin cylindrical shell is used to model the tape displacement. As the side flow of air in the Reynolds equation is neglected, we also neglect the axial variation of the tape deflection. Thus the equation of motion of the tape, (2.34), reduces to beam formulation that we mentioned above,

$$D\frac{\partial^4 w}{\partial x^4} + Kw + (\rho_a V^2 - T_x)\frac{\partial^2 w}{\partial x^2} + 2\rho_a V_x \frac{\partial^2 w}{\partial x \partial t} + \rho_a \frac{\partial^2 w}{\partial t^2} = p(x,t) - P_a - P_{BW} \qquad (6.2)$$

where, D is the bending rigidity (see Table 2.1), w is the displacement perpendicular to tape's surface, x is the longitudinal spatial coordinate, ρ_a is areal mass density, T_x is the externally applied tension per unit width. The shell stifness, K, and the belt wrap pressure, P_{BW}, are defined in Equations (2.43, 2.44).

The two media are coupled through the gap height, h, as follows:

$$h(x,t) = w(x,t) + \delta(x) \qquad (6.3)$$

See Section 2.3 for the definition of the tape geometry.

6.3 Boundary Conditions and Initial Conditions

The tape is assumed to be "simply supported" at the guide pins located at $(\bar{X}, \bar{Y}) = (0,0)$ and $(\bar{X}, \bar{Y}) = (0, L)$ as shown in Figure 2-3. Granzow and Lebeck showed that moving these supports to the edges of the guide does not affect the steady state solution of the problem [24]. We follow their choice of location, but keep the simple support conditions as opposed to their fixed end conditions. In this case, the boundary conditions given by Equations (2.36,2.37) become,

$$\begin{aligned} w(0,t) = w_L \quad w(0,t)_{,xx} = 0 \\ w(L_x,t) = w_R \quad w(L_x,t)_{,xx} = 0 \end{aligned} \qquad (6.4)$$

where, w_L and w_R are the displacements that the left and right supports experience when the tape is displaced by an amount h_o in the wrap region. See "Detail A" in Figure 2-3. The boundary condition for the Reynolds equation is as follows:

$$p = P_a \quad \text{at } s = 0, L_s \tag{6.5}$$

The initial conditions for the tape are given as follows:

$$w(x,0) = w_o \tag{6.6}$$

$$\frac{d}{dt}(w(x,0)) = 0 \tag{6.7}$$

The initial displacement w_o is defined by using Equation (6.3) and the foil bearing height, h_o, obtained from the perfectly flexible, infinitely wide, incompressible foil bearing theory [27],

$$h_o = 0.643R(\frac{6\mu_a V_x}{T_x})^{2/3} \tag{6.8}$$

This is applied between L_{x1} and L_{x2}. Outside this region the tape is connected to the far edge simple supports with straight lines. The initial pressure distribution is denoted by P_o, and it is given by,

$$P_o = \begin{cases} 0, & 0 \le s \le L_{s1} \\ \frac{T_x}{R}, & L_{s1} \le s \le L_{s2} \\ 0, & L_{s2} \le s \le L_s \end{cases} \tag{6.9}$$

See Figure 2-3 for the locations of L_{s1}, L_{s2} and L_s.

6.4 Solution Method

The tape equation and the Reynolds equation are solved by using the finite difference technique. We modified the method used by Stahl et al. [58] to include the shell stiffness and belt wrap pressure. We also allowed non-uniform spacing in the finite difference mesh for the Reynolds equation. The discretized forms of the equations involved are given in the following sections.

6.4.1 Discretization of the Tape Equation

The tape equation is discretized by using central finite difference formulas as Stahl et al. The system of equations turn out to be,

$$dw_{i+2}^{j+1} + cw_{i+1}^{j+1} + bw_i^{j+1} + aw_{i-1}^{j+1} + dw_{i-2}^{j+1} = f_i^{j+1} \tag{6.10}$$

where, the superscript on w refers to the time step, and the subscripts refer to the spatial node numbers. The coefficients appearing in the above equation are time invariant and they are given as follows:

$$a = -\frac{4D}{\Delta x^4} + \frac{\rho_a V_x^2 - T_x}{\Delta x^2} - \frac{\rho_a V_x}{\Delta t \Delta x} \tag{6.11}$$

$$b = \frac{6D}{\Delta x^4} - 2\frac{\rho_a V_x^2 - T_x}{\Delta x^2} + \frac{\rho_a}{\Delta t^2} + K_i \tag{6.12}$$

$$c = -\frac{4D}{\Delta x^4} + \frac{\rho_a V_x^2 - T_x}{\Delta x^2} + \frac{\rho_a V_x}{\Delta t \Delta x} \tag{6.13}$$

$$d = \frac{D}{\Delta x^4} \tag{6.14}$$

where, $\Delta x = \frac{L_x}{N_t - 1}$ is the spatial node spacing. L_x is the total tape length between the guides as shown in Figure 2-3. The time step size is $\Delta t = \frac{\tau}{N_T}$. In this definition τ is the total duration of simulated motion, N_T is the number of time steps, and N_t is the number of spatial nodes. The right hand side of Equation (6.10) consists of the currently applied force, P_i^{j+1}, displacements from the previous time steps, and a time invariant force, f_{BC_i}, which arises from the treatment of boundary conditions in Equation (6.4),

$$f_i^{j+1} = P_i^{j+1} - \frac{\rho_a}{\Delta t^2}(w_i^{j-1} - 2w_i^j) - \frac{\rho_a V_x}{2\Delta t \Delta x}(w_{i-1}^{j-1} - w_{i+1}^{j-1}) + f_{BC_i} \tag{6.15}$$

K_i is defined in Equation (2.43) and P_i^{j+1} is as follows:

$$P_i^{j+1} = p_i^{j+1} - Pa - P_{BW} \tag{6.16}$$

where, P_{BW} is the belt wrap pressure given by Equation (2.44). The time invariant force, f_{BC_i}, is as follows:

$$f_{BC_i} = \begin{cases} -(a+2d)w_L & i = 1 \\ -dw_L & i = 2 \\ 0 & 3 \leq i \leq N_{t-3} \\ -dw_R & i = N_{t-2} \\ -(a+2d)w_R & i = N_{t-1} \end{cases} \tag{6.17}$$

Combining the discretized boundary conditions (6.4-b) and (6.4-d) with Equation (6.10) for nodes $1, 2, N_{t-2}$ and N_{t-1} the system of equations can be put into the following matrix equation,

$$[K]\{w^{j+1}\} = \{f^{j+1}\} \tag{6.18}$$

As $[K]$ is independent of time, this equation is factorized by using the LU decomposition, [56], once, before the time integration is started. Then, the displacements for the next time step $\{w^{j+1}\}$ are obtained by the matrix multiplication of the factorized $[K]$ with $\{f^{j+1}\}$.

6.4.2 Discretization of the Reynolds Equation

The method of linearization of the Reynolds equation is as described by Stahl et al. [58]. However, as the discretized spatial coordinates for the Reynolds equation are not equally spaced, the regular central finite difference formulas are replaced by the following,

$$p_{,x} \approx \quad Ap_{i-1} + Bp_i + Cp_{i+1} \tag{6.19}$$

$$p_{,xx} \approx \quad 2[\tfrac{p_{i-1}}{D2X0} + \tfrac{p_i}{D2X1} + \tfrac{p_{i+1}}{D2X2}] \tag{6.20}$$

$$h_{,x} \approx \quad Ah_{i-1} + Bh_i + Ch_{i+1} \tag{6.21}$$

$$h_t \approx \quad \tfrac{h_i^j - h_i^{j-1}}{\Delta t} \tag{6.22}$$

$$p_t \approx \quad \tfrac{p_i^{j+1} - p_i^j}{\Delta t} \tag{6.23}$$

where, A, B and C are

$$A = \quad \tfrac{1}{D2X0}(s_i - s_{i+1}) \tag{6.24}$$

$$B = \frac{1}{D2X1}(2s_i - s_{i+1} - s_{i-1}) \tag{6.25}$$

$$C = \frac{1}{D2X2}(s_i - s_{i-1}) \tag{6.26}$$

and,

$$D2X0 = (s_i - s_{i-1})(s_{i+1} - s_{i-1}) \tag{6.27}$$

$$D2X1 = (s_i - s_{i-1})(s_i - s_{i+1}) \tag{6.28}$$

$$D2X2 = (s_{i+1} - s_i)(s_{i+1} - s_{i-1}) \tag{6.29}$$

The Reynolds equation is discretized by substitution of the above equations into (6.1). The linearization is achieved by replacing p^{j+1} with p^j in the terms that have products of p and its derivatives. With these substitutions the Reynolds equation reduces to the following set of linear equations,

$$\alpha p_{i-1}^{j+1} + \beta p_i^{j+1} + \chi p_{i+1}^{j+1} = G_i^{j+1} \tag{6.30}$$

At the entry and exit boundaries where the pressure is ambient Equation (6.30) becomes,

$$\beta p_i^{j+1} + \chi p_{i+1}^{j+1} = G_i^{j+1} - \alpha P_a, \quad \text{at } s = 0 \tag{6.31}$$

$$\alpha p_{i-1}^{j+1} + \beta p_i^{j+1} = G_i^{j+1} - \alpha P_a, \quad \text{at } s = L_s \tag{6.32}$$

This system of equations can be put in a matrix form,

$$[S]\{p^{j+1}\} = \{G^{j+1}\} \tag{6.33}$$

The matrix $[S]$ is populated only on the main diagonal and the adjacent upper and lower diagonals. This system of equations can, therefore, be solved by using the three diagonal matrix algorithm [56].

The coefficients appearing in Equation (6.30) are given as follows:

$$\alpha = (h_i^j)^2[A(3p_i^j(Ah_{i-1}^j + Bh_i^j + Ch_{i+1}^j) + h_i^j(Ap_{i-1}^j + Bp_i^j + Cp_{i+1}^j)) + \frac{2}{D2X0}(p_i^j h_i^j + 6\lambda_a p_a)] + 6Ah_i^j[2\lambda_a p_a(Ah_{i-1}^j + Bh_i^j + Ch_{i+1}^j) - \mu_a V_x] \tag{6.34}$$

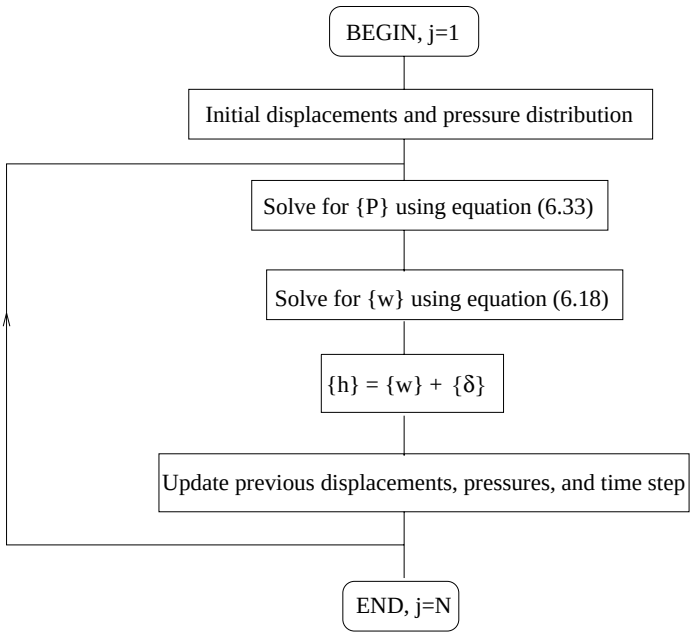

Figure 6-1: The time stepping algorithm for the foil bearing problem as given by Stahl et al.

$$\beta = (h_i^j)^2[B(3p_i^j(Ah_{i-1}^j + Bh_i^j + Ch_{i+1}^j) + h_i^j(Ap_{i-1}^j + Bp_i^j + Cp_{i+1}^j)) + \frac{2}{D2X1}(p_i^j h_i^j + 6\lambda_a P_a)] + 6Bh_i^j[2\lambda_a P_a(Ah_{i-1}^j + Bh_i^j + Ch_{i+1}^j) - \mu_a V_x] - 6\mu_a V(Ah_{i-1}^j + Bh_i^j + Ch_{i+1}^j) - \frac{12\mu_a h_i^j}{\Delta t} - 12\mu_a \frac{h_i^j - h_i^{j-1}}{\Delta t} \quad (6.35)$$

$$\chi = (h_i^j)^2[C(3p_i^j(Ah_{i-1}^j + Bh_i^j + Ch_{i+1}^j) + h_i^j(Ap_{i-1}^j + Bp_i^j + Cp_{i+1}^j)) + \frac{2}{D2X2}(p_i^j h_i^j + 6\lambda_a P_a)] + 6Ch_i^j[2\lambda_a P_a(Ah_{i-1}^j + Bh_i^j + Ch_{i+1}^j) - \mu_a V_x] \quad (6.36)$$

$$G_i^{j+1} = -\frac{12\mu_a}{\Delta t} h_i^j p_i^j \quad (6.37)$$

6.4.3 The Solution Algorithm

The system is coupled by solving the Reynolds equation, (6.33), with h^j and P^j known from the previous time step. The pressure distribution obtained is used to calculate the corresponding tape displacement from Equation (6.18). Using this displacement the foil bearing height, h^{j+1} is calculated, displacements of the previous time steps are updated and a new pressure calculation is started. This process, summarized in Figure 6-1, is repeated until the last time step, N_T.

6.5 Convergence Studies

In this section the effects of time step size, Δt and spatial step size, Δx, on the steady state tape flying height are presented. The case studied is given by Stahl et al. [58]. The specifications of this case are listed in Table 6.1. This geometry has been used in many studies as a bench mark test problem [1, 2, 24, 29, 30].

> *In this simulation the location where the flat part of the tape connects to the curved part requires special attention. We found that a node should be placed at the junction point, $x = L_{x1}$, when the tape is discretized. Discretization schemes that do not satisfy this restriction show problematic convergence characteristics.*

The effect of time step size and the spatial step size on the convergence of the problem is shown in Figure 6-2. The convergence study was done by running the simulation with different Δt and Δx values for $\tau = 0.0115s$[3]. We compared the steady state flying height, $h_{ss} = h(\frac{L_x}{2}, t_N)$, for the convergence study, as we changed Δx and Δt.

The time step size was chosen from the following range, $0.25 \leq \Delta t \leq 1.25\mu s$. In our study, convergence was unsatisfactory for Δt values that are greater than $1.25\mu s$. For the other Δt values $(0.25, 0.5, 0.75, 1.0, \mu s)$ the convergence curves are almost identical as can be seen from Figure 6-2.

[3]This is the time required for the tape to travel twice the bearing region's length as suggested by Eshel [17].

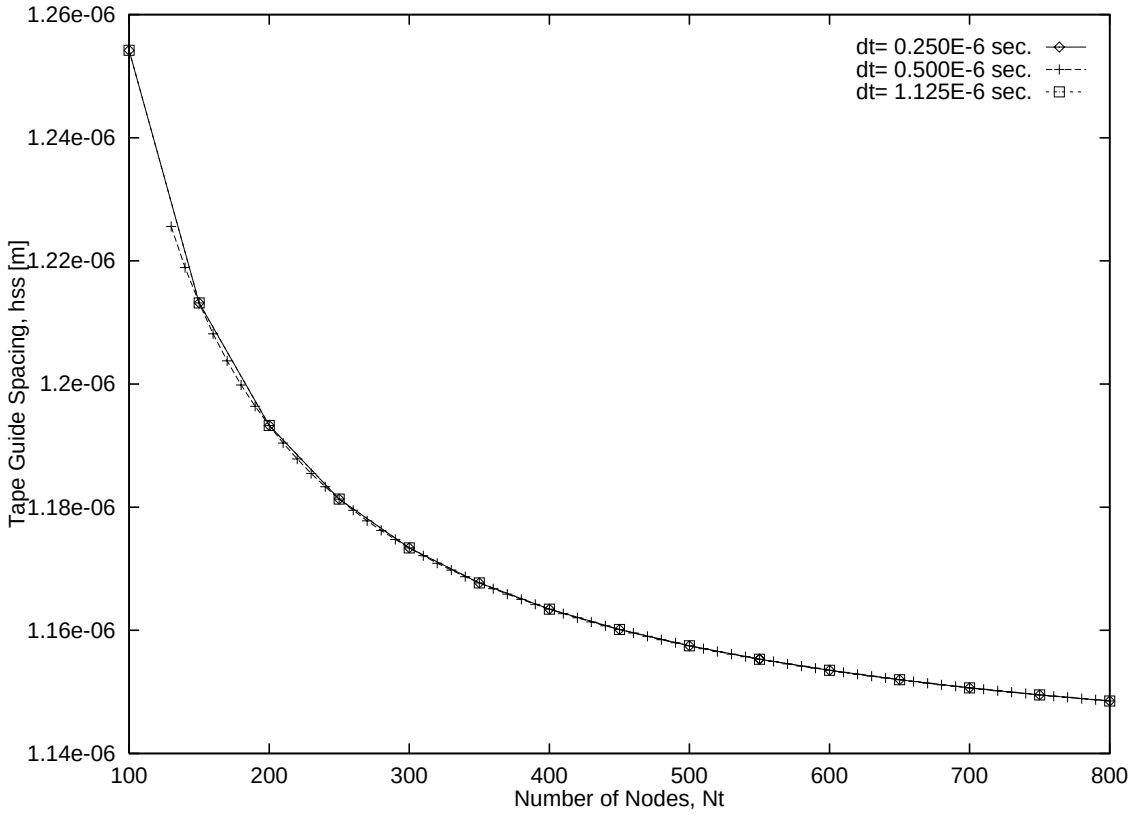

Figure 6-2: Convergence study for $20\mu m$ thick tape, as a function of Δt and Δx. Plotted are the results of the program for $\Delta t = 0.25, 0.5, 1.125\mu s$ for a range of node numbers. The $0.5\mu s$ case was run with 5, and the other two cases were run with 50 node number increments.

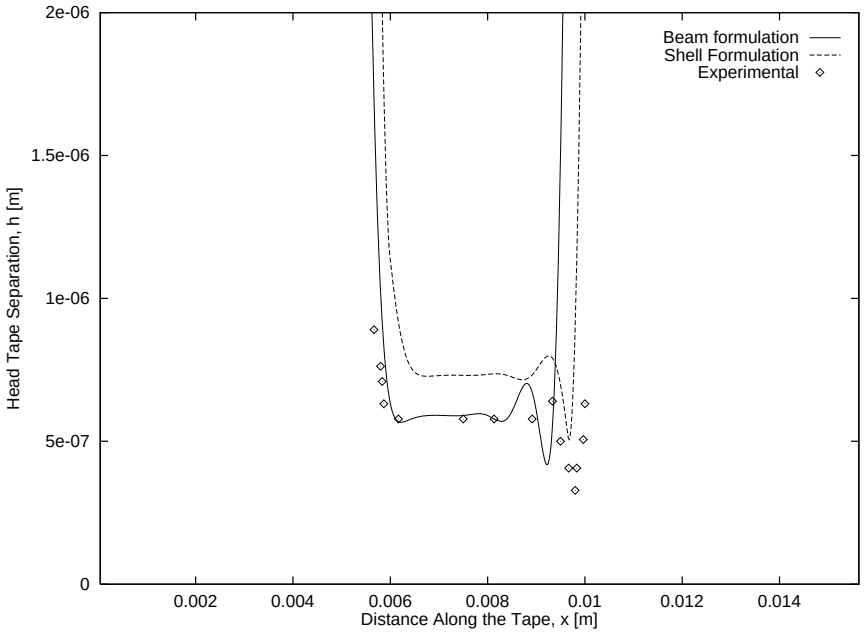

Figure 6-3: Comparing the flying heights for the experimental case from Vogel and Groom with the two approaches to the foil bearing problem. The offset is due to the definition of x-coordinate.

The spatial step size, Δx, has a more pronounced effect on h_{ss} than the time step size. The convergence to the steady state flying height as a function of number of nodes is a smoothly varying curve. Increasing the number of spatial nodes, N_t, clearly improves the convergence. For this example problem Figure 6-2 shows that between the two extremes of the number of nodes, 100 and 800, the predicted steady state flying height changes roughly 15%. Plotting the h_{ss} as a function of $\Delta x = L_x/(N_t - 1)$ as shown in Figure 6-6 shows that the convergence is almost linear. In fact, by extrapolating the lines shown on this figure we can get the solutions that the algorithm would predict for an infinite number of nodes.

6.6 Results and Conclusions

In order to check the validity of the model, the geometry from Vogel and Groom [67]

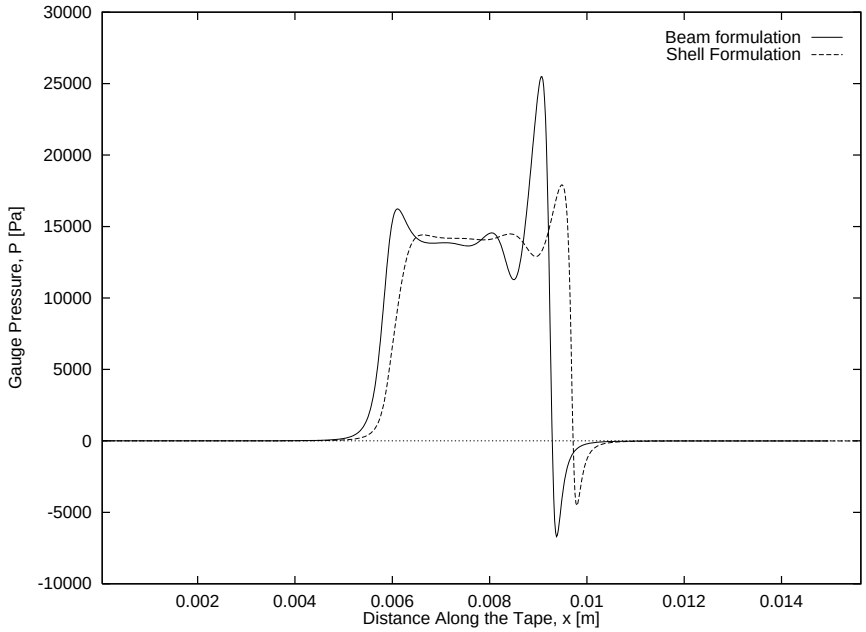

Figure 6-4: Comparison of the air pressure at steady state for the Vogel and Groom's geometry. The offset is due to the definition of x-coordinate.

is analyzed using the new approach[4]. Vogel and Groom's study is published together with Stahl et al.'s, [58], and contains experimental verification of the numerical method used in that study. We also recreated the solution algorithm of Stahl et al. Our approach is compared to the results of Stahl et al.'s approach, in Figures 6-3 and 6-4. The specifications of the problem are given in Table 6.2. Even though, our approach simulates the tape's behavior at the entry and exit zones better than Stahl et al.'s approach it converged to a roughly 20% higher steady state spacing in the constant gap region compared to the experimental values. The pressure values corresponding to this steady state are given in Figure 6-4. This figure shows that the pressure converges to a slightly higher value in our approach. It also shows that the spikes predicted at the entry and exit zones by the beam formulation of Stahl et al. are smoother in our approach.

The effect of tape thickness on the steady state flying height of the Stahl et al.'s

[4]We couldn't make direct comparisons with the Stahl et al.'s study because the tape thickness, c, is not reported in that work.

N_t	Number of nodes for tape	100,150, ... ,800	
N_P	Number of nodes for air bearing	$N_t - 2$	
Δt	Time step	0.25,0.5,0.75,1,1.125,1.25	μs
ρ_a/c	Volumetric mass density of the tape	1400	kg/m^3
V	Speed of the tape	2.54	m/s
T	Tension in the tape	277	N/m
E	Young's modulus of the tape	4.0	GPa
ν	Poisson's ratio	0.3	
c	Tape thickness	5,10,20,34.62	μm
R	Radius of the Guide	2.04	cm
L_x	Distance between far end supports	8.44	cm
θ_L	LHS wrap angle	8.89°	
θ_R	RHS wrap angle	8.89°	
θ_{e1}	LHS entry angle	12°	
θ_{e2}	RHS exit angle	12°	
P_a	Ambient pressure	84.1	kPa
μ_a	Viscosity of air	1.81×10^{-5}	$N/m^2 s$
λ_a	Mean free path lenght of air	0.0635	μm

Table 6.1: Specifications for example problem for the Stahl et al.case.

geometry and parameters as function of node numbers, N_t are given in Figures 6-5 and 6-6. We see that the convergence trend is similar for all of the tape thickness values considered, $c = 5, 10, 20$, and $34.6 \mu m$. We also note that thinner tapes tend to settle to lower flying heights. In Figure 6-6 we plot the steady state gap height as a function of spatial step size, Δx. This shows us that the convergence to the steady state flying height is almost a linear function of Δx. We can obtain the steady state flying height for $\Delta x \to 0$ by extrapolating the lines given in Figure 6-6.

The slightly higher pressure that can be seen in Figure 6-4, in the constant gap zone, is the result of higher flying height predicted by our approach. However, we can not explain why the pressure is higher in our approach. In the next chapter, we use the tape displacement and air pressure values at the steady state obtained from the 1D study as the intial conditions for reaching the steady state for the 2D problem.

N_t	Number of nodes for tape	800	
N_P	Number of nodes for air bearing	$N_t - 2$	
Δt	Time step size	0.5	$\mu_a s$
V_x	Speed of the tape	1.27	m/s
T_x	Tension in the tape	276.7	N/m
c	Tape thickness	38.1	$\mu_a m$
E	Young's modulus	4.0	GPa
ρ_a/c	Volumetric mass density of the tape	1400	kg/m^3
ν	Poisson's ratio	0.35	
R	Radius of the Guide	2.0	cm
θ_L	Wrap angle (See Fig.5)	5.2995°	
θ_R	Wrap angle	5.2295°	
θ_{e1}	Entry angle	16.7248°	
θ_{e2}	Exit angle	16.7248°	
L_x	Distance between far end supports	8.44	cm
P_a	Ambient pressure	1.013	kPa
μ_a	Viscosity of air	1.81×10^{-5}	$N/m^2 s$
λ_a	Mean free path lenght of air	0.0635	$\mu_a m$

Table 6.2: Specifications of the test case for Vogel and Groom.

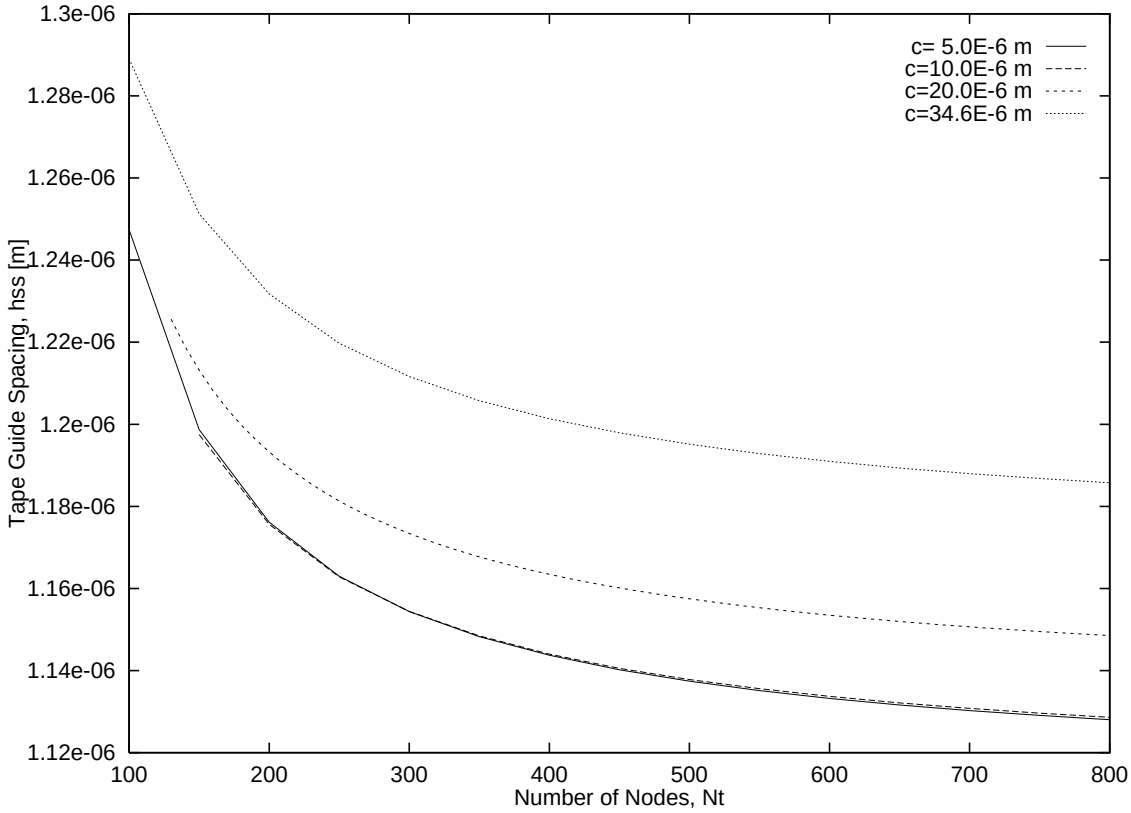

Figure 6-5: Comparison of the steady state foil bearing heights for different tape thicknesses as a function of number of nodes, N_t, used to solve the problem.

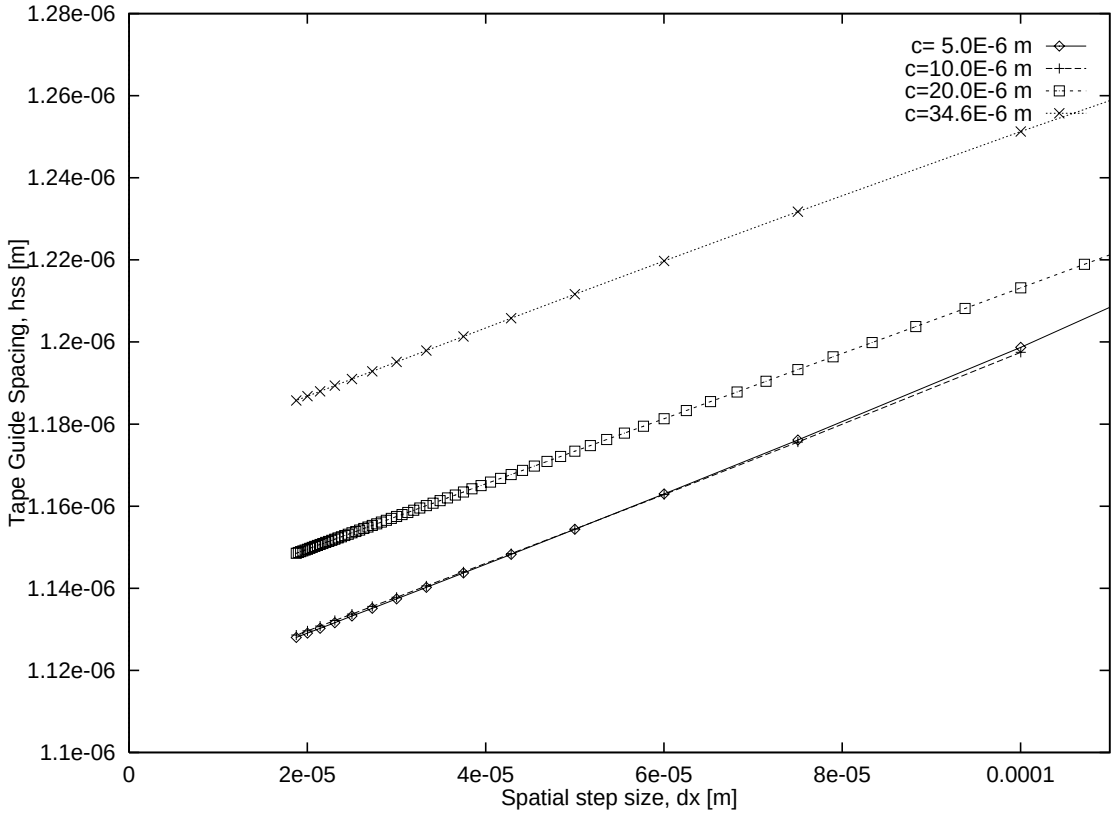

Figure 6-6: Comparison of the steady state foil bearing heights for different tape thicknesses as a function of spatial step size, Δx. Note that extrapolation of the curve gives a better estimate of the steady state gap height. This corresponds to $\Delta x \to 0$ solution.

Chapter 7

The 2D Foil Bearing Problem

7.1 Introduction

In this chapter we present the results of our model for the finite width (2D) foil bearing problem. There are several reasons to study this problem. Imperfections in a tape system's parameters, such as axial tension variations, cause cross-width asymmetry in the tape. In linear recording, increasing demands on increasing the bit density will eventually necessitate the use of unused bands on the sides of the tape. These bands can not be modeled by a 1D analysis. Continuing trends to use smaller form factors in recording will show the emergence of narrower tapes for linear recording. However, as the tape is made narrower the displacement boundary layers on the free edges of the tape merge[1]. This can not be modeled by a 1D analysis, either. In helical scan recording there is no longitudinal symmetry, therefore, the analysis of this type of recording should consider the width effects. These factors motivated the study presented in this chapter.

In modeling the finite width foil bearing problem, investigators who published on this field use varying formulations. The two major assumptions used by some investigators are the incompressibility of air, and/or leaving the high Knudsen number effects out of the analysis. For flying heights that are in the order of $0.5\mu m$ or less the compressibility

[1]See [22] for more on the displacement boundaries layers in thin bent plates.

of air is important. Also in this region the effects of molecular rarefaction of air becomes important. Therefore, these effects are kept in our study.

The tape models have been subject to more variations. Some studies, [4, 29, 39, 47, 57, 72], consider only the out-of-plane displacement, w, in the derivation of the equation of equilibrium, whereas others, [21, 25, 36, 73], consider also the in-plane displacements u and v. Except for [72], all of these studies consider the bending stiffness of the tape. The orthotropy of the tape is considered by [47]. In establishing strain-displacement relations some investigators use linear relationships [4, 25, 47, 36] and others consider the non-linear terms [21, 57]. The linear strain-displacement assumption is suitable for modeling longitudinal recording, whereas non-linear strain-displacement relations and in-plane displacements should be employed in modeling helical scan recording where the head penetration causes large rotations, and friction forces cause in-plane loading. The selection of the equation of motion of the tape in this thesis is made from a practical point of view. We use a linear, uncoupled tape model, (2.34), because compared to other models, it is less time consuming to solve this equation on the computer in a transient solution. Nonlinear tape models can be incorporated into the time algorithm given in Chapter 2, with a cost of increased simulation time.

The underlying equations, (2.34) (2.58) and (2.64), for our model are derived in Chapter 2. The numerical methods used to solve these equations, are given in Sections 3.2 and 3.5, and the transient coupling algorithm is given in Section 3.6. In the following we review the governing equations. Then, we present the boundary layers that occur in the air flow, and their effects on the solution of the problem[2]. In Section 7.3 we present the results of several case studies in which we demonstrate the effects of axial variations of several problem parameters on the steady state tape-guide spacing. In Section 7.4 we give the results of the simulations in the transient domain for linear and helical-scan recording applications.

[2]Please note that we also mention a boundary layer effect on the tape. The two are related but one of them is not the only cause of the other.

7.2 Problem Formulation

The governing equation of motion for the out-of-plane displacements, w, of a thin elastic tape with thickness, c, and bending stiffness, D, is given as follows:

$$D\nabla^4 w + Kw - T_x\frac{\partial^2 w}{\partial x^2} + \rho_a(V_x^2\frac{\partial^2 w}{\partial x^2} + 2V_x\frac{\partial^2 w}{\partial x \partial t} + \frac{\partial^2 w}{\partial t^2}) = p + P_c - P_a - P_{BW} \quad (7.1)$$

In this equation x is the circumferential direction, y is the axial direction, and t is time. The shell stiffness, K, and the belt wrap pressure, P_{BW}, take different values on different locations of the tape,

$$K = \begin{cases} 0, & 0 \le x \le L_{x1} \\ \frac{Ec}{R^2(1-\nu^2)}, & L_{x1} \le x \le L_{x2} \\ 0, & L_{x2} \le x \le L_x \end{cases} \quad (7.2)$$

$$P_{BW} = \begin{cases} 0, & 0 \le x \le L_{x1} \\ \frac{T_x}{R}, & L_{x1} \le x \le L_{x2} \\ 0, & L_{x2} \le x \le L_x \end{cases} \quad (7.3)$$

The tape fallows the curvature of the guide only where, $L_{x1} \le x \le L_{x2}$. The tape lengths L_{x1} and L_{x2} mark the locations of connections between the flat and curved regions of the tape as shown in Figure 2-3. In Equation (7.1) the tape is assumed to be under tension, T_x, and moving longitudinally with speed V_x. The loading on the tape is provided by the air pressure, $p - P_a$, the contact pressure, P_c, and the belt wrap pressure. Ambient pressure is P_a. The contact pressure is defined in Section 2.6. The boundary conditions and the initial conditions for the tape equation are as follows:

Simply Supported Sides:

$$M_x = D[\frac{\partial^2 w}{\partial x^2} + \nu\frac{\partial^2 w}{\partial y^2}] = 0 \qquad x = 0, L_x, \text{ and } 0 \le y \le L_y \quad (7.4)$$

$$w = 0 \qquad x = 0, L_x, \text{ and } 0 \le y \le L_y \quad (7.5)$$

Free Edges :

$$M_y = D[\frac{\partial^2 w}{\partial y^2} + \nu\frac{\partial^2 w}{\partial x^2}] = 0, \qquad \text{at } y = 0, L_y, \text{ and } 0 \le x \le L_x \quad (7.6)$$

$$Q_y^{eq} = D[\frac{\partial^3 w}{\partial y^3} + (2-\nu)\frac{\partial^3 w}{\partial x^2 y}] = 0, \qquad \text{at } y = 0, L_y, \text{ and } 0 \le x \le L_x \quad (7.7)$$

where, M_x, M_y and Q_y^{eq} are the bending moment resultants in x and y directions and the equivalent shear force resultant in the y direction, respectively. The length of the tape between the supports, as described in Section 6.3, is L_x and the width of the tape is L_y.

Initial Conditions :

$$\text{Initial displacement,} \qquad w(x,y,0) = w^o(x,y) \tag{7.8}$$

$$\text{Initial displacement velocity,} \qquad \frac{\partial w(x,y,0)}{\partial t} = v^o(x,y) \tag{7.9}$$

The initial condition, w^o, v^o, are defined below by Equations (7.24) and (7.25).

The air lubrication is modeled by using the modified Reynolds equation,

$$\begin{aligned} \frac{\partial}{\partial s}[h^3 p \frac{\partial p}{\partial s}(1 + 6\frac{\lambda_a}{h})] \quad + \quad & \frac{\partial}{\partial y}[h^3 p \frac{\partial p}{\partial y}(1 + 6\frac{\lambda_a}{h})] = \\ & 12\mu_a \frac{\partial ph}{\partial t} + 6\mu_a (V_x + V_x^G)\frac{\partial ph}{\partial s} + 6\mu_a (V_y + V_y^G)\frac{\partial ph}{\partial y} \end{aligned} \tag{7.10}$$

where, p, is the air pressure, h, is the tape guide separation, λ_a, is the molecular mean free path length of air, μ_a is the viscosity of air and s is the spatial coordinate on the guide surface in the circumferential direction. Tape velocity components are denoted by V_x and V_y and the guide velocity components are denoted by V_x^G and V_y^G. The boundary conditions for the Reynolds equation are,

$$p(0,y) = p(L_x,y) = p(x,0) = p(x,L_y) = P_a \tag{7.11}$$

The initial condition for the Reynolds equation is,

$$p(x,y,0) = p_o \tag{7.12}$$

where, p_o is given below by Equation (7.26).

The tape guide separation, h, couples the equations governing the two media,

$$h(x,y,t) = w(x,y,t) + \delta(x,y) \tag{7.13}$$

The guide shape is defined by a function, $\delta(x,y)$. The x-direction definition of this function is identical to the definition in Equation (2.45). See Figure 2-3. In the 2D foil bearing problem we allow for variation on the guide surface in the axial direction,

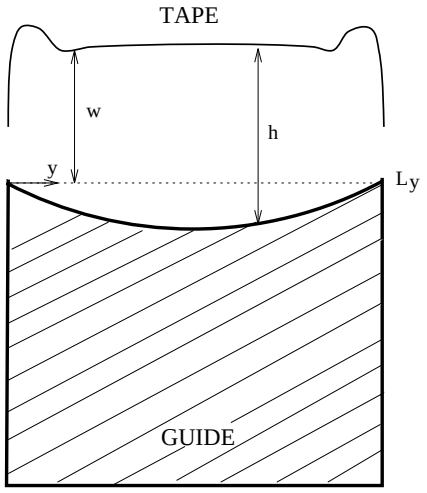

Figure 7-1: The guide shape in the y (axial) direction. Note that the shape variation may be due to production tolerances or a deliberate design preference.

as shown Figure 7-1[3]. However, unless otherwise stated all of the cases studied in this thesis assume a *flat* guide surface, without any axial variation.

7.2.1 The Pressure Boundary Layers

The side flow of air in a foil bearing is confined to a narrow band on the sides of the bearing. In the middle part of the tape air flow is in the direction of the tape velocity, and the pressure distribution is similar to that of an infinitely wide bearing. At the two free edges of the tape, the side flow is significant, and the air pressure drops from its value in the middle to the ambient pressure in a narrow boundary layer.

We are not aware of any study which predicts the side boundary layer width for a foil bearing. However, for a slider bearing asymptotic studies show that the side boundary layer width is,

$$W_{side} \propto \Lambda^{-1/2} \tag{7.14}$$

[3]See Section 7.3.

where, the *bearing number* is defined as follows:

$$\Lambda = \frac{6\mu V_x L_y}{h_m^2 P_a} \tag{7.15}$$

In this equation, h_m is the minimum bearing clearance. Similarly, at the trailing edge (exit side) of a slider bearing the pressure drops to ambient value within a boundary layer width, W_{exit}, proportional to Λ^{-1} [27, page 172]. However, for an infinitely wide, perfectly flexible, and incompressible foil bearing an estimate for W_{exit} exists. This estimate shows that,

$$W_{exit} \propto h_o(T_x/(6\mu V_x))^{1/3} \tag{7.16}$$

[27, chapter 6], where h_o is the foil bearing height in the constant gap region.

In any case these relations suggest that for higher tape speeds, V_x, the boundary layers are expected to be narrower. In the next section we elaborate on the effects of narrow boundary layers on the numerical solution of the problem.

7.2.2 Interpolation

As shown in Chapter 4, the accuracy of the tape equation depends on the the spatial mesh size, Δ, and as noted by Hughes, on the time integration scheme that one uses [34]. Similar claims can be made for the solution of the Reynolds equation [16]. In the previous section we mentioned that narrow boundary layers form on the lateral edges and the exit side of the foil bearing. In order to adequately resolve the pressure changes, using a discretized solution method, one needs to place a large number of nodes in these boundary layers. However, using the same nodal spacing in the boundary layer regions, and the other parts of the pressure solution domain, as well as in the tape mesh is computationally inefficient. For this reason we wrote our simulation to handle varying mesh sizes in the tape and Reynolds equation domains. This situation requires interpolation of the variables from one mesh type to the other.

As the meshes used in both domains are rectangular we borrowed an interpolation idea used extensively by a distant cousin of the finite difference method; the finite element

method. We used the interpolation provided by the isoparametric bilinear elements to interpolate a function on a four-noded rectangular element. Knowing the values of a variable P at the four corners of a rectangle, its values anywhere inside the rectangle can be interpolated by,

$$P(\xi,\eta) = \sum_{i=1}^{4} N_i P_i \tag{7.17}$$

where, P_i are the known values of the variable at the four corners. See Figure 7-2. The *shape functions*, N_i, are given as follows:

$$N_1 = (1-\xi)(1-\eta) \tag{7.18}$$

$$N_2 = (1+\xi)(1-\eta) \tag{7.19}$$

$$N_3 = (1+\xi)(1+\eta) \tag{7.20}$$

$$N_4 = (1-\xi)(1+\eta) \tag{7.21}$$

The nondimensional coordinates of the interpolation element, ξ and η can be expressed in terms of the coordinates of the four corners, (x_i, y_i) and the coordinates of the point at which interpolation is sought, (x, y), as follows:

$$\xi = \frac{x-0.5(x_1+x_4)}{0.5(x_4-x_1)} \tag{7.22}$$

$$\eta = \frac{y-0.5(y_1+y_2)}{0.5(y_2-y_1)} \tag{7.23}$$

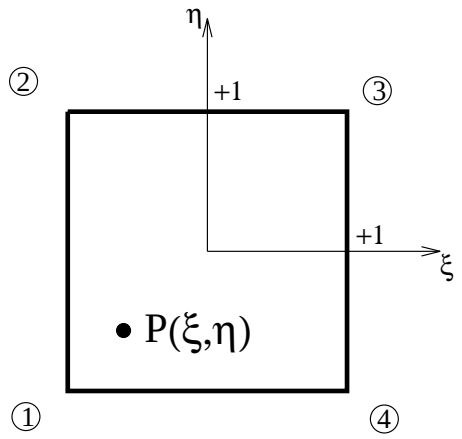

Figure 7-2: Isoparametric, bilinear interpolation element used in interpolating the variables between the pressure and tape domains.

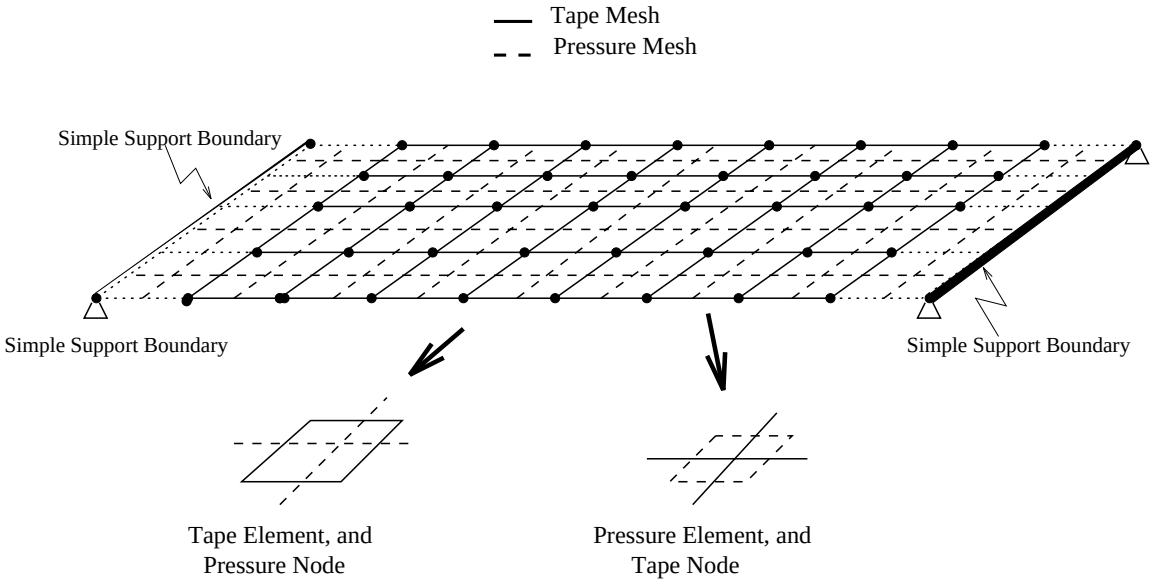

Figure 7-3: The tape and pressure solution domains, and the tape and pressure interpolation elements.

The pressures, $p(x, y, t)$, obtained from the Reynolds equation solver are interpolated to the pressures used by tape equation solver. To do this, the nodes of the pressure mesh to are grouped as fictitious four noded *pressure elements*. Then each tape node is located with respect to these elements. See Figure 7-3 for this arrangement. For each tape node we make a list establishing the tape-node-to-pressure-element relation. We, then, calculate the shape functions for that particular pressure element and that node using Equations (7.18-7.21). This information needs to be calculated only once before the time integration is started. The interpolation from the pressure domain to the tape domain is performed by applying Equation (7.17) at every node.

We also need to interpolate the tape guide spacing, $h(x, y, t)$, from the tape mesh to the pressure mesh. Note that this interpolation is in the opposite direction as the one described in the above paragraph. In this case we set up fictitious *tape elements* and proceed as before. These fictitious elements are shown in Figure 7-3.

7.3 The Steady State in Linear Recording

In order to find the steady state of a given problem we trace the transient solution to steady state while keeping its parameters constant. To reach a steady state we run the simulation for a duration of $\tau = 2\frac{L_x}{V_x}$ as suggested by Eshel's study, [17]. We also trace the mid-point tape-guide separation, $h(\frac{L_x}{2}, \frac{L_y}{2})$. The initial conditions of the 2D problem are obtained from the solution of the 1D problem,

$$w_o(x, y, 0) = \quad w_o^{1D}(x) \tag{7.24}$$

$$v_o(x, y, 0) = \quad 0 \tag{7.25}$$

$$p_o(x, y, 0) = \quad P_a + (p_o^{1D}(x) - P_a)\frac{4}{L_y}(y - \frac{y^2}{L_y}) \tag{7.26}$$

where, $w_o^{1D}(x)$ denotes the displacement distribution, and $p_o^{1D}(x)$ denotes pressure distribution of the 1D problem at the steady state. In Equation (7.26) we impose a parabolic variation in the y-direction onto the pressure solution of the 1D problem. Unless we make the pressure variation smoother as described here, initially, the pressure gradient

on the side boundaries becomes unrealistically large. In fact, the algorithm will not run successfully without this type of initialization. We also note that the displacement distribution given by Equation (7.24) is unequilibriated[4], because of the nature of the moment boundary condition, (2.38), on the free edges of the tape. For the linear recording problem the only non-zero velocity component that is used for the Reynolds equation solution is the tape transport speed, V_x.

In Figure 7-5 we show the "snapshots" of the gap height and pressure distribution at the initial stages of the simulation. The parameters for this simulation are given in Table 7.4. The frames marked as $t = 0$ denote the initial conditions of the gap height, h, and the air pressure, p, that are given by Equations (7.24) and (7.26). Since the free edges of the tape are exposed to the atmosphere, air pressure does not support the tape at these edges at any time. This situation, combined with the effect of tape's initial flat displacement causes the free edges of the tape to "drop" as shown in Figure 7-5. As these edges drop to lower flying heights, the air reacts by rapidly increasing the pressure at this region. See frames marked $t = 2$ and $4\mu s$ in Figure 7-5. The wave action, seen in this figure, in the pressure and tape domains are primarily caused by the initial conditions and are not physical. Most of the higher harmonics are damped out by the time, $t = 300\mu s$, however the steady state in tape displacement is not observed before $t = 2ms$.

The conditions of the tape guide spacing, h, the air pressure p, and the contact pressure, P_c at the steady state are presented in Figure 7-6. As expected, we notice that the contact pressure at the free edges of the tape are non-zero, supporting our earlier claim that air pressure does not support the tape here. This figure agrees well with the results of Heinrich and Conelly [29], except for the contact pressure which is not mentioned in that study . The minimum displacement occurs on the free edges of the exit side of the tape. The presence of this high contact pressure makes the sides of a guide most vulnerable locations for wear. The air pressure is, in general higher, close to the

[4]In the case of a thin shell wrapped around a cylindrical surface, the only way to obtain a perfectly flat surface in the thin shell, as shown in $t = 0$ of Figure 7-5, would be to apply moments, on the $y = 0$ and $y = L_y$ sides of the shell.

free edges of the tape due to lower tape gap there. In the exit side air pressure boundary layer, the air pressure dips below ambient, and it shows spikes at the free edges, where the maximum and minimum pressures are located near each other. Mixing of the side and exit pressure boundary layers cause the spikes in the pressure.

7.3.1 Tape Width Effects in Linear Recording

In this section we study the effect of tape width on the steady state tape guide spacing, h. The widths considered are, $L_y = 2, 4, 8$ and $12mm$. Other tape parameters are as indicated in the respective figure captions, and can be found in Tables 7.3 or 7.4.

The first picture of Figure 7-6 shows the cross section of the tape guide spacing, h, and air pressure, p, in the axial direction at $x = L_x/2$ for a $6.35mm$ wide tape. We observe, from this figure that the tape displacement boundary layers near the lateral edges of the tape cover nearly half of the total tape width, $L_y = 6.35mm$. The pressure boundary layers are slightly narrower compared to the displacement boundary layers, but they are comparable. We also note that the minimum tape displacement is close to the tape roughness value that we used, $\sigma_t = 93.4nm$.

The effects of some other tape widths, $L_y = 2, 4, 8, 12mm$, on the cross-tape displacement of the tape in steady state are shown in Figure 7-7. For the $2mm$ wide tape, the displacement boundary layers are mixed, and the constant gap region in the width direction is lost. This is better observed in the cross sectional views given in Figures 7-8 and 7-10. Looking at the $4mm$ wide tape, we see, in Figures 7-7 and 7-10, that the displacement boundary layers are almost separated. For wider tapes, $L_y = 6.35mm$ in Figure 7-6, and $L_y = 8$ and $12mm$ in Figures 7-7 - 7-10, we see a bigger cross-tape constant gap region. Close inspection of Figure 7-8 shows that the width of the displacement boundary layer at the sides of the tape is independent of the total tape width, except for the $2mm$ case where the two boundary layers are mixed. The width of this displacement boundary layer is approximately $2.5mm$.

Figures 7-9 and 7-11 show the effect of the tape width on the steady state air pressure

profiles. Similar observations are made about these pressure boundary layers. From these figures we conclude that a distinction should be made between the narrow and wide tapes because the results obtained for a narrow tape, $L_y < 5mm$, would not adequately represent the results for a wide one.

These results also lead to question the effect of the side air leakage on the steady state flying height. In the previous studies it was expected that the air loss from the sides of the tape would cause a lower tape-guide separation [58] [67]. Heinrich and Connely reported that this, in fact, is the situation for the Stahl et al. example [29]. What we observed from our numerical experiments is that the tape guide separation is also affected by the asperity height, the tape speed, and the amount of wrap. The separation, h, shown in Figure 7-8 is for $2.54m/s$ tape speed, (Table 7.3), whereas the one in 7-10 is for $1.27m/s$, (Table 7.4). The flat lines on these figures denote the predictions of the 1D problem. For the faster tape speed, and larger wrap angle the 2D solution flies at a lower separation, whereas for the slower tape speed, and smaller wrap angle the predictions of the 1D and 2D cases are nearly the same. Adding to these the fact that the free edges of the tape are elevated by an amount equal to the surface asperity size[5], in our simulations, any conclusions about the comparison of the 1D and the 2D cases becomes vague.

7.3.2 The Effect of Axial Tension Variation

In a magnetic recording application the tape tension, T_x, is rarely uniform across the width of the tape. Among the common causes of the this non-uniformity is the imperfections in the alignment of guide pins. Another cause of non-uniform axial tension is the driving belts that are used in some tape systems.

In this section we analyze two hypothetical axial tension variation cases. In the first case the tension variation is given as follows:

$$T_x(y) = (0.6\frac{y}{L_y} + 0.7)\bar{T}_x \tag{7.27}$$

[5] $\sigma_t = 93.4nm$

where $\bar{T}_x = 276.7N/m$. This equation provides a 60% linear tension increase between the two free edges of the tape. Other parameters of the problem are as given in Table 7.4. The steady state tape guide separation, and the corresponding air pressure are shown on the left-hand-side column of Figure 7-12. As expected, we observe in this figure that the separation, h, is smaller on the high tension side of the tape. The air responds to this smaller separation by a considerable increase in the pressure at the low flying side.

The second case of tension variation is given by the following equation,

$$T_x(y) = \begin{cases} (-1.2\frac{y}{L_y} + 0.7)\bar{T}_x, & \text{for } 0 \leq y \leq \frac{L_y}{2} \\ (1.2\frac{y}{L_y} + 0.7)\bar{T}_x, & \text{for } \frac{L_y}{2} \leq y \leq L_y \end{cases} \tag{7.28}$$

where $\bar{T}_x = 276.7N/m$. This function represents 60% tension decrease between the edge of the tape and the middle of the tape, followed by an increase of the same amount from the middle to the other edge. The steady state results of this simulation are given on the right-hand-side column of Figure 7-12. As before the separation, h, is largest where the tension is lowest. The flat region in the middle of the tape is completely lost. The pressure response is also similar.

7.3.3 The Effect of Guide Surface Shape

In many tape pack systems a rigid guide is placed on the tape path to make the tape turn a corner. If the conditions of the system are right -in other words if the radius of the guide is large and/or the tape tension is low and/or the tape speed is high- the tape will experience self air lubrication and lift away from the guide surface. This effect is desirable in some tape steering applications because it reduces the driving torque requirements, but it may be regarded as entirely unsatisfactory in other applications because it makes the tape alignment difficult.

Regardless of the intended purpose of the guide, its surface is seldom perfectly straight. In this section we show the effects of four different surface shapes on the tape-guide spacing at steady state. The surface imperfection that we introduce is a sinusoidal variation in the axial direction, although other shapes can be analyzed by our approach.

	$h[\mu m]$	
$A\ [\mu m]$	Protrusion	Dent
1	0.763	0.806
3	0.725	0.854

Table 7.1: Steady state tape-guide separation values at $(L_x/2, L_y/2)$ when there is a sinusoidal dent or protrusion on the guide surface

In the presence of the surface imperfection the head tape spacing, h, definition, (7.13), becomes,

$$h(x,y,t) = w(x,y,t) + \delta(x) + A\sin(\frac{\pi y}{L_y}) \tag{7.29}$$

where, $\delta(x)$ is as given by Equation (2.45) and A is the amplitude of the function. The sign of the amplitude, A, is positive when we want to model a dent on the surface, as shown in Figure 7-1, and it is negative when we want to model a protrusion. The y direction derivatives of the Reynolds equation are evaluated on the guide surface.

In Figure 7.13 we show four tape-guide spacings at steady state. The two pictures on the left hand side column show two surface protrusions with 1 and $3\mu m$ amplitudes, and the other two pictures on the right hand side column show two cases of dented surfaces with the same amplitudes. The guide surfaces are also drawn beneath the sketches of the tapes to enable better visualization of the situation. For the parameters that we used in this analysis (Table 7.4) $A = 3\mu m$ is the biggest amplitude that can be simulated by our model. This suggests that for bigger amplitudes the support of the tape due to air bearing becomes harder. The head tape separations at $(L_x/2, L_y/2)$ are given in Table 7.1. We notice that the flying height is generally higher for dented surfaces. For these parameters the flying height for a *flat* guide surface is $0.785\mu m$.

7.4 Transient Effects

In magnetic recording applications system parameters such as the tape tension, and the tape speed are seldom stationary. Quick starts and stops of the tape are required

to increase the data access rates. Some systems such as the 3M Data Cartridge have inherent transient tension characteristics while the tape is wound from one spool to the other. In helical-scan recording applications the interaction between the magnetic head which is rotating at a high rate and the tape which is being transported slowly, can cause undesirable wave propagation in the tape. Severe signal drop-outs occur if an asperity or a tape imperfection enters the head tape interface. Considering all of these effects, it is important to understand the implications of these transient phenomena on the tape behavior in the interface. Therefore, in this section we study some of these transient effects encountered in the 2D foil bearing problem.

The literature of the transient foil bearing problem is given in Section 1.1.3. To the best of our knowledge, the tape inertia and squeeze film effects of the air bearing are not combined in a 2D study except for Heinrich and Connelly's paper [29].

7.4.1 Transient Effects in Linear Recording

In this section we present several case studies for the transient effects in linear recording. The parameters of this analysis are given in Table 7-2. The analysis is started from the steady state solution of the 2D problem.

Tension Reduction

In Figures 7-15 and 7-16 a case in which the tape tension is reduced from $276.7N/m$ to $193.7N/m$ in $1ms$ is shown. Figure 7-15 shows snap shots of the tape's reaction to this reduction. Note that as the tape tension is decreased the distance between the tape and the guide increases. This increase starts to take place from the entry side of the tape, and propagates toward the exit side. Due to the effective cushioning provided by the air bearing the effect of the tension change propagates mildly through the interface. The final flying height is $0.54\mu m$ and it is reached in roughly $9ms$. This is roughly 20% longer than the time required for the tape to travel the length of the lubrication zone between points L_{x1} and L_{x2}[6]. For clarity we show two cross sections of this transient

[6] $\mid L_{x2} - L_{x1} \mid = 3.7mm$

motion in Figure 7-16. The column on the left shows the cross section in the running direction, $(x, L_y/2)$ and the column on the right shows the cross section in the axial direction, $(L_x/2, y)$. From this figure we notice that the major wave action is in the running direction of the tape. The foil bearing reaction to the tension change is not immediate. In the $(1ms)$ duration of tension variation the separation shows hardly any change.

Tension Increase

In Figures 7-18 and 7-17 we show the transient tape displacement in a case that is the opposite of the previous case study. Here, we allow the tension to increase to $359.7N/m$ in the same length of time. As in the tension decrease case the effect moves from the entry side to the exit side with a smooth motion in approximately $9ms$. The steady state flying height is $0.33\mu m$. These results show that the same amount of tension increase and decrease do not correspond to the same amount of flying height change. However, besides this result, there is not a fundamental difference between the tension decrease and increase situations.

Figure 7-14 shows the steady state flying height of the three different uniform tension cases, $T_x = 193.69, 276.7$ and $359.71N/m$. The decrease in the tape guide separation, h, is non-linear even though the tension is reduced 30% at each case. We also note that the minimum flying height stays at the asperity level, for all of the three cases.

Tape Speed Reduction

Figures 7-19 - 7-20 show a case where the tape transport speed, V_x, is reduced from $0.5m/s$ to $0.35m/s$ in $1ms$. As a result of this, the steady state flying height reduces to $0.31\mu m$. Similar to the previous two cases the tape displacement reduction propagates as a slowly moving axial wave. Total time to reach the steady state is $12\mu s$. This suggests that the time to reach steady state is a function of the tape speed as predicted by Eshel [17] and as observed by Stahl et al. [58]. The tape response is similar to the cases in which tension is varied.

One of the observations common for all of the above three cases is that the displace-

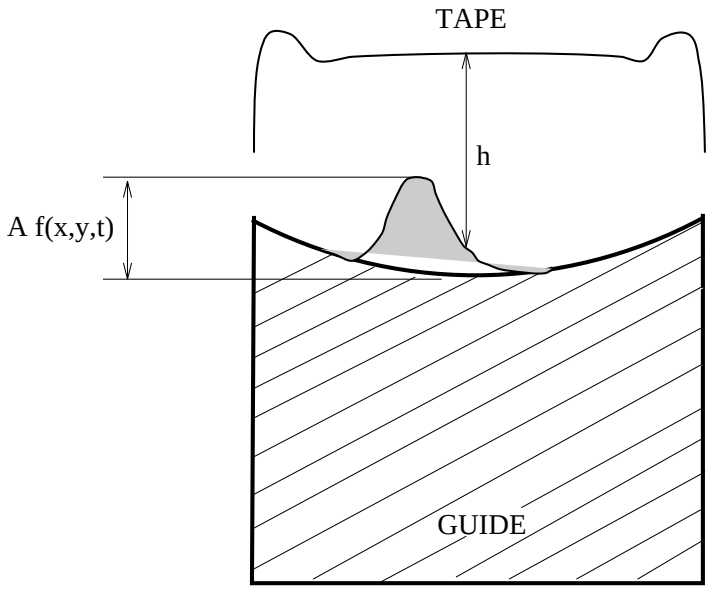

Figure 7-4: A schematic view of the tape-guide separation, h.

ment wave propagation is in the running direction of the tape. We also see that the minimum flying height is limited approximately by the back surface roughness of the tape and does not change with changing tape tension or speed. Another common finding is that the foil bearing reaction to the tension and speed changes is not immediate. In fact in the duration of the change, $(1ms)$, the tape-guide separation stays nearly stationary. We attribute the robustness of the behavior in the interface to the damping created by the air lubrication. Had it not been for the air bearing these transient changes would have caused much different results.

Moving Asperity in the Interface

Asperities going into the head-tape interface cause signal dropouts. These asperities may be stuck on the back surface of the tape as in the case of tape surface imperfections, or they may be dust particles that get caught in the air flow toward the interface. Prediction of the tape behavior when an asperity gets into the interface is useful in designing an optimal tape recording system.

In Figure 7-21 the tape's reaction to an asperity going through the interface is shown.

In this figure the asperity moves with the same speed as the tape. Its path is linear and located at the middle of the tape. This case represents an asperity that is stuck to the back side of the tape. We assume that this asperity is rigid, and model it with the following sinusoidal function,

$$\bar{\delta}(x,y,t) = \begin{cases} A \sin \frac{(y-(y_o(t)-aL_y/2))\pi}{aL_y} \sin \frac{(x-(x_o(t)-aL_y/2))\pi}{aL_y}, & \text{if } x_o - aL_y/2 \le x \le x_o + aL_y/2, \\ & \text{and} \\ & y_o - aL_y/2 \le y \le y_o + aL_y/2 \\ 0 & \text{otherwise} \end{cases} \tag{7.30}$$

where, A is the magnitude of the asperity, the point $(x_o(t), y_o(t))$ is the center of the asperity and a is a constant used to determine width and the length of the asperity. The value of a is between zero and one. Note that the function given in Equation (7.30) is valid only for the asperity aspect ratio[7] of one. Similar to Equation (5.1), the asperity center is given the following linear motion,

$$\begin{aligned} x_o(t) &= V_L \cos(\Gamma)t + x_i \\ y_o(t) &= V_L \sin(\Gamma)t + y_i \end{aligned} \tag{7.31}$$

where, V_L is the speed of the asperity, Γ is the slope of the asperity's path, and (x_i, y_i) is the initial location of the asperity.

The tape-guide spacing in the presence of the asperity is shown schematically in Figure 7-4. This variable is given as,

$$h(x,y,t) = w(x,y,t) + \delta(x,y) - \bar{\delta}(x,y,t) \tag{7.32}$$

The height of the asperity in Figure 7-21 is $2\mu m$ whereas the initial flying height of the tape is $0.785\mu m$. The width of the asperity is $1.27mm$. This figure reveals several interesting phenomena, first of which is the observation that an asperity whose amplitude is considerably higher than the steady state head tape spacing can move through the

[7]The ratio of the asperity's length to its width.

head tape interface without crash. In fact we were able to simulate an asperity with $6\mu m$ amplitude move through this interface. As the distance between the asperity and the tape becomes lower than the mean roughness value of the tape, σ_t, the contact pressure supplies most of the loading near the tip of the asperity. The contact pressure increases with increasing asperity height.

Close inspection of the pressure profiles given in Figure 7-21 shows that the pressure solution has a spike on the upstream side and a dip on the downstream side of the asperity. This can be better seen in the cross sectional view given in Figure 7-22. Note that the tape-guide spacing, h, is extremely small near the asperity tip and that the maximum air pressure is located slightly toward the upstream side of the tip. The spike occurs because the tape-guide spacing has a converging wedge shape on the upstream side. The dip is caused by the diverging wedge shape on the downstream side. The tape displacement is not greatly affected by the subambient pressures on the downstream side of the asperity because of the tent-pole shape that the tape deforms into.

7.4.2 Transient Effects in a Helical-Scan Application

In Figure 7.23 we show the simulation of the transient effects in a helical-scan like application. The tape speed, V_x, is $1m/s$ and initially the drum is stationary. We first find the steady state solution of the case with uniform transport speed of $1m/s$. Once we obtain that solution, we let $t = 0$, and the left half of the drum starts to rotate. The surface speed of the drum, V_x^G reaches $5m/s$ in $1ms$. In the mean time a doubly sinusoidal surface protrusion also strats to move with the rotating part of the drum. The center of the protrusion is initially located at $(x_i, y_i) = (0, 4.4)mm$, and it moves with the same speed as the drum. The protrusion height, A, is $6\mu m$ and the width parameter a is 0.1. For this application we used unequal nodal spacing on the pressure solution domain. The nodal density was increased on the free edges and the exit side of the foil bearing as well as around the path of the protrusion. The nodal spacing used for this case is given in Table 7.2

y range	Node	Δy	x range	Node	Δx
0.5×10^{-3}	9	0.625×10^{-4}	1.7×10^{-2}	171	1.0×10^{-4}
4.0×10^{-3}	43	1.02941×10^{-4}	1.85×10^{-2}	201	5.0×10^{-5}
5.0×10^{-3}	63	5×10^{-5}	1.922807×10^{-2}	208	1.04×10^{-4}
7.5×10^{-3}	88	1×10^{-4}			
8.0×10^{-3}	96	5.8863×10^{-4}			

Table 7.2: Node spacing for the pressure domain for helical-scan simulation

The y components of the tape, V_y and the drum, V_y^G, velocities as well as the helix angle, Γ, are zero. The protrusion shape, and motion are given by Equations (7.30), and (7.31). The parameters of the tape are given in Table 7.5.

The tape-drum spacing is shown in Figure 7.23 and corresponding pressure profile is given in Figure 7.24. We see that the tape-drum spacing, h, is higher over the rotating drum where the higher shear rate causes higher air pressures. We see that this zone propagates in the downstream direction faster than the protrusion. The protrusion, at the same time, creates a tent-pole like displacement which is localized around itself. This is similar to the asperity case shown before. The pressure profile near the protrusion is also similar to before; it has a spike at the upstream side of the protrusion due to the converging spacing, and it has a dip on the downstream side due to diverging spacing, h.

The drum and the protrusion are moving rather slowly compared to the load speeds we considered in Chapter 5, for that reason the tape inertia and subsequent wave propagation are insignificant in this simulation. Note that at the drum speed of $5m/s$ the air bearing is very effective in damping out the dynamic changes in the tape. The effects are localized near the protrusion.

7.5 Summary and Conclusions

In this chapter we analyzed the foil bearing problem in magnetic recording applications. We considered the effects of the finite tape width as well as transient effects on the tape

displacements in the tape-guide interface.

For the parameters that we studied, we observed that as we consider narrower tapes the displacement boundary layers forming on the lateral edges of the tape mix and the flat zone in the the cross-tape direction diminishes. Non-uniform tension variations in the cross-width direction also affect the flatness of the mid-section of the tape. These non-uniformities of the flying height could have an important impact on the multi-channel recording since the quality of the magnetic signal depends on the head-tape gap.

Our simulations showed that the tape is supported by rigid body contact on the lateral edges. We saw no evidence of air bearing support, moreover our numerical scheme fails to converge if we neglect the rigid body contact. The maximum rigid body contact occurs at the exit side of the tape. The flying height at the lateral edges, in the constant gap zone, is near the surface asperity height used in modeling the contact pressure. We observed that this flying height stays the same for all of the tape speeds, tape tensions and recording modes we considered. The existence of relatively high contact pressures at the lateral edges make both the tape and the guides vulnerable to wear at these locations.

When we studied the transient changes in the system parameters such as tape speed and tension, we see that the coupled system is effective to damp out the excessive dynamic action. We observed that the changes propagate with a speed close to one half of the tape transport speed[8].

Simulation of an asperity going through the tape-guide interface showed that the tape would lift on an air layer above the moving asperity and allow it to go through the interface with minimal contact with the back side of the tape. We were able to simulate this with asperity heights nearly ten times bigger than the undisturbed tape-guide spacing.

Our simulations also showed that the air pressure on the downstream side of the asperity has a subambient dip and on the upstream side of the asperity it has superambient

[8]Our simulations suggest that this propagation speed is actually higher than the half of the tape transport speed.

spike. For the tape speeds that we considered the effect of the moving asperity was seen to be localized due to strong damping provided by air.

We also studied a split-drum recording case. We showed the stages of pressure built-up as the drum starts to rotate and as the head simulated by a doubly sinusoidal function enters the interface. We were able to simulate drum speeds up to $10m/s$. Mixing of the air flow becomes complicated near a moving protrusion and requires a very finely resolved mesh. An adaptive meshing algorithm for the Reynolds equation solution should be used, to resolve the steep pressure gradients occurring at higher drum speeds.

N	No. of nodes for tape (y-dir.)	71	
M	No. of nodes for tape (x-dir.)	172	
N_p	No. of nodes for air bearing (y-dir.)	71	
M_p	No. of nodes for air bearing (x-dir.)	172	
Δt	Time step size	0.1	μs
α	Integration parameter	0	
β	Integration parameter	1/4	
γ	Integration parameter	1/2	
V_x	Tape speed	2.54	m/s
T_x	Tape tension	278	N/m
c	Tape thickness	20	μm
L_x	Tape length (appr.)	15	mm
L_y	Tape width	6.35	mm
E	Young's modulus	4.0	GPa
ρ_a/c	Volumetric mass density of the tape	1400	kg/m^3
ν	Poisson's ratio	0.3	
R	Guide radius	2.04	cm
θ_L	Wrap angle (See Fig.2-3)	8.89°	
θ_R	Wrap angle	8.89°	
θ_{e1}	Entry angle	12°	
θ_{e2}	Exit angle	12°	
$\bar{L}$	Distance between far end supports	8.44	cm
P_a	Ambient pressure	84.1	kPa
μ_a	Air viscosity	1.81×10^{-5}	$N/m^2 s$
λ_a	Mean free path length of air	63.5	nm

Table 7.3: Specifications for test case from Stahl et al.

N	No. of nodes for tape (y-dir.)	71	
M	No. of nodes for tape (x-dir.)	172	
N_p	No. of nodes for air bearing (y-dir.)	71	
M_p	No. of nodes for air bearing (x-dir.)	172	
Δt	Time step size	0.1	μs
α	Integration parameter	0	
β	Integration parameter	1/4	
γ	Integration parameter	1/2	
V_x	Tape speed	1.27	m/s
T_x	Tape tension	276.7	N/m
c	Tape thickness	38.1	μm
L_x	Tape length (appr.)	15	mm
L_y	Tape width	6.35	mm
E	Young's modulus	4.0	GPa
ρ_a/c	Volumetric mass density of the tape	1400	kg/m^3
ν	Poisson's ratio	0.35	
R	Guide Radius	2.0	cm
θ_L	Wrap angle (See Fig.2-3)	5.2734°	
θ_R	Wrap angle	5.2734°	
θ_{e1}	Entry angle	16.6654°	
θ_{e2}	Exit angle	16.7647°	
$\bar{L}$	Distance between far end supports	8.44	cm
P_a	Ambient pressure	101.3	kPa
μ_a	Viscosity of air	1.81×10^{-5}	$N/m^2 s$
λ_a	Mean free path length of air	63.5	nm

Table 7.4: Specifications for test case from Vogel and Groom.

N	No. of nodes for tape (y-dir.)	115	
M	No. of nodes for tape (x-dir.)	274	
N_p	No. of nodes for air bearing (y-dir.)	96	
M_p	No. of nodes for air bearing (x-dir.)	208	
Δt	Time step size	0.1	μs
α	Integration parameter	0	
β	Integration parameter	1/4	
γ	Integration parameter	1/2	
V_x	Tape speed	1.0	m/s
T_x	Tape tension	90.0	N/m
c	Tape thickness	20.0	μm
L_x	Tape length (appr.)	19.2	mm
L_y	Tape width	8.0	mm
E	Young's modulus	4.0	GPa
ρ_a/c	Volumetric mass density of the tape	1400	kg/m^3
ν	Poisson's ratio	0.3	
R	Guide Radius	1.0	cm
θ_L	Wrap angle (See Fig.2-3)	45°	
θ_R	Wrap angle	45°	
θ_{e1}	Entry angle	9.6480°	
θ_{e2}	Exit angle	10.1598°	
$\bar{L}$	Distance between far end supports	N/A	
P_a	Ambient pressure	101.3	kPa
μ_a	Viscosity of air	1.81×10^{-5}	$N/m^2 s$
λ_a	Mean free path length of air	63.5	nm

Table 7.5: Specifications for the helical scan case.

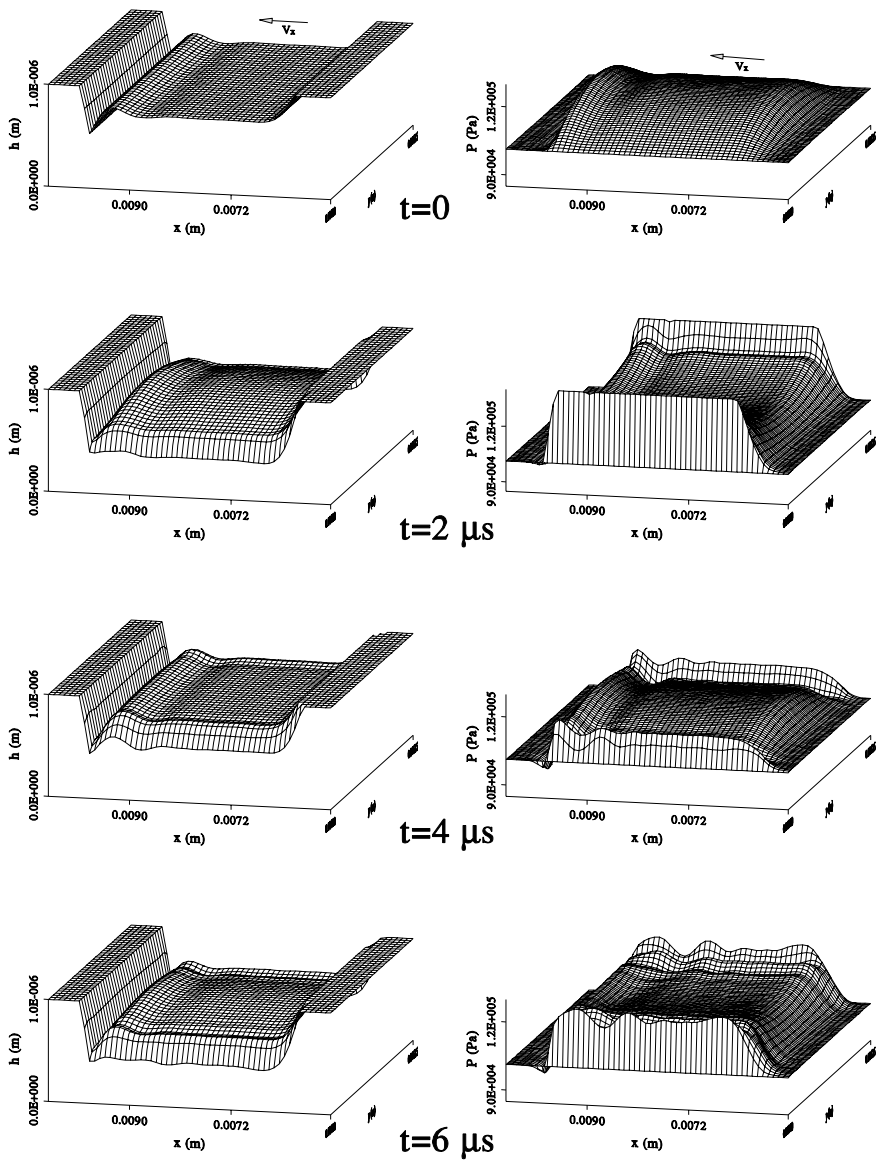

Figure 7-5: The initial stages of the transient analysis. Due to the state of the initial conditions the wave action in the tape and the pressure domains is not physical. See Table 7.4 for problem parameters.

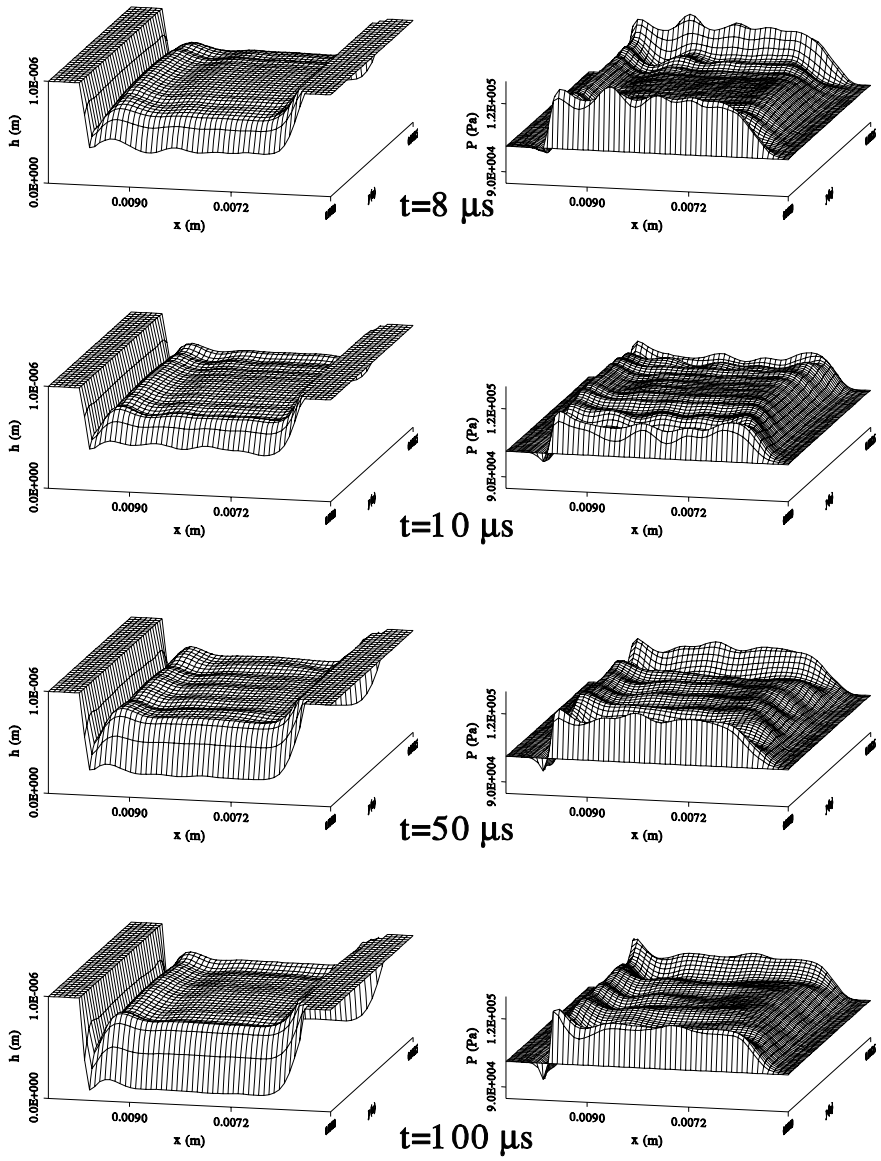

Figure 7-5: ctd.

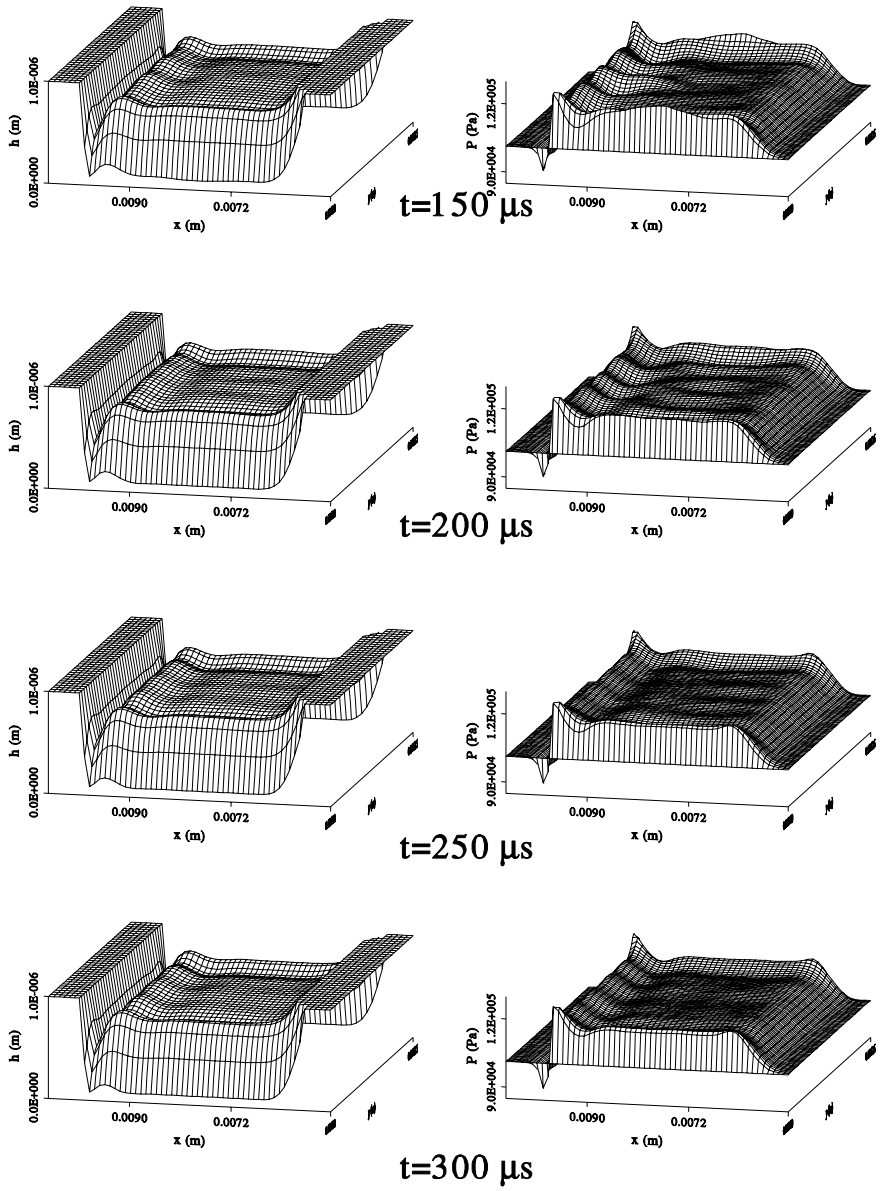

Figure 7-5: ctd.

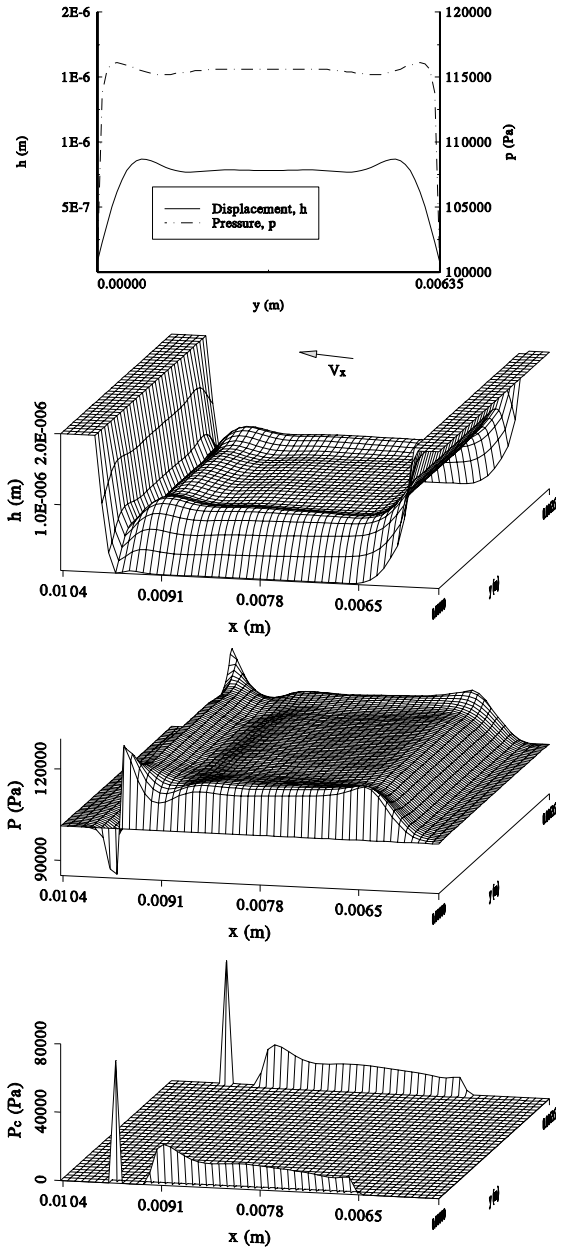

Figure 7-6: The tape-guide spacing, h, air pressure, p, and the contact pressure, p_c at steady state. The tape speed and tension are, $V_x = 1.27m/s$, and $T_x = 276.7N/m$. The mid point flying height is $h_o = 0.785\mu m$. See Table 7.4 for problem parameters.

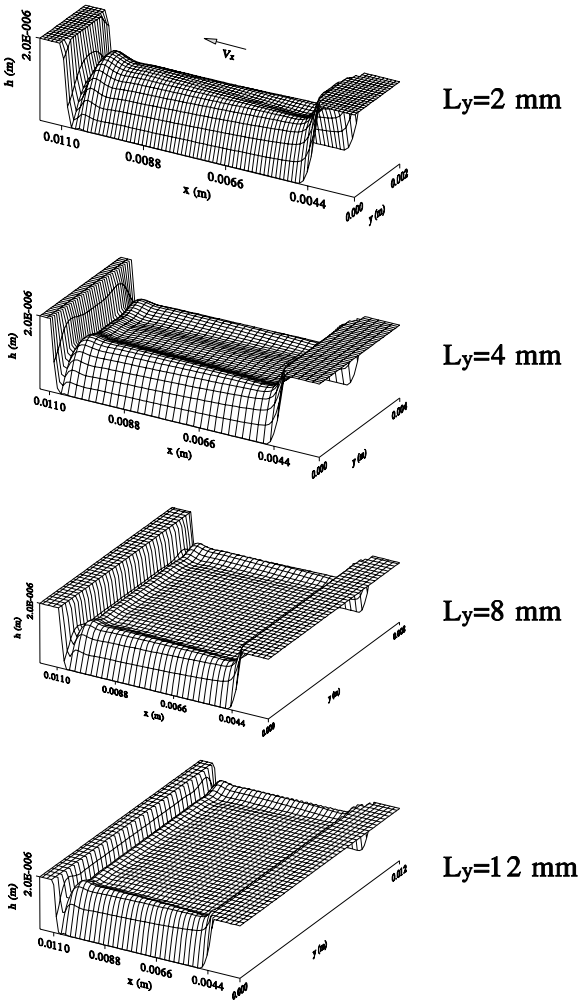

Figure 7-7: Steady state tape-guide spacing, h, for different tape widths, L_y. The mid-point flying heights, h_o, are $1.342, 1.217$ and $1.207\mu m$, respectively. The tape speed and tension are, $V_x = 2.54m/s$, and $T_x = 278N/m$, tape thickness is $c = 20\mu m$. See Table 7.3 for problem parameters.

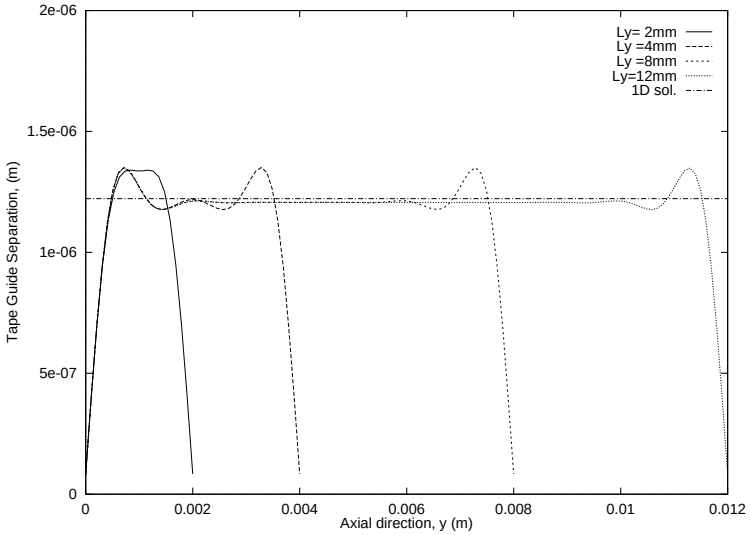

Figure 7-8: Cross section of the steady state tape-guide spacing, h, for different tape widths at $x = L_x/2$. The mid-point flying heights, h_o, are $1.342, 1.217$ and $1.207\mu m$, respectively. See Table 7.3 for problem parameters.

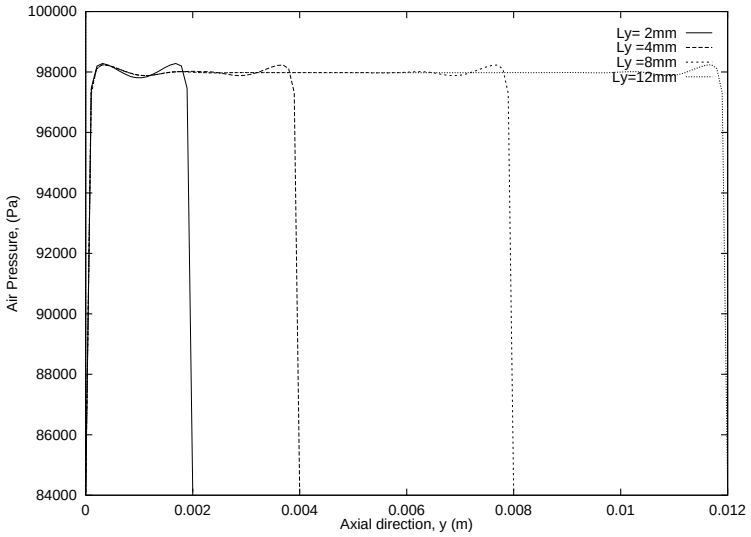

Figure 7-9: Cross section of the steady state air pressure, p, for different tape widths at $x = L_x/2$. See Table 7.3 for problem parameters.

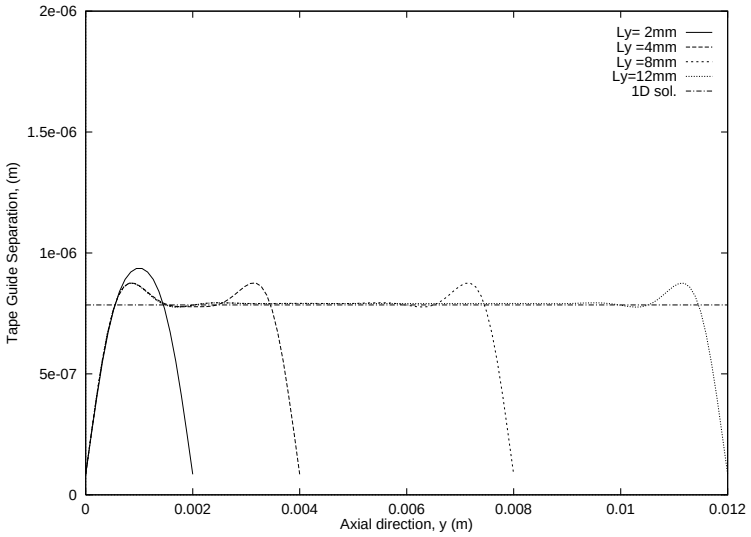

Figure 7-10: Cross section of the steady state tape-guide spacing, h, for different tape widths at $x = L_x/2$. See Table 7.4 for problem parameters.

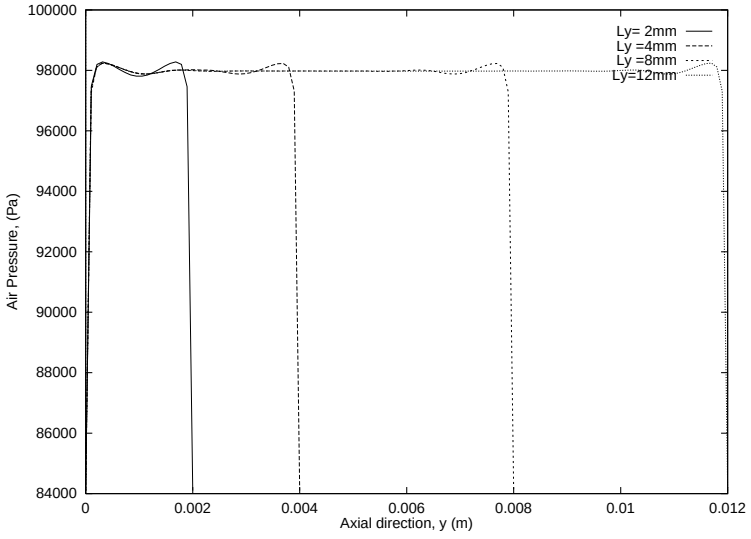

Figure 7-11: Cross section of the steady state air pressure, p, for different tape widths at $x = L_x/2$. See Table 7.4 for problem parameters.

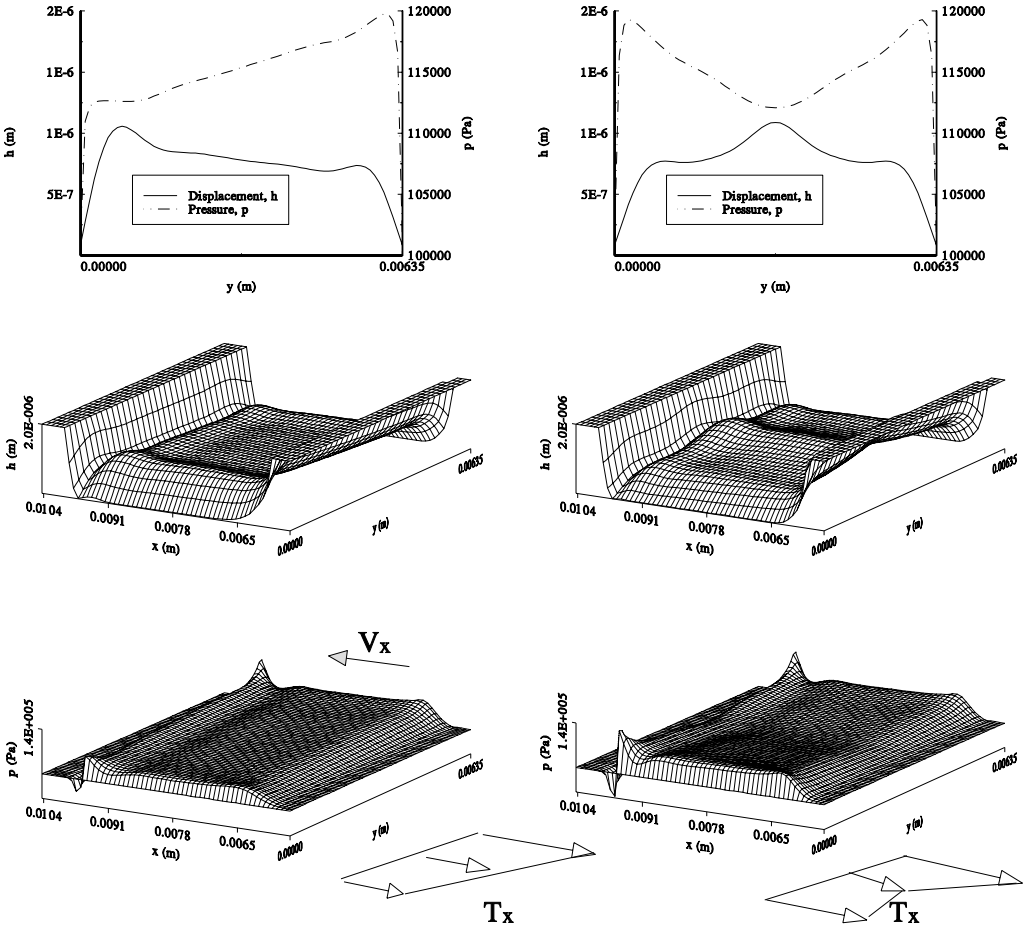

Figure 7-12: The effect of axial tension variation on steady state tape-guide spacing, h. Nominal tape tension is $T_x = 276.7N/m$, with 30% variations as shown. The tape speed and thickness are, $V_x = 0.5m/s$, and $c = 38.2\mu m$. See Table 7.4 for other problem parameters.

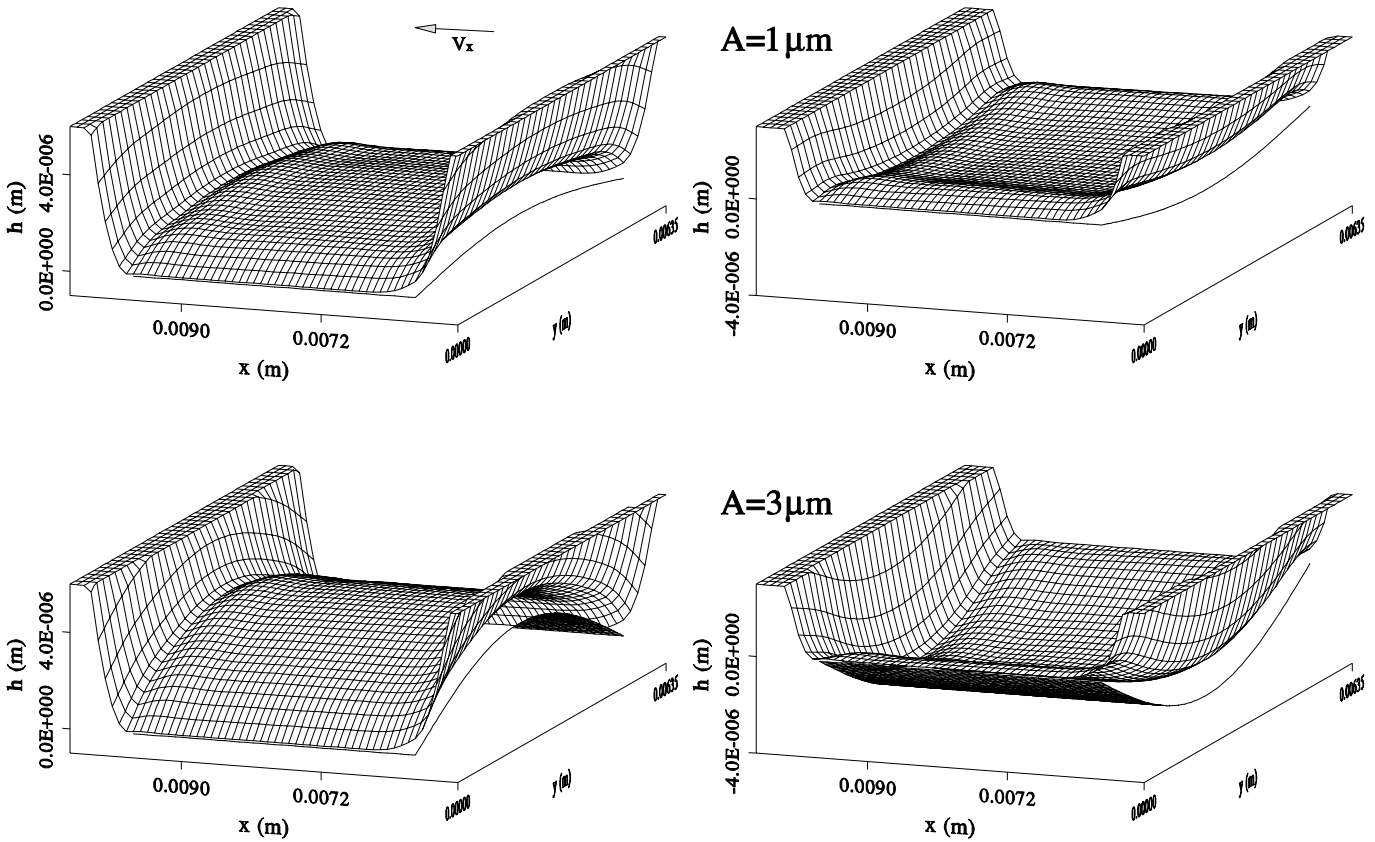

7-13: The effect of axial guide shape on the steady state tape guide separation. The guide shape is defined in the axial direction by, $A\sin(\frac{\pi y}{L_y})$. See Table 7.4 for problem parameters.

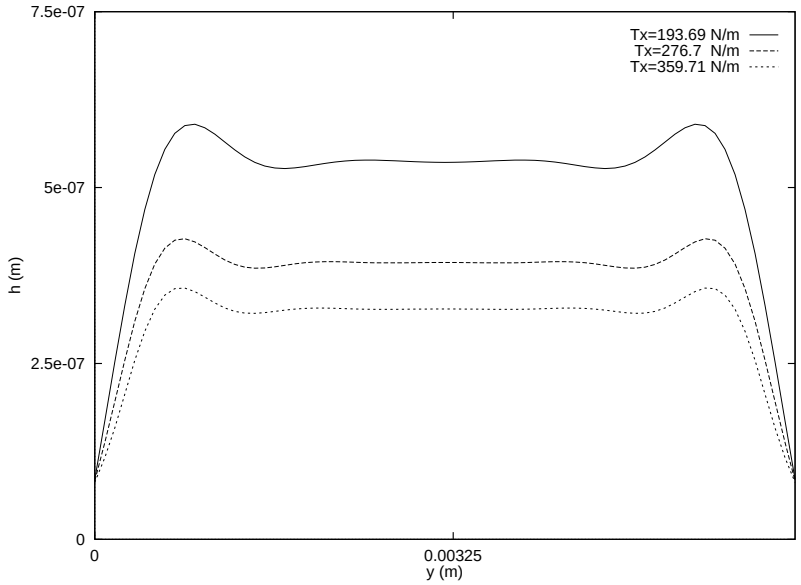

Figure 7-14: Steady state flying heights at cross-sections $(L_x/2, y)$, at 30% above and below the nominal tension, $T_x = 276.7N/m$. The flying heights are $0.54\mu m, 0.39\mu m$ and $0.33\mu m$ from top to bottom. See Table 7.4 for other problem parameters.

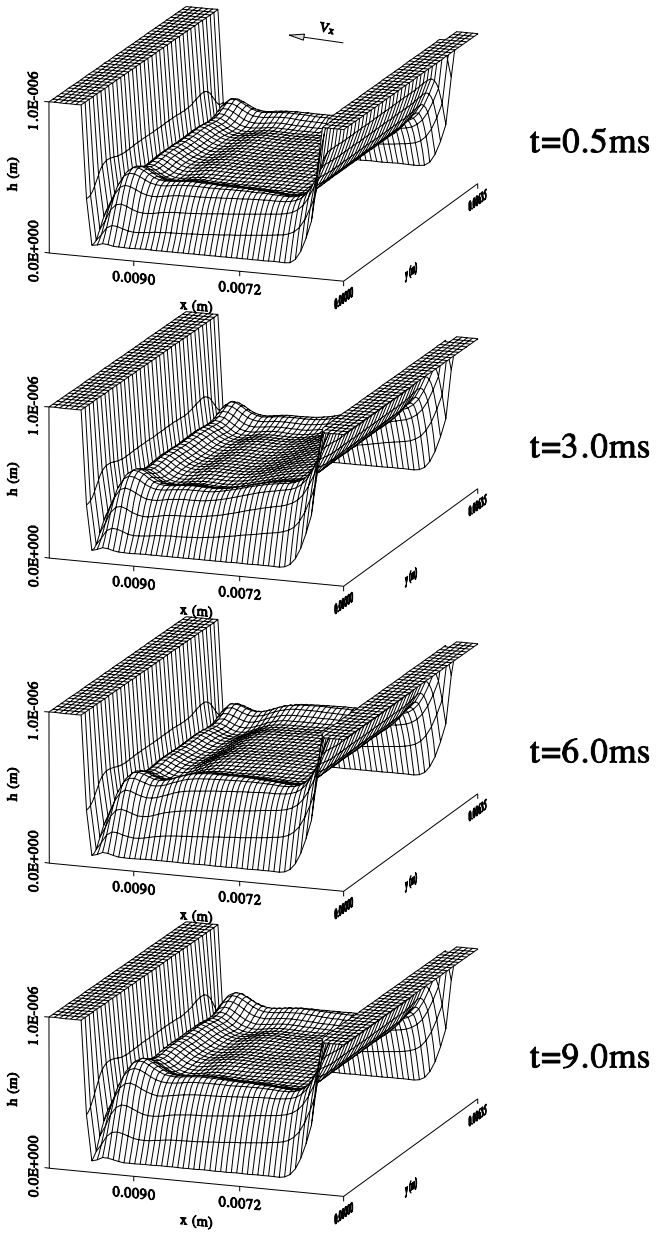

Figure 7-15: Transient effects while tension is reduced 30%, from $276.7 N/m$, in $1ms$. The flying height increases to $0.54\mu m$ from $0.39\mu m$. The steady state is reached in approximately $9ms$. Tape transport speed is $0.5m/s$. See Table 7.4 for other problem parameters.

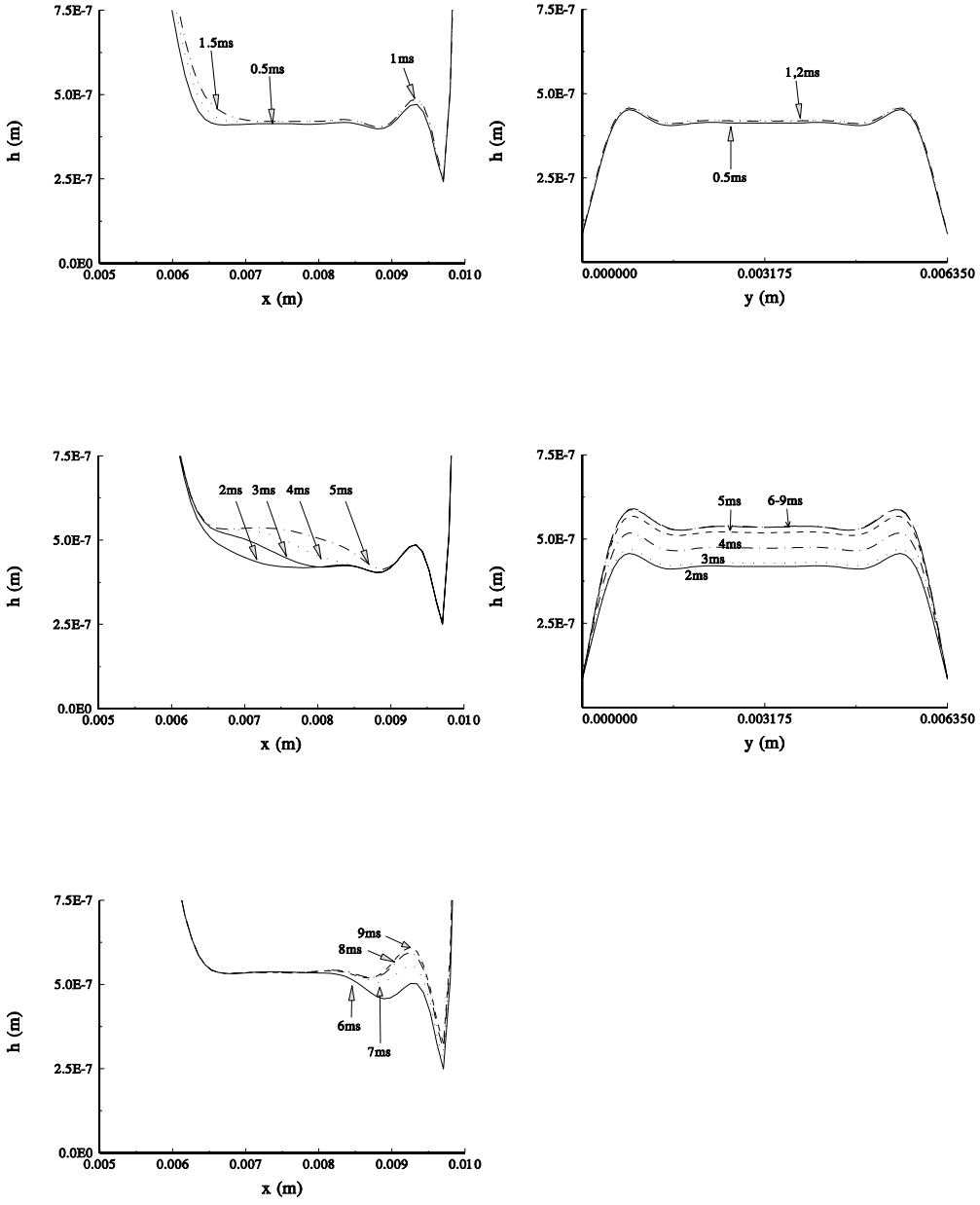

Figure 7-16: The cross sections at $(x, L_y/2)$ and $(x, L_y/2)$ for Figure 7-15.

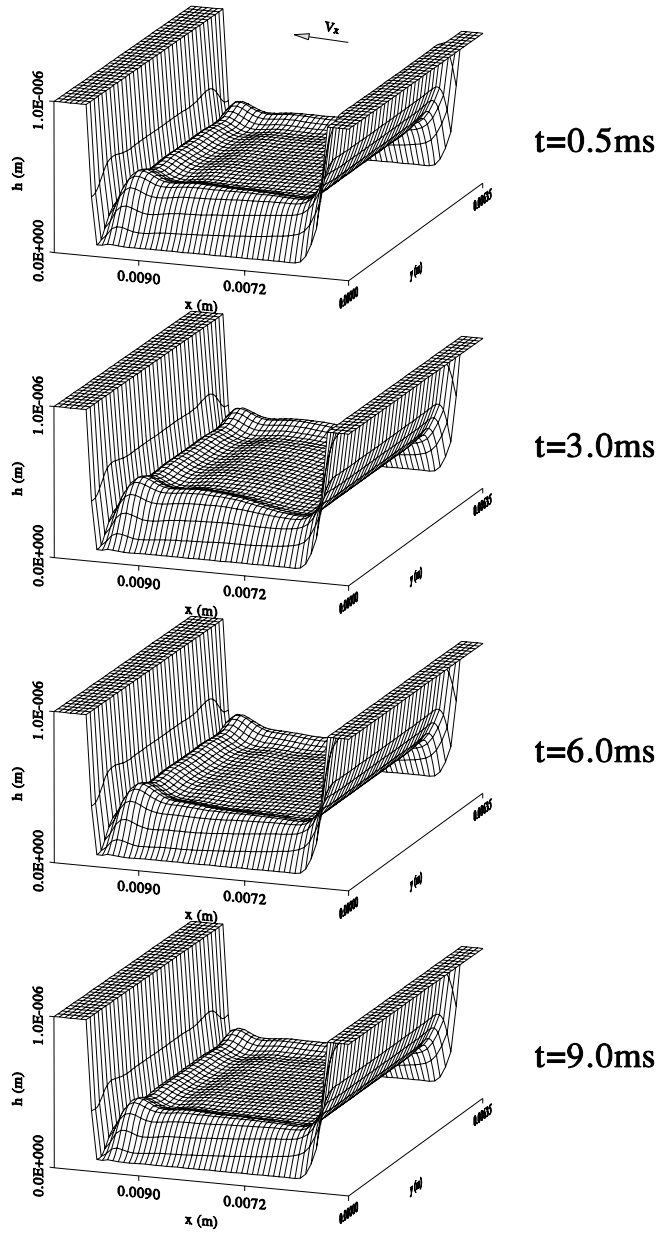

Figure 7-17: Transient effects while tension is increased 30%, from $276.7 N/m$, in $1ms$. The flying height reduces to $0.33\mu m$ from $0.39\mu m$. The steady state is reached in approximately $9ms$. The tape transport speed is $0.5m/s$. See Table 7.4 for problem parameters.

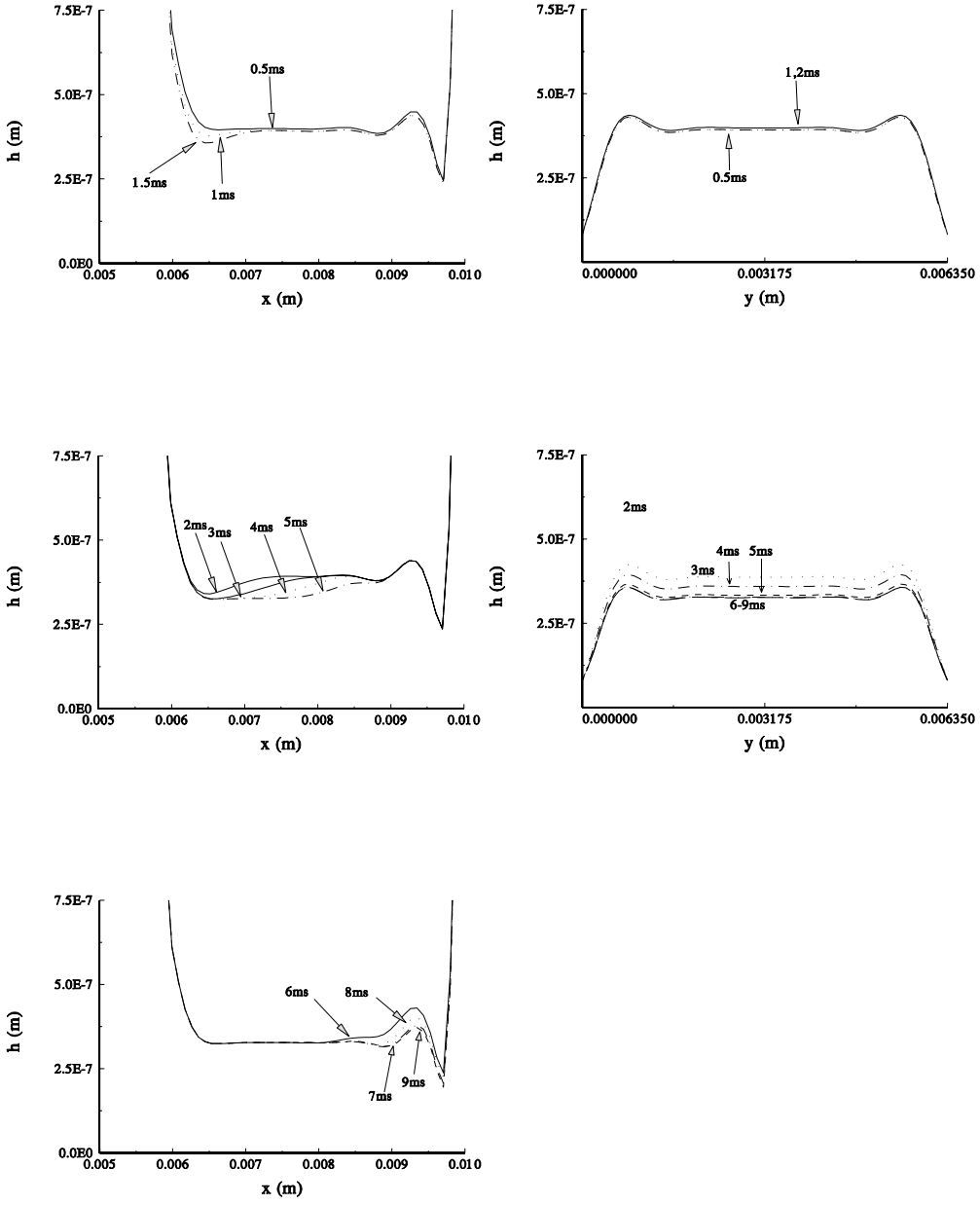

Figure 7-18: The cross sections at $(x, L_y/2)$ and $(x, L_y/2)$ for Figure 7-17

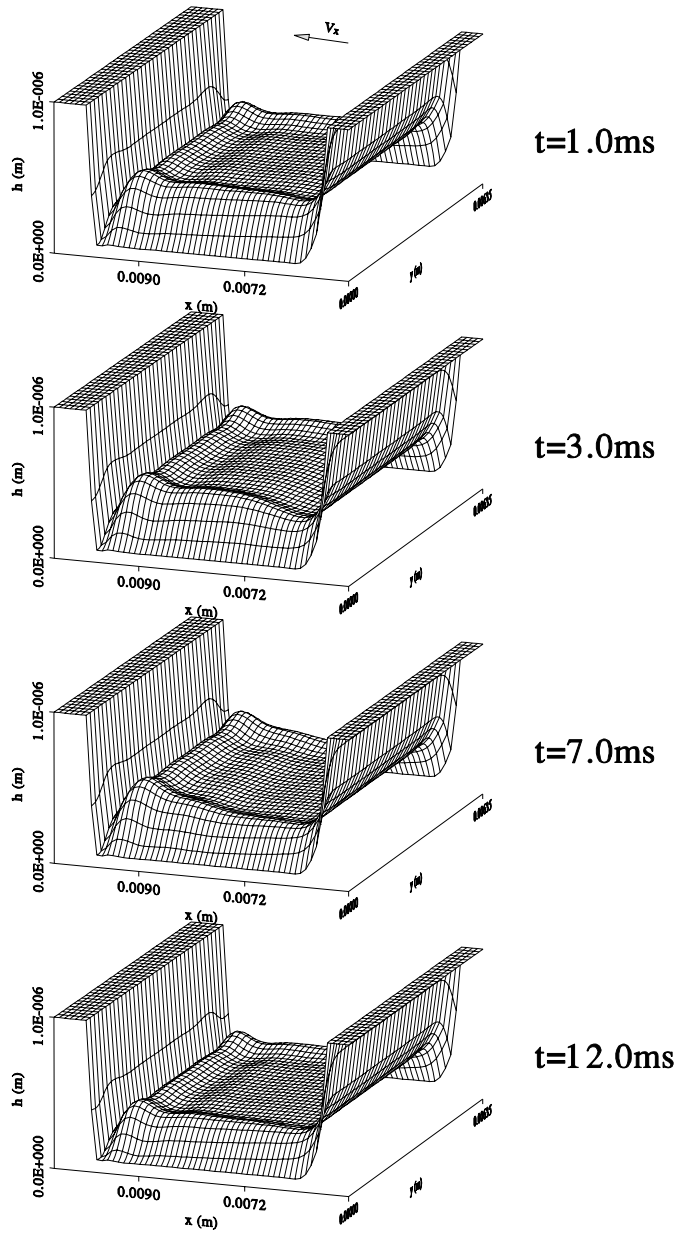

Figure 7-19: Transient effects while tape speed is decreased 30%, from $0.5m/s$, in $1ms$. The flying height reduces to $0.31\mu m$ from $0.39\mu m$. The steady state is reached in approximately $12ms$. See Table 7.4 for other problem parameters.

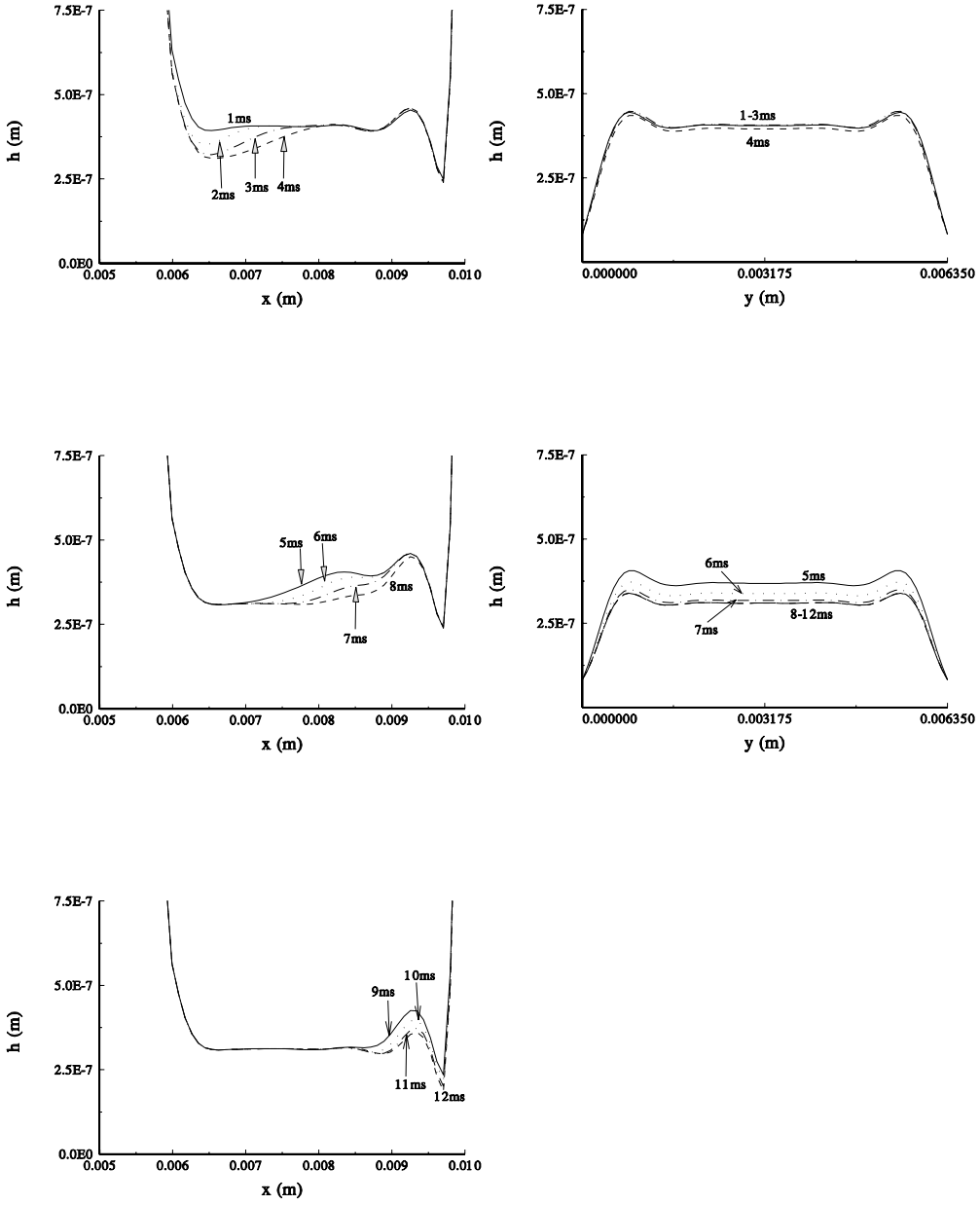

Figure 7-20: The cross sections at $(x, L_y/2)$ and $(x, L_y/2)$ for Figure 7-19

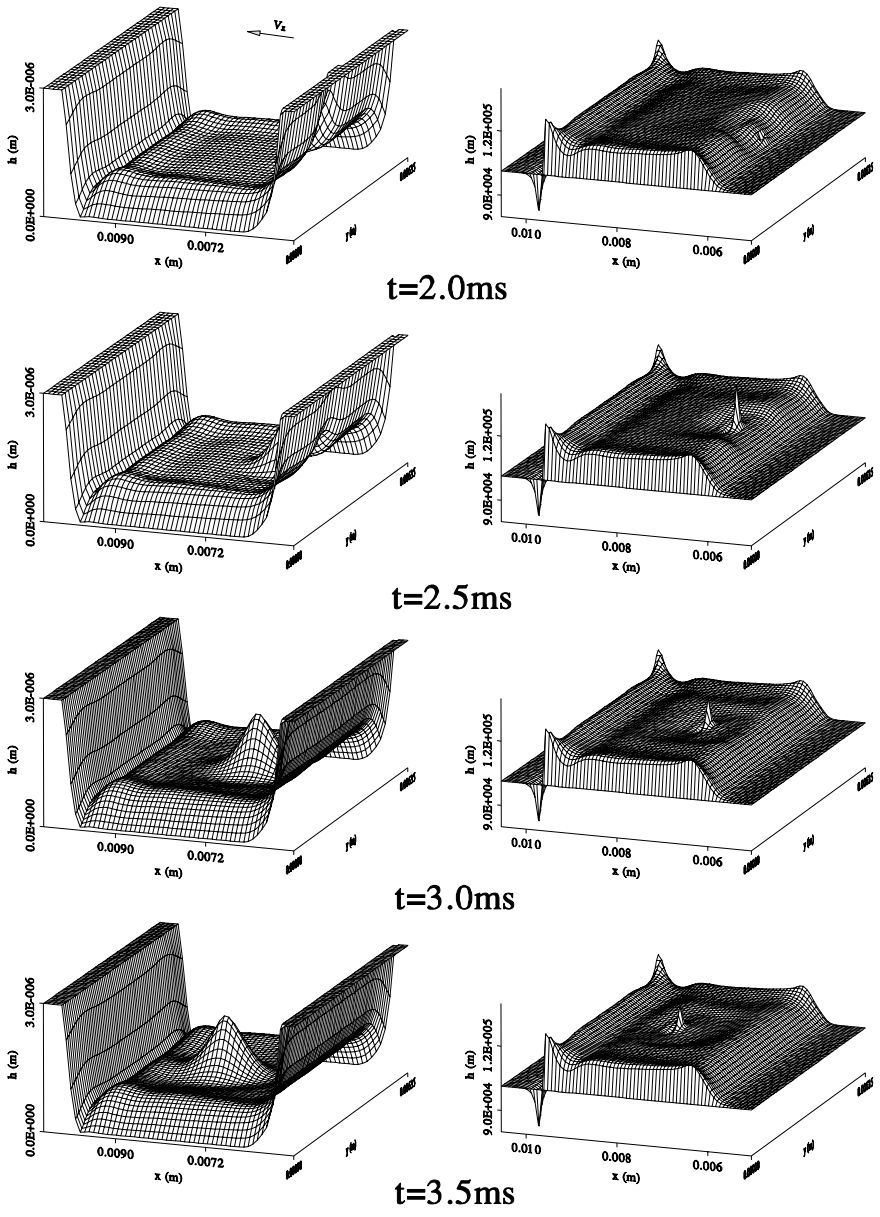

Figure 7-21: Transient effects while an asperity moves under the tape. The asperity is defined by Equation (7.29) where asperity height, $A = 2\mu m$, and $a = 0.1$. The asperity moves with the same same speed as the tape. See Table 7.4 for the tape parameters.

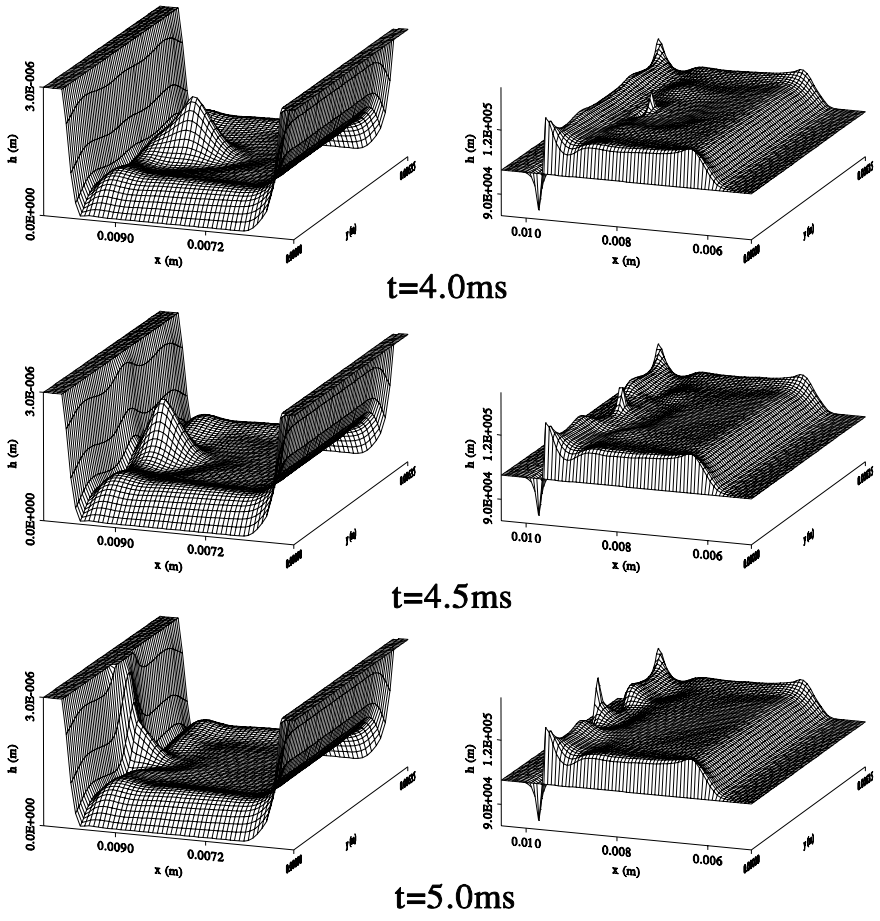

Figure 7-21: ctd.

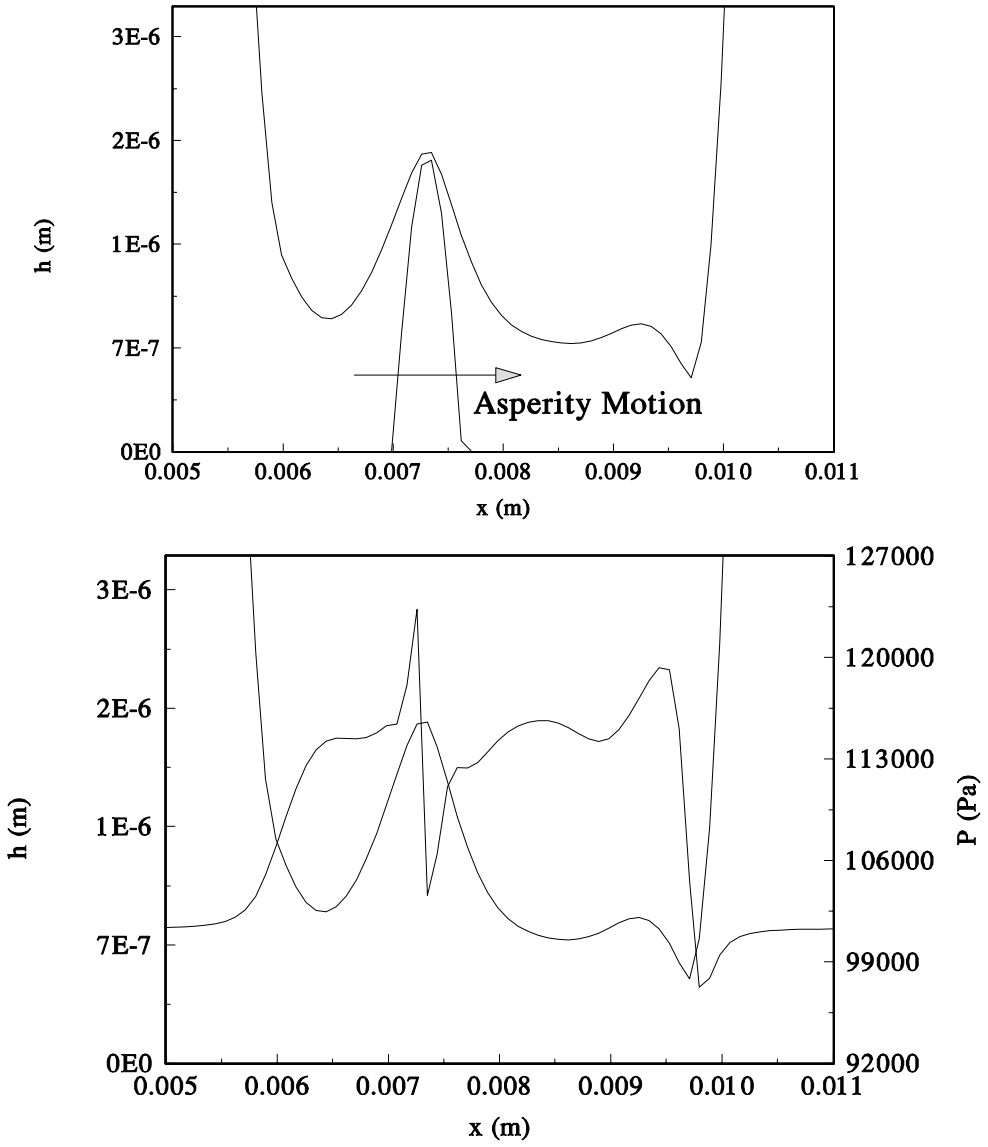

Figure 7-22: Tape displacement and pressure profiles at the cross section $(x, L_y/2)$ for the case given in Figure 7-21. Note that the node numbering is insufficient to resolve the pressure spike.

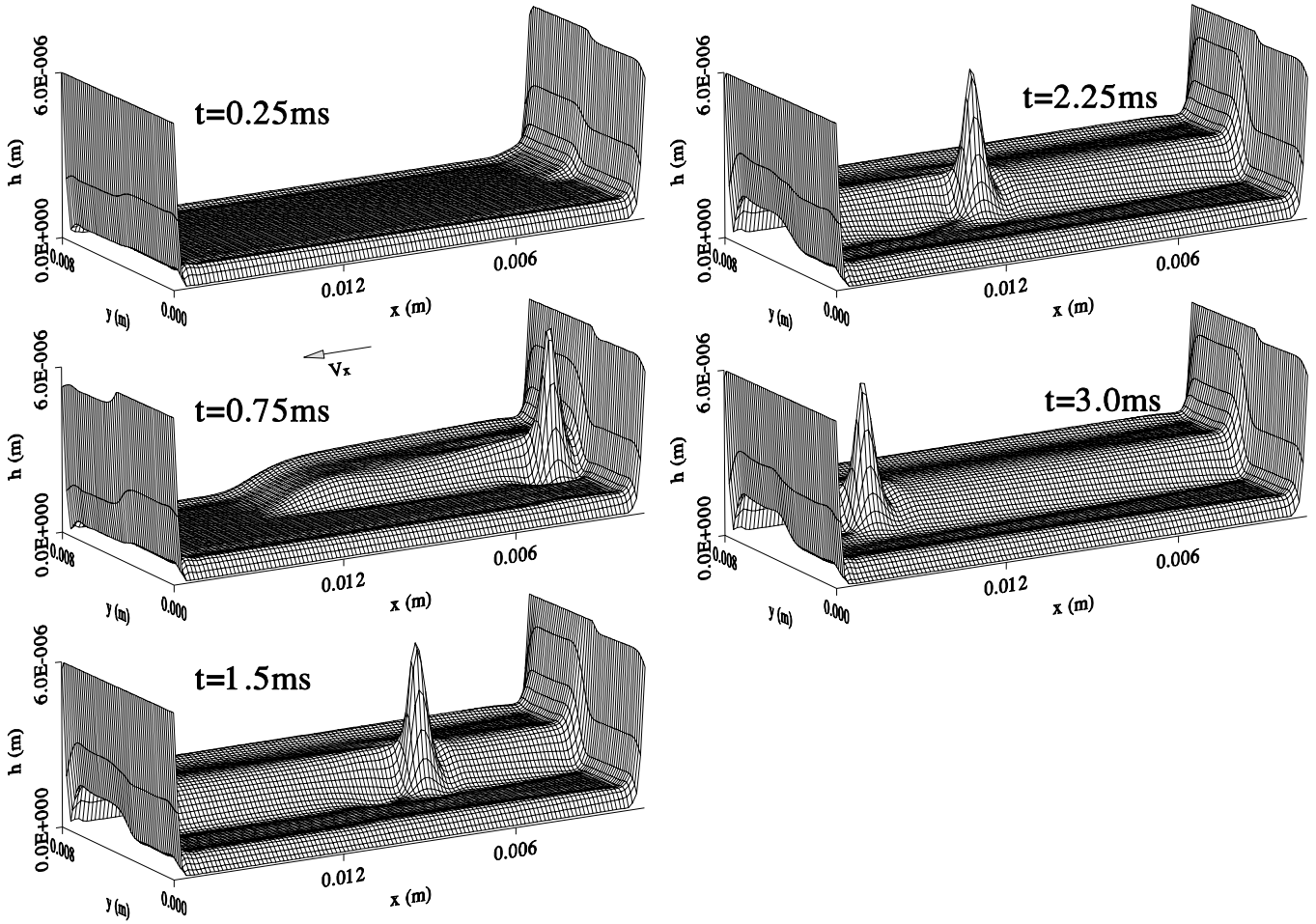

7-23: Transient displacement variation in a helical-scan like simulation. See Table 7.5 for problem parameters.

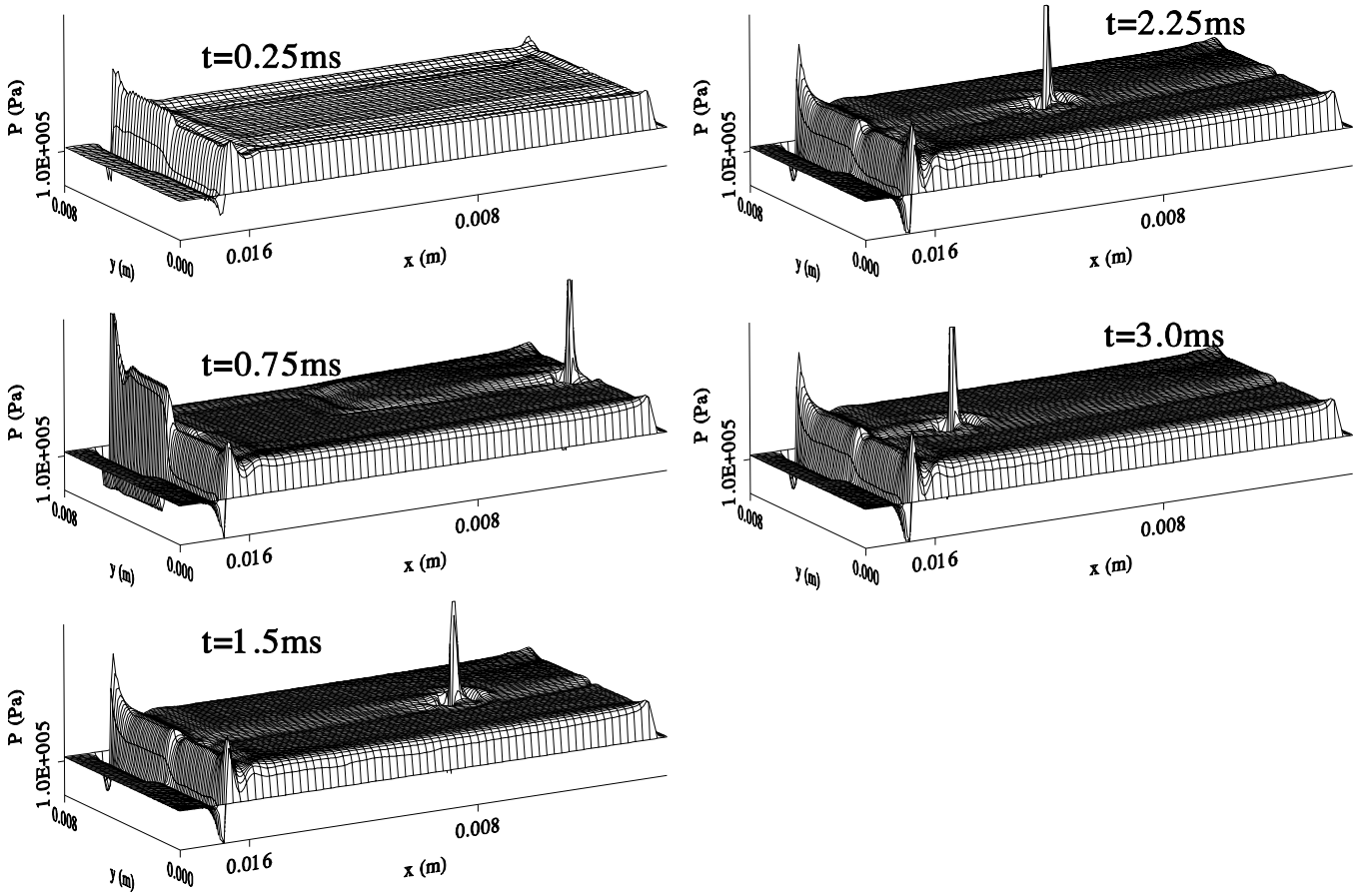

7-24: The pressure profiles corresponding to the case given in Figure 7.23. Transient pressure variation in a helical-scan like simulation. See Table 7.5 for problem parameters.

Chapter 8

Summary and Conclusions

In this thesis we analyzed the transient effects in the foil bearing problem applied to the magnetic recording applications. We included characteristics arising from tape inertia and finite tape width. The compressibility of air and first order slip-flow corrections are also included in our analysis.

We introduced a segmented model for the out-of-plane tape displacements. In this model the tape is modeled as a cylindrical shell in the wrap zone and as a plate in the straight segments between the guide pins and the tangency points. This choice allows us to analyze problems in which the angle of wrap is large. The air lubrication is modeled with the modified Reynolds equation.

We analyzed the foil bearing problem in the transient domain. The tape equation is discretized with central finite difference formulas in the spatial domain. The α-method is used for integration in the time domain. We used explicit time integration in solving the coupled problem to decrease the simulation time. The Reynolds equation is solved with ADI method. We investigated the effects of finite tape width, axial tension variations and tape inertia on the tape's displacement in the self lubrication zone for linear and split-drum formats.

We also analyzed the wave propagation in a circumferentially moving thin cylindrical shell due to a point load moving relative to the shell in the absence of air lubrication.

This analysis lead us to study the dispersive nature of the wave propagation in the thin shells.

Our conclusions are summarized below.

- **The Foil Bearing Problem**

  - For the parameters that we studied, we observed that as we consider narrower tapes the displacement boundary layers forming on the lateral edges of the tape mix and the flat zone in the the cross-tape direction diminishes. We saw that the non-uniform tension variations in the cross-width direction also affect the flatness of the mid-section of the tape. These non-uniformities of the flying height could have an important impact on the multi-channel recording since the quality of the magnetic signal depends on the head-tape gap.

  - Our simulations showed that the tape is supported by rigid body contact on the lateral edges. We saw no evidence of air bearing support. Moreover, our numerical scheme fails to converge if we neglect the rigid body contact. We found that the maximum rigid body contact occurs at the exit side of the tape. The flying height at the lateral edges in the constant gap zone was seen to be close to the value of the surface asperity height used in modeling the contact pressure. We observed that this flying height stays the same for all of the tape speeds, tape tensions and recording modes considered. The existence of relatively high contact pressures at the lateral edges make both the tape and the guides vulnerable to wear at these locations.

  - When we studied the transient changes in the system parameters such as tape speed and tension, we saw that the coupled system is effective to damp out the excessive dynamic action. We observed that the changes propagate with a speed close to one half of the tape transport speed[1].

[1]Our simulations suggest that this propagation speed is actually higher than the half of the tape transport speed.

- Simulation of an asperity going through the tape-guide interface showed that the tape would lift on an air layer above the moving asperity and allow it to go through the interface without damage due to contact with the back side of the tape. We were able to simulate this with asperity heights nearly ten times bigger than the undisturbed tape-guide spacing.
- Our simulations also showed that the air pressure on the downstream side of the asperity has a subambient dip and on the upstream side of the asperity it has superambient spike. For the tape speeds that we considered the effect of the moving asperity was seen to be localized due to damping by the air.
- We also studied a split-drum recording case. We showed the stages of pressure built-up as the drum starts to rotate and as the head simulated by a doubly sinusoidal function enters the interface. We were able to simulate drum speeds up to $10m/s$. Mixing of the air flow became complicated near a moving protrusion and required a very finely resolved mesh. An adaptive meshing algorithm for the Reynolds equation solution should be used, to resolve the steep pressure gradients occurring at higher drum speeds.

- **Wave propagation in a Cylindrical Shell**
  - We observed that the displacement wave caused by a point load applied in the step function manner propagates symmetrically around the load point. However, when the tape was put in a circumferential motion the symmetry was lost and the wavelength became longer in the direction of the shell's motion.
  - We also observed that the waves emanating from the load point reflect from the free edges as well as the pinned boundaries, and return back to the load point. Superposition of these waves was thought as the cause of the quasi-periodic motion at the load point. Increasing the tape transport speed resulted in large displacements.

- In the case of a moving point load the waves that occur on the tape and the load were seen to compete with each other. A critical load speed was identified at which the load penetrates the wave front in the tape.
- This critical speed became lower with increasing tape thickness, tape transport speed, and tape tension. We also observed the evidence of more edge flutter in thicker tapes.

- **Frequency Analysis of Wave propagation in a Cylindrical Shell**
  - We showed that the wave propagation in a circumferentially moving thin cylindrical shell is dispersive. The long waves encountered in this medium are dominated by the shell stiffness term, K, and the short wavelengths are dominated by a combination of the bending rigidity, tension and transport speed.
  - We also showed that the spatial step size effects the short wavelength behavior of the solution. In order to prevent the occurrence of incorrect wave speeds at short wavelengths, a safe rule is to use a step size that is 1/10th of the shortest wave length of interest.

In the future, adaptive mesh refinement may be applied to the solution of the Reynolds equation in order to resolve the abrupt pressure changes that occur near a moving protrusion. This would allow simulation of faster drum speeds in split-drum applications. The Reynolds equation solver that we used can be modified in such a way that it would handle atmospheric pressure boundary conditions under the tape. This would enable proper modeling of the atmospheric boundary conditions at the head window, and at the junction of the split drum in helical-scan models. A more complete tape model considering the effects of in-plane tape displacements and stresses can be used in modeling the helical-scan tape. This would open the way for understanding the effects of friction on the tape tension. A more comprehensive study of the tape parameters such as thickness and tension should be made to determine the effects of tape inertia in helical scan.

Bibliography

[1] G.G. Adams. A very efficient solution to the foil bearing problem. *ASME/ASLE Symposium on Tribology and Mechanics of Magnetic Storage Systems*, Oct 1986.

[2] G.G. Adams. A novel approach to the foil bearing problem. *ASLE SP-26*, 6:1–7, 1989.

[3] D.M. Albrecht, E.G. Laenen, and Chua Lin. Experiments on the dynamic response of a flexible strip to moving loads. *IBM Journal of Research and Development*, July 1977.

[4] E. J. Barlow. Derivation of governing equations for self acting foil bearing. *Journal of Lubrication Technology, Transactions of the ASME*, pages 334–340, July 1967.

[5] E. J. Barlow. Self acting bearings of infinite width. *Journal of Lubrication Technology, Transactions of the ASME*, pages 341–345, July 1967.

[6] T.B. Barnum and H.G. Elrod. A theoretical study of the dynamic behavior of foil bearings. *Journal of Lubrication Technology, Transactions of the ASME*, 133, 1971.

[7] T. Belytschko and T.J.R. Hughes, editors. *Computational Methods for Transient Analysis*. North-Holland, Amsterdam, 1983. chapter 9.

[8] Bharat Bhushan. *Tribology and Mechanics of Magnetic Storage Devices*. Springer-Verlag, NY, 1990.

[9] Garret Birkhoff and Vasilios A. Dougalis. Numerical solution of hydrodynamic problems. *Advances in Computer Methods for Partial Differential Equations*, 1975. ed. R. Vichnevetsky.

[10] D.B. Bogy, H.J. Greeenberg, and F.E. Talke. Steady solution for circumferentially moving loads on cylindrical shells. *IBM Journal of Research and Development*, 18(5):395, Sept 1974.

[11] A.T. Brewen, R.C. Benson, and V.J. Piarulli. A simple procedure for determining elastohydrodynamic equilibrium and stability of a flexible tape flying over a recording head. *ASLE, SP-19*, pages .43–51, Oct. 1985.

[12] Leon Brillouin. *Wave Propagation and Group Velocity.* Academic Press, NY, 1960.

[13] A. Burgdorfer. The influence of the molecular mean free path on the performance of hydrodynamic gas lubricated bearings. *Journal of Basic Engineering, Transactions of the ASME*, pages 94–100, March 1959.

[14] Marvin Camras. *Magnetic Recording Handbook.* Van Nostrand Reinhold Company, NY, 1988.

[15] V.J. Castelli and J. Privics. Review of numerical methods in gas bearing film analysis. *Journal of Lubrication Technology, Transactions of the ASME*, pages 777–792, Oct 1968.

[16] R.L. Coleman. A brief comparison of the accuracy of time dependent integration schemes for the reynolds equation. *Journal of Lubrication Technology, Transactions of the ASME*, pages 330–334, Oct 1972.

[17] A. Eshel. The propagation of disturbances in the infinitely wide foil bearing. *Journal of Lubrication Technology, Transactions of the ASME*, 91:120, 1969.

[18] A. Eshel and Jr. H.G. Elrod. The theory of the infinitely wide, perfectly flexible, self acting foil bearing. *Journal of Basic Engineering, Transactions of the ASME*, 87:831–836, Dec 1965.

[19] A. Eshel and M. Wildmann. Dynamic behavior of a foil bearing in the presence of a lubricating film. *Journal of Applied Mechanics, Transactions of the ASME*, 35:242, 1968.

[20] W. Flugge. *Stresses in Shells*. Springer-Verlag, Berlin, 1960.

[21] K. Fujimoto, E. Nagaoka, S. Watanabe, and K. Kawakami. Tape deforamation analysis considering in-plane stress. *Proceedings of the 1993 JSME International Conference on Advanced Mechatronics, Tokyo, Japan, Aug. 1993*, pages 905–910, 1993.

[22] Y. C. Fung and W. H. Wittrick. A boundary layer phenomenon in the large deflexion of thin plates. *Quart. Journ. Mech. and Appliead Math.*, 8:191–210, 1955.

[23] R.F. Gans. Lubrication theory at arbitrary knudsen number. *Journal of Lubrication Technology, Transactions of the ASME*, 107:431, July 1985.

[24] G.D. Granzow and A.O. Lebeck. An improved one-dimensional foil bearing solution. *ASLE, SP-16*, pages 54–58, 1984.

[25] H.J. Greenberg. Study of head-tape interaction in high speed rotating head recording. *IBM Journal of Research and Development*, 23:197, 1979.

[26] J.A. Greenwood and J.B.P. Williamson. Conatct of nominally flat surfaces. *Proc. Roy. Soc. London*, A295:300–319, 1966.

[27] W.A. Gross, editor. *Fluid Film Lubrication*. John Wiley & Sons, New York, 1980.

[28] Bernard J. Hamrock. *Fundamentals of Fluid Film Lubrication*. McGraw-Hill, New York, 1994.

[29] J.C. Heinrich and D. Connelly. Three-dimensional finite element analysis of self-acting foil bearings. *Computer Methods in Applied Mechanics and Engineering*, 100:31–43, 1992.

[30] J.C. Heinrich and S.K. Wadhawa. Analysis of self-acting foil bearings: A finite element approach. *ASLE, SP-21*, page 152, 1986.

[31] H.M. Hilber. *Analysis and design of Numerical integration methods in structural dynamics*. PhD thesis, University of California, Berkeley, 1976.

[32] Y. Hori, A. Hasiuke, T. Higashi, and Y. Nagase. A study on foil bearings -an application to tape memory devices. *Joint JSME-ASME Applied Mechanics Western Conference*, pages 121–128, 1975.

[33] Y.T. Hsia and G.A. Domoto. An experimental investigation of molecular rarefaction effects in gas lubricated bearings at ultra-low clearances. *Journal of Lubrication Technology*, 105:120–130, 1983.

[34] T.J.R. Hughes. *The Finite Element Method; Linear Static and Dynamic Finite Element Analysis*. Prentice-Hall, New Jersey, 1987.

[35] Earle H. Kennard. *Kinetic Theory of Gases*. McGraw-Hill Book Company, New York, 1938.

[36] H. Kotera, H. Kita, Y. Mizoh, and H. Yohda. Finite element analysis of visco-elastic frictional phenomena in vtr. *Private communication*, 1993.

[37] C. A. Lacey and F.E. Talke. Tape dynamics in a high-speed helical recorder. *IEEE Transactions on Magnetics*, 26(5):2208–2210, Sept 1990.

[38] C. A. Lacey and F.E. Talke. A tightly coupled numerical foil bearing solution. *IEEE Transactions on Magnetics*, 1990. Proceedings of 1st TMRC Conference.

[39] C.A. Lacey. *The Head/Tape Interface.* PhD thesis, University of California, San Diego, 1992.

[40] A.W. Leissa. *Vibration of Shells.* NASA-SP 288, 1973.

[41] L. Licht. An experimental study of elastohydrodynamic lubrication of foil bearings. *Journal of Lubrication Technology, Transactions of the ASME*, 90(1):199–220, Jan 1968.

[42] J.T.S. Ma. An investigation of self acting foil bearings. *Journal of Basic Engineering, Transactions of the ASME*, pages 837–846, 1965.

[43] C.D. Mee and E.D. Daniel, editors. *Magnetic Recording Volume I: Technology.* McGraw-Hill, 1987.

[44] C.D. Mee and E.D. Daniel, editors. *Magnetic Recording Volume II: Computer Data Storage.* McGraw-Hill, 1988.

[45] Y. Mitsuya. Modified reynolds equation for ultra-thin film gas lubrication using 1.5-order slip flow model and considering surface accommodation coefficient. *Journal of Tribology*, 115:289–294, 1993.

[46] D.K. Miu. *Dynamics of Gas-Lubricated Slider Bearings in Magnetic Recording Disk Files; Theory and Experiment.* PhD thesis, University of California, Berkeley, 1985.

[47] Y. Mizoh, H. Yohda, H. Kita, and H. Kotera. Simulation of head wear and reproduction envelope by the finite element method. *Electronics and Communications in Japan, Part 2*, 75(11):91–100, 1992.

[48] M. Mizukawa, H. Hosaka, and S. Hara. Study on spherical foil bearing, 4th report, comparison between experiment and analysis for large bearing penetration. *Bulletin of the Japan Society of Mechanical Engineers*, 28(243), Sept 1985.

[49] Sinan Muftu and Richard C. Benson. Numerical simulation of tape dynamics in helical-scan recording. *IEEE Transactions on Magnetics*, 1993.

[50] Sinan Muftu and Richard C. Benson. A numerical solution for the transient displacement of a circumferentially moving cylindrical shell. *Journal of Vibration and Acoustics, Transactions of the ASME*, 1993.

[51] Y. Nishida and H. Hosaka. Dynamic deflection of magnetic tape due to rotating head scanning. *Bulletin of the Japan Society of Mechanical Engineers*, 1984.

[52] K. Ono and T. Ebihara. Improved green's function in tape deflection and solutions of head contour with uniform contact pressure. *ASLE, SP-16*, pages 97–102, 1984.

[53] K. Ono, N. Kodama, and S. Michimura. A new numerical analysis method for two-dimensional foil-bearing problems based on inverse analysis concept. *JSME International Journal*, 34(1), 1991.

[54] K. Ono and M. Mizukawa. Study on spherical foil bearing (2nd report, analysis including foil bending stiffness and its experimental verification). *Bulletin of the Japan Society of Mechanical Engineers*, 24(198), Dec 1981.

[55] D.M. Perry, J.K. Knudsen, and W.L. Skelcher. Design of flying heads for tensioned flexible recording media. *IEEE Transactions on Magnetics*, MAG-22, Sept 1986.

[56] William H. Press, Brian P. Flannery, Saul A. Teukolsky, and William T. Vetterling. *Numerical Recipes, The Art of Scientific Computing (FORTRAN version)*. Cambridge University Press, 1990.

[57] P.M.J. Rongen. On numerical solutions of the instationary 2d foil bearing problem. *ASLE SP-29*, pages 130–138, 1990.

[58] K.J. Stahl, J.W. White, and K.L. Deckert. Dynamic response of self acting foil bearings. *IBM Journal of Research and Development*, pages 513–520, 1974.

[59] R. Sundaram and R.C. Benson. A green's function with improved convergence for cylindrically wrapped tapes. *STLE SP-26*, 1989.

[60] R. Sundaram and R.C. Benson. Tape dynamics following an impact. *IEEE Transactions on Magnetics*, 26(5):2211–2213, sept 1990.

[61] Rudolph Szilard. *Theory and Analysis of Plates, Classical and Numerical Methods.* Prentice-Hall, 1974.

[62] K. Tanaka. Analytical and experimental study of tape spacing for magnetic tape unit- effects of tape bending rigidity, gas compressibility, and molecular mean free path. *ASLE, SP-19*, pages 72–79, 1985.

[63] S.P. Timoshenko and J.M. Gere. *Theory of Elastic Stability.* McGraw-Hill, 1961.

[64] S.P. Timoshenko and S. Woinkowsky-Krieger. *Theory of Plates and Shells.* McGraw-Hill, 1987.

[65] A.C. Ugural. *Stresses in Plates and Shells.* McGraw-Hill, New York, 1981.

[66] Robert Vichnevetsky and John B. Bowles. *Fourier Analysis of Numerical Approximations of Hyperbolic Equations.* SIAM, 1982.

[67] S.M. Vogel and J.L. Groom. White light interferometry of elastohydrodynamic lubrication of foil bearings. *IBM Journal of Research and Development*, pages 521–528, Nov 1974.

[68] J.W. White and A. Nigam. A factored implicit scheme for the numerical solution of the reynolds equation at very low spacing. *Journal of Lubrication Technology, Transactions of the ASME*, 102:80–85, Jan 1980.

[69] J.W. White and P.P.Prabhu. An inverse procedure for optimum foil bearing design. *ASLE, SP-19*, pages 36–42, Oct 1985.

[70] J.A. Wickert and Jr. C.D. Mote. Classical vibration analysis of axially moving continua. *Journal of Applied Mechanics, Transactions of the ASME*, 57:738–744, 1990.

[71] M. Wildmann. Foil bearings. *Journal of Lubrication Technology, Transactions of the ASME*, pages 37–44, Jan 1969.

[72] B. Wolf, N. Deshpande, and V. Castelli. The flight of finite width foil bearings. *Journal of Lubrication Technology, Transactions of the ASME*, 105:138–142, 1983.

[73] K. Yoneda and T. Sawada. Simulation of tape flying characteristics above vtr drum considering in-plane stresses. *IEEE Transactions on Magnetics*, 24(6):2766–2768, sept 1988.